Controlled Generation and Characterization of Multi-component Fluid/Fluid Interfaces

Submitted in partial fulfillment of the requirements for

the degree of

Doctor of Philosophy

in

Chemical Engineering

Stephanie M. Kirby

B.S., Chemical and Biomolecular Engineering, University of Pennsylvania

Carnegie Mellon University
Pittsburgh, PA

April, 2017

ACKNOWLEDGEMENTS

Firstly, I'd like to thank my advisors, Professors Lynn Walker and Shelley Anna, for all of their support and encouragement throughout my graduate career. They always pushed me to reach my full potential, and perhaps just as importantly, taught me to see the value in my own work. Through their guidance I have become a better researcher, and I feel immensely fortunate to have had the opportunity to work with them. I'd also like to thank my committee members, Professors Bob Tilton, Mike Domach, and Steve Garoff.

I owe thanks to all the past and current members of the Complex Fluids group for making the 3rd floor such an amazing place to work. In particular, thanks to Matt Reichert, who brought me up to speed in the lab and whose advice since has been invaluable. Thanks to Chris Nelson for always lending me his tinkering skills in the lab, and to Melissa Dao and Javier Lanauze for keeping me well-caffeinated with plenty of afternoon coffee breaks. Thanks to the entire Walker and Anna groups: I can't count the number of times our conversations have helped me solve a research problem or just made a rough day in the lab better. I never thought I could have so much fun working.

I'm also so grateful for the friends I've made outside the lab who have made my years here fly by. To my extended fifth-year family, thank you for making me laugh and reminding me to take breaks every once in a while. Thursday nights won't be the same without you. To my non-grad school friends, thank you for enduring more conversations about research than you ever signed up for. A special

heartfelt thank you to Chris Knapp: your encouragement and support has meant the world to me. Finally, thanks to my family, especially my parents, for cheering me on throughout this entire process. To all my friends and mentors past and present, this work would not have been possible without you. Thank you!

Funding for this work was provided by the Gulf of Mexico Research Initiative (GoMRI) and the National Science Foundation (CBET-1437864).

ABSTRACT

The stabilization of multiphase fluid formulations via addition of multiple surface active materials is widespread across various industries and applications. The properties of the air/water and oil/water interfaces that are affected by these materials, including surface tension and elasticity, have been shown to correspond to measurable changes in desirable bulk properties, such as foam and emulsion stability. However, equilibrium interfacial tension values are rarely enough to predict or design stability. Understanding the dynamic interfacial behavior of these materials is critical for improving formulation design.

This work aims to characterize the interfacial properties of multi-component systems at air/water and oil/water interfaces. A microtensiometer platform is used to measure interfacial tension and interfacial mechanics to quantify multi-species adsorption under a variety of conditions, including adsorption time, concentration, and ionic strength. This technique is used to characterize several model systems, encompassing nonionic and anionic surfactants, rhamnolipid biosurfactants, hydrophobin proteins and surfactant-particle complexes. Dynamic interfacial tension measurements of surfactant systems reveal the irreversible adsorption behavior of a polymeric surfactant and rhamnolipids, as well as the effects of added small molecule surfactants on their persistence at the interface.

For larger adsorbed species, measuring the interfacial mechanics is important to capture adsorption behavior more completely. Through precise control of bulk solution properties, rigid incompressible protein and nanoparticle films are created that can effectively stabilize interfaces. The unique interfacial mechanics

of the films are only observed when the interfaces are generated utilizing a controlled adsorption procedure.

The results on these model systems highlight the complex nature of the interactions of multiple species on an interface. Systematic modification of the bulk solution allows for the generation of mixed interfaces where interfacial properties that are traditionally confounded by bulk species interaction or dispersion instability can be probed. These interfacial measurements contribute to the overall understanding of the importance of processing as well as composition on desirable formulation properties.

TABLE OF CONTENTS

LIST OF TABLES

LIST OF FIGURES

CHAPTER 1

INTRODUCTION

Foams and emulsions are present across a wide variety of industrial and biological applications, including use in food and consumer products, pharmaceuticals, enhanced oil recovery, and environmental remediation. One of the most important criteria in foam and emulsion formulation design is ensuring stability to prevent phase separation. Stability is achieved through the addition of various surface active species that adsorb at fluid/fluid interfaces, reducing the free energy of the system. Often, multiple components are present on the interface, via the intentional addition of multiple stabilizers to a formulation or due to the presence of other surface active components naturally present in the system. These compounds modify the properties of the interfaces to which they adsorb, affecting overall system properties. Understanding the adsorption behavior of multiple surface active species is necessary for improving formulation design and application.

Multi-component systems at air/water and oil/water interfaces have been characterized using a variety of techniques. Interfacial structure can be determined through atomic force microscopy,[1] Brewster angle microscopy,[2] ellipsometry,[3] and neutron reflectivity.[4] Interfacial rheology measurements have been used to characterize interfacial mechanics,[5] while interfacial tension measurements provide dynamic and equilibrium information to lend insight into transport and adsorption phenomena for a variety of systems.[6,7] A common approach to characterizing multi-component systems with interfacial tension is to allow multiple species in the bulk

solution to simultaneously adsorb at an oil/water or air/water interface. Relative and absolute concentrations of each species can be manipulated to estimate the amount of each component on the interface.[8] This approach has the advantage of more closely representing a real application environment, but limits understanding of, and control over, the exact composition on the interface. Further, mixtures of various surface-active species often exhibit strong bulk interactions that impact their surface activity. These bulk interactions result in significant deviations from ideal mixing laws and complicated adsorption behavior.[9,10]

An alternate approach employed in this study is sequential adsorption, where only one species is exposed to the interface at a time. This approach is particularly useful when one or more components irreversibly adsorb to the interface, persisting even when the bulk concentration is changed. By employing a sequential adsorption technique, we mitigate the potential for any bulk species interaction and can directly control the exposure of the interface to each individual species. Measurements of both the dynamic interfacial tension and interfacial mechanics are used to characterize non-equilibrium systems as a function of adsorption time, concentration, and ionic strength. In addition, by controlling the reservoir solution conditions, we assess the effect of changing environments on interfacial properties that are relevant to industrial processing conditions and the lifetime of these interfaces.

Experiments are performed on a microtensiometer platform to measure the interfacial tension and interfacial mechanics of several systems. The microtensiometer is based on a capillary pressure tensiometer, where an oil drop or

air bubble forms a spherical cap at the tip of a capillary in line with a pressure transducer. The Laplace equation is used to calculate surface tension from the measured pressure jump across a curved interface and the radius of the interface. The solution reservoir of the microtensiometer is ~ 3 mL, which allows for rapid solution exchange and control over reservoir conditions. A detailed description of the device and experimental techniques is provided in Chapter 3.

In Chapter 4, the adsorption of a nonionic surfactant Tween 80 and an anionic surfactant Aerosol-OT (AOT) is measured at a squalane/water interface. Tween 80 and AOT are two of the main components in commercial dispersants used in response to oil spills. Tween 80 has been shown to adsorb irreversibly at oil/water interfaces,[11] which is relevant not only to dispersant efficacy but also to the environmental impact of dispersant use in oil spill remediation. Chapter 4 characterizes the effect of an added surfactant on the irreversibly adsorbed component of Tween 80. To achieve this, a layer of Tween 80 is generated at a squalane/water interface and the surfactant solution in the reservoir is replaced with deionized water. AOT is then introduced to the reservoir and the adsorption of the secondary surfactant on the pre-formed Tween 80 layer is measured. The effect of subphase ionic strength on AOT adsorption is also investigated. AOT is shown to co-adsorb at interfaces pre-coated with Tween 80, but the presence of Tween 80 inhibits AOT adsorption, reducing the maximum surface concentration. Even after exposure to high AOT concentrations, Tween 80 remains irreversibly adsorbed at the interface. The results provide insight to a commercially relevant surfactant

system and highlight the different roles surfactants play in stabilizing oil/water interfaces.

Using similar techniques, Chapter 5 investigates the adsorption behavior of rhamnolipid biosurfactants at air/water and oil/water interfaces. Rhamnolipids are produced by an oil metabolizing bacteria and play a critical role in the biodegradation of dispersed oil droplets from an oil spill.[12] Their adsorption at bare interfaces as well as interfaces coated with the irreversibly adsorbed surfactant Tween 80 is characterized using dynamic interfacial tension measurements. Rhamnolipid adsorption is partially irreversible at both air/water and oil/water interfaces, but the presence of a Tween 80 at the interface reduces the ability of rhamnolipid to remain irreversibly adsorbed upon rinsing. A scaling analysis developed by Alvarez *et al.*[13] is used to characterize dilute rhamnolipid adsorption to air/water and oil/water interfaces as diffusion-limited, and lower bounds on the kinetic adsorption parameters are presented. The microtensiometer is a particularly useful instrument for characterizing the dynamics of adsorption of rhamnolipids, as it requires only a small solution volume and results in a rapid adsorption rate due to the high radius of curvature of the interface.

In Chapter 6, the adsorption of the hydrophobin Cerato-ulmin (CU) at an air/water interface is presented. Hydrophobins are globular proteins that have been shown to form strong membranes at interfaces,[14,15] but measuring the interfacial properties of the films is challenging once the interface is no longer fluid.[16] Through a combination of surface tension and dilatational modulus measurements, we observe the dynamic formation of an irreversibly adsorbed, fully rigid protein film

at the interface. Measurements are performed up through solidification, providing a minimum estimate of the modulus of the rigid films. Similar results are obtained for CU adsorption at a squalane/water interface, presented in the Appendix.

Using the sequential adsorption procedures from Chapters 4 and 5, we introduce the surfactant sodium dodecyl sulfate (SDS) to a fully rigid CU film. SDS co-adsorbs to the protein film, and both the surface tension and dilatational modulus of the resulting mixed interface are shown to be functions of bulk SDS concentration. At high SDS concentrations (just below the CMC), we are able to form mixed SDS-CU layers on the surface that are fully incompressible. Mixed films with these mechanics are not obtainable through simple co-adsorption from bulk solution. At larger SDS concentrations, the SDS displaces the adsorbed CU, and upon rinsing results in a clean air/water surface.

In Chapter 7, the adsorption of surfactant-nanoparticle complexes at an air/water interface is characterized. Negatively charged silica nanoparticles alone are not surface active, but the addition of cationic surfactant results in a surfactant-nanoparticle complex that readily adsorbs to air/water interfaces.[17–19] The effect of modifying surfactant tail length as well as modifying the ionic strength of the solution is investigated using surface tension and interfacial mechanical measurements. We observe that transport to the interface is dominated by the added surfactant, but the interfacial mechanics are governed by particle interactions on the surface. By tuning the subphase ionic strength and inducing compressive flow on the surface, we can generate incompressible particle-coated interfaces at relatively low particle fractions.

Overall, this work uses experimental techniques to control the adsorption of multiple species at interfaces and allows for precise measurement of individual contributions to the properties of mixed interfaces. Through the combination of controlled interfacial formation and simultaneous interfacial tension and interfacial rheology measurements, we create a more complete picture of the nature of complex, multi-component interfaces. Furthermore, we highlight the role that interfacial processing and environmental history has on the properties and composition of these interfaces. The findings presented here can be used to improve formulation and process design across a variety of surface active systems and applications.

REFERENCES

(1) Mackie, A.; Wilde, P. The Role of Interactions in Defining the Structure of Mixed Protein-Surfactant Interfaces. *Adv. Colloid Interface Sci.* **2005**, *117*, 3–13.

(2) Patino, J.; Sanchez, C.; Nino, R. Is Brewster Angle Microscopy a Useful Technique To Distinguish between Isotropic Domains in B-Casein - Monoolein Mixed Monolayers at the Air - Water Interface ? *Langmuir* **1999**, *15*, 4777–4788.

(3) Asnacios, A.; Langevin, D.; Argillier, J. Complexation of Cationic Surfactant and Anionic Polymer at the Air-Water Interface. *Macromolecules* **1996**, *9297*, 7412–7417.

(4) Goddard, E. D. Polymer/Surfactant Interaction: Interfacial Aspects. *J. Colloid Interface Sci.* **2002**, *256*, 228–235.

(5) Fainerman, V. B.; Miller, R.; Ferri, J. K.; Watzke, H.; Leser, M. E.; Michel, M. Reversibility and Irreversibility of Adsorption of Surfactants and Proteins at Liquid Interfaces. *Adv. Colloid Interface Sci.* **2006**, *123–126*, 163–171.

(6) Kotsmár, C.; Grigoriev, D. O.; Makievski, a. V.; Ferri, J. K.; Krägel, J.; Miller, R.; Möhwald, H. Drop Profile Analysis Tensiometry with Drop Bulk Exchange to Study the Sequential and Simultaneous Adsorption of a Mixed β-Casein /C12DMPO System. *Colloid Polym. Sci.* **2008**, *286*, 1071–1077.

(7) Miller, R.; Fainerman, V. B.; Makievski, a V; Krägel, J.; Grigoriev, D. O.; Kazakov, V. N.; Sinyachenko, O. V. Dynamics of Protein and Mixed Protein/surfactant Adsorption Layers at the Water/fluid Interface. *Adv. Colloid Interface Sci.* **2000**, *86*, 39–82.

(8) Rosen, M.; Hua, X. Surface Concentrations and Molecular Interactions in Binary Mixtures of Surfactants. *J. Colloid Interface Sci.* **1982**, *86*, 164–172.

(9) Hines, J.; Thomas, R. Investigation of Mixing in Binary Surfactant Solutions by Surface Tension and Neutron Reflection: Anionic/nonionic and Zwitterionic/nonionic Mixtures. *J. Phys. Chem. B* **1997**, *101*, 9215–9223.

(10) Okano, T.; Tamura, T.; Abe, Y.; Tsuchida, T. Micellization and Adsorbed Film Formation of a Binary Mixed System of Anionic/nonionic Surfactants. *Langmuir* **2000**, *16*, 1508–1514.

(11) Reichert, M. D.; Walker, L. M. Interfacial Tension Dynamics, Interfacial Mechanics, and Response to Rapid Dilution of Bulk Surfactant of a Model Oil-Water-Dispersant System. *Langmuir* **2013**, *29*, 1857–1867.

(12) Churchill, S. A.; Griffin, R. A.; Jones, L. .; Chirchill, P. . Biodegradation Rate Enhancement of Hydrocarbons by an Oleophilic Fertilizer and a Rhamnolipid Biosurfactant. *J. Environ. Qual.* **1995**, *24*, 19–28.

(13) Alvarez, N.; Walker, L.; Anna, S. Diffusion-Limited Adsorption to a Spherical Geometry: The Impact of Curvature and Competitive Time Scales. *Phys. Rev. E* **2010**, *82*, 11604.

(14) Linder, M. B. Hydrophobins: Proteins That Self Assemble at Interfaces. *Curr. Opin. Colloid Interface Sci.* **2009**, *14*, 356–363.

(15) Wösten, H. A. B. Hydrophobins: Multipurpose Proteins. *Annu. Rev. Microbiol.* **2001**, *55*, 625–646.

(16) Cox, A. R.; Cagnol, F.; Russell, A. B.; Izzard, M. J. Surface Properties of Class II Hydrophobins from Trichoderma Reesei and Influence on Bubble Stability. *Langmuir* **2007**, *23*, 7995–8002.

(17) Ravera, F.; Santini, E.; Loglio, G.; Ferrari, M.; Liggieri, L. Effect of Nanoparticles on the Interfacial Properties of Liquid/liquid and Liquid/air Surface Layers. *J. Phys. Chem. B* **2006**, *110*, 19543–19551.

(18) Binks, B. P.; Rodrigues, J. a; Frith, W. J. Synergistic Interaction in Emulsions Stabilized by a Mixture of Silica Nanoparticles and Cationic Surfactant. *Langmuir* **2007**, *23*, 3626–3636.

(19) Maestro, A.; Guzmán, E.; Santini, E.; Ravera, F.; Liggieri, L.; Ortega, F.; Rubio, R. G. Wettability of Silica Nanoparticle-Surfactant Nanocomposite Interfacial Layers. *Soft Matter* **2012**, *8*, 837–843.

CHAPTER 2

BACKGROUND

2.1 SURFACE-ACTIVE SPECIES

2.1.1 Molecular Surfactants

Surfactants are a widely used class of materials that perform a variety of functions, including acting as lubricants, dispersants, wetting agents, and foam and emulsion stabilizers.[1,2] Surfactant molecules are amphiphilic, typically comprised of a hydrophilic head group attached to a hydrophobic tail. They adsorb to surfaces (air/liquid boundaries) and interfaces (immiscible liquid/liquid boundaries) and lower the free energy of the interface by reducing the interfacial tension between the two phases. As such, interfacial tension measurements are useful in characterizing surfactant adsorption.

Depending on the structure of the head group, aqueous surfactants are broadly classified as nonionic, anionic, cationic, or zwitterionic (with both positive and negative charges present in the head group). The adsorption of ionic surfactants at interfaces is affected by both the charge of the surface and the ionic strength of the solution; increasing ionic strength reduces the electrostatic repulsion between surfactant molecules and increases overall adsorption. Maintaining electric neutrality in the surface layer requires that counterion adsorption equal surfactant adsorption at the surface.[3]

The adsorption of small-molecule surfactants is typically reversible, where the surfactants can freely desorb from the surface. Larger polymeric surfactants

have shown some irreversibility at air/water and oil/water interfaces, due to conformational changes at the interface that increase their binding energy.[4–6]

2.1.2 Proteins

Proteins are large, complex amphiphilic molecules often comprised of ionic, polar, and non-polar regions. Like surfactants, the amphiphilic nature of many proteins makes them surface active. The adsorption of proteins at air/water and oil/water interfaces is of interest in a variety of applications, including in food products and pharmaceuticals.[7,8] Once adsorbed, proteins can undergo reorientation or denaturation at the interface, often forming inter-molecular linkages that alter the mechanics of the interface.[9] The ability of proteins to increase foam and emulsion stability is linked to their interfacial rheological properties, which often depend strongly on surface age and protein type.[10]

One particular class of proteins known as hydrophobins exhibits unusual surface properties. Hydrophobins are produced by filamentous fungi and share a similar rigid, globular structure that enables strong surface adsorption.[11–13] Unlike many other proteins, hydrophobins do not denature in solution or at the interface,[14] yet they are able to form strong membranes that stabilize non-equilibrium bubble shapes and wrinkle upon compression.[15,16]

2.1.3 Particles

Pickering foams and emulsions are systems stabilized by the adsorption of

particles at the air/water or oil/water interface. Particle adsorption lends steric stability to interfaces not provided by small molecule surfactants, reducing the rate of bubble coalescence and coarsening.[17–19] Particles lower the interfacial energy by pinning at the interface and reducing the total interfacial area. The energy required to adsorb a particle at an interface is estimated by

$$E = \pi R^2 \gamma (1 \pm \cos\theta)^2, \tag{2.1}$$

where R is the radius of the particle, γ is the interfacial tension, and θ is the particle contact angle at the interface.[20] Values of adsorption energy for 10 nm nanoparticles can range from $10^2 - 10^3 kT$, resulting in particles that are irreversibly pinned to the interface.

The adsorption of colloidal particles ($R > 1$ μm) at air/water interfaces has been studied extensively using a combination of microscopy and surface tension measurements (typically using spread particle monolayers on a Langmuir trough).[17] The interparticle interactions that govern bulk particle dispersion properties also impact interfacial behavior. Electrostatic repulsion between negatively charged particles at the air/water interface results in the formation of an ordered particle array; particle spacing can be tuned by modifying the ionic strength of the particle subphase.[21] Compressing a particle monolayer on a Langmuir trough results in highly ordered hexagonal particle packing, until a failure of the monolayer occurs and the interface buckles or expels particles from the surface.[22]

While colloidal particle adsorption can be observed optically, measuring the adsorption of nanoparticles at air/water interfaces requires the use of indirect methods, since nanoparticles are below the resolution limits of most optical

techniques. A combination of surface tension and rheological measurements can be used to characterize nanoparticle adsorption.

2.2 DYNAMIC SURFACE TENSION

Surface (or interfacial) tension is a measure of the interfacial free energy per unit area. Several measurement techniques exist that use either geometric methods (pendant drop, sessile drop, capillary height) or direct force measurements (Du Nüoy ring, Wilhelmy plate) to determine surface tension. The measurement technique used throughout this work uses the capillary pressure of a curved interface to calculate the surface tension. For a spherical interface, the Laplace equation defines the surface tension γ as,

$$\gamma = \frac{(P_1 - P_2)R}{2}, \tag{2.2}$$

where P_1 is the pressure inside the drop or bubble, P_2 is the pressure outside the drop or bubble, and R is the radius of the interface. Surface tension is related to surface coverage, Γ, by the Gibbs adsorption equation,

$$\Gamma = -\frac{1}{nRT}\frac{\partial\gamma}{\partial \ln C}, \tag{2.3}$$

where C is the bulk surfactant concentration, R is the gas constant, T is the temperature, and the integer n accounts for potential counterion adsorption. For a nonionic surfactant, n = 1; for an ionic surfactant, n = 2.[23] An isotherm model is chosen to define the relationship between Γ and bulk concentration. The Langmuir isotherm is widely used for simple surfactant systems, which assumes surfactants

adsorb in a monolayer and do not interact on the surface. The Langmuir model defines surface coverage as,

$$\Gamma = \frac{\Gamma_\infty C}{C + a} \tag{2.4}$$

where Γ_∞ is the maximum surface concentration and a is the ratio of the desorption rate constant, α, to the adsorption rate constant, β, such that $a = \alpha / \beta$. Substituting the Langmuir isotherm into equation (2.3) gives a relationship between surface tension and surface coverage, or equation of state,

$$\gamma = \gamma_0 + RT\Gamma_\infty \ln\left(1 - \frac{\Gamma}{\Gamma_\infty}\right), \tag{2.5}$$

where γ_0 is the surface tension of the clean interface. Another commonly used isotherm is the Volmer model, which also assumes monolayer adsorption and no interaction on the surface, but allows for finite size of the adsorbed molecules and mobility of species on the interface. The Volmer isotherm has been used to model the adsorption of particles and globular proteins.[24–27] The Volmer isotherm defines surface coverage as,

$$\Gamma = C\left(1 - \frac{\Gamma}{\Gamma_\infty}\right)\exp\left(\frac{\Gamma}{\Gamma_\infty - \Gamma}\right). \tag{2.6}$$

Substituting equation (2.6) into equation (2.3) gives the resulting Volmer equation of state,

$$\gamma = \gamma_0 - \frac{RT}{\left(\frac{1}{\Gamma} - \frac{1}{\Gamma_\infty}\right)}. \tag{2.7}$$

The isotherms discussed above both assume the system has reached equilibrium. However, the kinetics of adsorption are also relevant for a variety of applications that involve the generation of "fresh" interface that is initially devoid of any surface active material. Adsorption occurs in two distinct stages: diffusion from the bulk solution to the interface, and the transfer of species from the sub-surface to the interface. A characteristic timescale for diffusion to the interface is defined as $\tau_D = l^2 / D$, where l is the length scale across which diffusion must occur, and D is the diffusion coefficient. For a planar interface,

$$\tau_{D,p} = h_p^2 / D, \tag{2.8}$$

where h_p is the planar diffusion depth, $h_p = \Gamma_{eq} / C$. For a spherical interface, the characteristic diffusion timescale is defined as[28]

$$\tau_{D,s} = \frac{(h_s^3 h_p)^{1/2}}{D}, \tag{2.9}$$

where the spherical diffusion depth $h_s = R\left[\left(3\frac{h_p}{R}+1\right)^{1/3} - 1\right]$.

The kinetic rate of transfer to the interface from the sub-surface can be described by the Langmuir rate equation,

$$\frac{\partial \Gamma}{\partial t} = \beta C \Gamma_\infty \left(1 - \frac{\Gamma}{\Gamma_\infty}\right) - \alpha \Gamma. \tag{2.10}$$

From equation (2.10), a kinetic timescale is identified as

$$\tau_K = \frac{1}{\beta C + \alpha}. \tag{2.11}$$

Comparing τ_D and τ_K allows for an adsorption process to be described as diffusion-limited ($\tau_D >> \tau_K$), kinetically-limited ($\tau_K >> \tau_D$), or a mixture of both mechanisms.

2.3 INTERFACIAL RHEOLOGY

The adsorption of surface active materials to an interface often impacts the rheological properties of the interface. Rheological properties relate interfacial stresses to imposed strains that arise from interfacial deformation. The mode of deformation considered in this work is dilation, in which the surface area is expanded or compressed while a constant interfacial shape is maintained. The corresponding dilatational modulus relates the surface stress, P^S, to the imposed change in area A,

$$E = \frac{dP^S}{d\ln A} = \frac{d\gamma}{d\ln A} + \frac{1}{2}\frac{d(\tau_{\theta\theta} + \tau_{\phi\phi})}{d\ln A}. \tag{2.12}$$

The total surface stress includes contributions from both the surface tension and intrinsic dilatational stresses, τ, that depend on the rate of deformation.[29] The component of the dilatational modulus that is due solely to changes in the surface tension, $\frac{d\gamma}{d\ln A}$, is a thermodynamic quantity known as the Gibbs modulus. Equation (2.12) neglects any contributions from bending stresses that arise for a curved interface.

The dilatational modulus is typically measured by imposing a small amplitude oscillatory dilation at frequency ω. The resulting surface stress oscillates

at the same frequency, shifted by phase angle Φ. The relationship is then reported as

$$E^*(\omega) = E' + iE'' = \frac{dP^S}{d\ln A} e^{i\Phi}, \qquad (2.13)$$

where E^* is a complex quantity that consists of an in-phase component E' and out-of-phase component E''. The complex dilatational modulus has been linked to a variety of interfacial properties that impact overall complex system behavior, including the long term stability of foams and emulsions.[8,10,30,31]

REFERENCES

(1) Rosen, M. *Surfactants and Interfacial Phenomena*; 3rd Ed.; Wiley-Interscience: New York, 2004.

(2) Berg, J. C. *An Introduction to Interfaces and Colloids*; 1st Ed.; World Scientific: New Jersey, 2010.

(3) Eastoe, J.; Dalton, J. S. Dynamic Surface Tension and Adsorption Mechanisms of Surfactants at the Air-Water Interface. *Adv. Colloid Interface Sci.* **2000**, *85*, 103–144.

(4) Reichert, M. D.; Walker, L. M. Interfacial Tension Dynamics, Interfacial Mechanics, and Response to Rapid Dilution of Bulk Surfactant of a Model Oil-Water-Dispersant System. *Langmuir* **2013**, *29*, 1857–1867.

(5) Kirby, S. M.; Anna, S. L.; Walker, L. M. Sequential Adsorption of an Irreversibly Adsorbed Nonionic Surfactant and an Anionic Surfactant at an Oil/Aqueous Interface. *Langmuir* **2015**, *31*, 4063–4071.

(6) Huston, K. J.; Larson, R. G. Reversible and Irreversible Adsorption Energetics of Poly(ethylene Glycol) and Sorbitan Poly(ethoxylate) at a Water/Alkane Interface. *Langmuir* **2015**, *31*, 7503–7511.

(7) Dickinson, E. Proteins at Interfaces and in Emulsions: Stability, Rheology and Interactions. *J. Chem. Soc. Faraday Trans.* **1998**, *94*, 1657–1669.

(8) Damodaran, S. Protein Stabilization of Emulsions and Foams. *J. Food Sci.* **2005**, *70*, R54–R66.

(9) Freer, E. M.; Yim, K. S.; Fuller, G. G.; Radke, C. J. Interfacial Rheology of Globular and Flexible Proteins at the Hexadecane/Water Interface: Comparison of Shear and Dilatation Deformation. *J. Phys. Chem. B* **2004**, *108*, 3835–3844.

(10) Dickinson, E. Milk Protein Interfacial Layers and the Relationship to Emulsion Stability and Rheology. *Colloids Surf. B. Biointerfaces* **2001**, *20*, 197–210.

(11) Hektor, H. J.; Scholtmeijer, K. Hydrophobins: Proteins with Potential. *Curr. Opin. Biotechnol.* **2005**, *16*, 434–439.

(12) Wessels, J. Hydrophobins, Unique Fungal Proteins. *Mycologist* **2000**, *14*, 153–159.

(13) Linder, M. B. Hydrophobins: Proteins That Self Assemble at Interfaces. *Curr. Opin. Colloid Interface Sci.* **2009**, *14*, 356–363.

(14) Kisko, K.; Szilvay, G. R.; Vuorimaa, E.; Lemmetyinen, H.; Linder, M. B.; Torkkeli, M.; Serimaa, R. Self-Assembled Films of Hydrophobin Proteins HFBI and HFBII Studied in Situ at the Air/Water Interface. *Langmuir* **2009**, *25*, 1612–1619.

(15) Basheva, E. S.; Kralchevsky, P. a.; Christov, N. C.; Danov, K. D.; Stoyanov, S. D.; Blijdenstein, T. B. J.; Kim, H. J.; Pelan, E. G.; Lips, A. Unique Properties of Bubbles and Foam Films Stabilized by HFBII Hydrophobin. *Langmuir* **2011**, *27*, 2382–2392.

(16) Cox, A. R.; Cagnol, F.; Russell, A. B.; Izzard, M. J. Surface Properties of Class II Hydrophobins from Trichoderma Reesei and Influence on Bubble Stability. *Langmuir* **2007**, *23*, 7995–8002.

(17) Binks, B. P. Particles as Surfactants—Similarities and Differences. *Curr. Opin. Colloid Interface Sci.* **2002**, *7*, 21–41.

(18) Tambe, D. E.; Sharma, M. M. Factors Controlling the Stability of Colloid-Stabilized Emulsions. *JCIS*, 1993, *157*, 244–253.

(19) Stocco, A.; Drenckhan, W.; Rio, E.; Langevin, D.; Binks, B. P. Particle-Stabilised Foams: An Interfacial Study. *Soft Matter* **2009**, *5*, 2215–2222.

(20) Levine, S.; Bowen, B. D.; Partridge, S. J. Stabilization of Emulsions by Fine Particles I. Partitioning of Particles between Continuous Phase and Oil/water Interface. *Colloids and Surfaces* **1989**, *38*, 325–343.

(21) Aveyard, R.; Clint, J. H.; Nees, D.; Paunov, V. N. Compression and Structure of Monolayers of Charged Latex Particles at Air/water and Octane/water Interfaces. *Langmuir* **2000**, *16*, 1969–1979.

(22) Razavi, S.; Cao, K. D.; Lin, B.; Lee, K. Y. C.; Tu, R. S.; Kretzschmar, I. Collapse of Particle-Laden Interfaces under Compression: Buckling vs Particle Expulsion. *Langmuir* **2015**, *31*, 7764–7775.

(23) Eastoe, J.; Nave, S.; Downer, A.; Paul, A. Adsorption of Ionic Surfactants at the Air-Solution Interface. *Langmuir* **2000**, *16*, 4511–4518.

(24) Gurkov, T. D.; Russev, S. C.; Danov, K. D.; Ivanov, I. B.; Campbell, B. Monolayers of Globular Proteins on the Air/water Interface: Applicability of the Volmer Equation of State. *Langmuir* **2003**, *19*, 7362–7369.

(25) Fainerman, V.; Kovalchuk, V. Surface-Pressure Isotherms of Monolayers Formed by Microsize and Nanosize Particles. *Langmuir* **2006**, *22*, 1701–1705.

(26) Pauchard, V.; Rane, J. P.; Zarkar, S.; Couzis, A.; Banerjee, S. Long-Term Adsorption Kinetics of Asphaltenes at the Oil-Water Interface: A Random

Sequential Adsorption Perspective. *Langmuir* **2014**, *30*, 8381–8390.

(27) Kirby, S. M.; Zhang, X.; Russo, P. S.; Anna, S. L.; Walker, L. M. Formation of a Rigid Hydrophobin Film and Disruption by an Anionic Surfactant at an Air/Water Interface. *Langmuir* **2016**, *32*, 5542–5551.

(28) Alvarez, N.; Walker, L.; Anna, S. Diffusion-Limited Adsorption to a Spherical Geometry: The Impact of Curvature and Competitive Time Scales. *Phys. Rev. E* **2010**, *82*, 11604.

(29) Kotula, A. P.; Anna, S. L. Regular Perturbation Analysis of Small Amplitude Oscillatory Dilatation of an Interface in a Capillary Pressure Tensiometer. *J. Rheol. (N. Y. N. Y).* **2015**, *59*, 85–117.

(30) Dicharry, C.; Arla, D.; Sinquin, A.; Graciaa, A.; Bouriat, P. Stability of Water/crude Oil Emulsions Based on Interfacial Dilatational Rheology. *J. Colloid Interface Sci.* **2006**, *297*, 785–791.

(31) Georgieva, D.; Schmitt, V.; Leal-Calderon, F.; Langevin, D. On the Possible Role of Surface Elasticity in Emulsion Stability. *Langmuir* **2009**, *25*, 5565–5573.

CHAPTER 3

MATERIALS AND METHODS

3.1 SAMPLE PREPARATION

The surfactants used in this work are polysorbate 80 (Tween 80), dioctyl sodium sulfosuccinate (Aerosol-OT or AOT), sodium dodecyl sulfate (SDS), tetradecyltrimethylammonium bromide (C_{14}TAB), hexadecyltrimethylammonium bromide (C_{16}TAB), and octadecyltrimethylammonium bromide (C_{18}TAB). All synthetic surfactants are purchased from Sigma (St. Louis, MO). The biosurfactants used are a mixture of mono- and di-rhamnolipids, purchased from Sigma-Aldrich (St. Louis, MO) at 95% purity and used as received. Tween 80, AOT, and SDS are also used as received without further purification. The C_nTAB surfactants are purchased at 99% purity and are recrystallized twice in ethanol to remove impurities. Recrystallization is performed by dissolving the surfactant in ethanol at room temperature. The ethanol solution is stored in a -20 ^oC freezer overnight to crystallize the dissolved C_nTAB. The solution is filtered through a medium porosity fritted glass filter and the crystallized surfactant is retained, with a yield of about 30%.

Surfactant solutions are made with deionized water prepared by a Barnstead Ultrapure water purification system to 18.2 MΩ·cm resistivity. Stock solutions are made at concentrations above the critical micelle concentration (CMC) of each surfactant, and are prepared in 250-500 mL volumetric flasks that are acid-washed prior to solution preparation. Solutions of C_{16}TAB, C_{18}TAB, and rhamnolipid are stored above their Krafft temperatures in a 35 ^oC oven to ensure full solubility.[1,2]

Individual samples are prepared by volumetric dilution of the stock solutions into either 50 mL VWR (Batavia, IL) centrifuge tubes (Chapter 4) or 20 mL acid-washed scintillation vials (Chapters 5-7). All containers are pre-rinsed with the surfactant solutions to minimize depletion effects to the walls of the sample cell.[3]

The hydrophobin protein used in Chapter 6 and the Appendix is Cerato-ulmin (CU). Cerato-ulmin is a gift of Wayne Richards of the Canadian Forest Service, provided to us by Paul Russo of the Georgia Institute of Technology as a 0.02 mg/mL solution in deionized water. Dilution to 0.002 mg/mL for interfacial studies is made volumetrically, and samples are placed in a sonication bath immediately prior to use to eliminate any microscopic bubbles stabilized by CU.[4]

The particles used in Chapter 7 are Ludox TMA SiO_2 nanoparticles (Sigma, St. Louis, MO), purchased as a 34 wt% dispersion. Solutions containing mixed C_nTAB/SiO_2 complexes are prepared via dropwise addition of 0.2 mM C_nTAB solution into a 20 wt% SiO_2 dispersion in a method modified from Ravera *et al*.[5] The dispersion is held in a sonication bath and gently mixed during C_nTAB addition to aid in even surfactant distribution and avoid bulk aggregation. The C_nTAB/SiO_2 dispersions are kept in the sonication bath for 30 minutes after mixing to reduce flocculation. Dispersions are aged for 24 hours before use to ensure uniform surfactant distribution, and measurements are taken within 48 hours of sample preparation.

Squalane ($C_{30}H_{62}$) is used as the oil phase in Chapters 4 and 5 and the Appendix. Squalane is purchased from Sigma (St. Louis, MO) at 98% purity and is further purified via gravity filtration through a glass column packed with 2 g of

basic activated alumina (Sigma, St Louis, MO). The filter medium is held in place with a slug of 400 μm acid-washed silica beads purchased from OPS Diagnostics, LLC (Lebanon, NJ). To assess the purity after filtration, the interfacial tension is measured. The oil is considered sufficiently clean if the squalane/deionized water interfacial tension remains within 1 mN/m of the clean interfacial tension value (52.5 ± 0.5 mN/m) for at least 2000 seconds.

Sodium chloride is used to increase the ionic strength of solutions in Chapters 4 and 7. It is purchased from VWR (Batavia, IL) at 99% purity and is baked at 400^{o}C for 5 hours to remove hydrates and impurities. A stock solution is prepared with deionized water immediately after baking.

3.2 THE MICROTENSIOMETER

The microtensiometer platform developed by Alvarez *et al*.[6] is used throughout this work to measure the surface/interfacial tension and interfacial mechanics. The components of the microtensiometer and the individual measurement techniques are detailed below.

3.2.1 Components and Layout

The microtensiometer consists of an Omegadyne PX409-001GV pressure transducer in line with a capillary filled with oil or air and held at a specific pressure by a constant pressure head. The capillary is housed by a 3D-printed thermoplastic cell and is submerged in an aqueous solution reservoir. The oil or air forms a spherical cap at the tip of the capillary, which is imaged on Nikon T-300 inverted

light microscope with an attached Flea3 Monochrome GigE camera. Measurements of the pressure and radius are analyzed in LabView.

The thermoplastic cell used for all experiments is a design by Reichert and Walker.[7] The reservoir within the cell is lined with a PTFE ring, and the base is sealed with a 30 mm circular glass slide (Warner Instruments, Hamden, CT, model CS-30R) held in place with Loctite® marine epoxy. The top of the reservoir is open to the atmosphere for most experiments that last under an hour. To guard against evaporation in the case of experiments that last over an hour, a second circular glass slide is placed on the top of the cell reservoir. The capillary is held in place within the cell by a PEEK fitting with a tapered ferrule that seals the device and prevents leaks.

3.2.2 Capillary Preparation

Borosilicate glass capillaries are purchased from World Precision Instruments, Inc. (model TW 100-6) with dimensions of i.d.=0.75 mm, o.d.=1 mm, and L=150 mm, and are pulled to a tip radius of 35-50 μm using custom settings on a PMP-100 capillary puller (Micro Data Instrument Inc.). To ensure that the three phase contact line remains pinned at the tip of the capillary, the interiors of the capillaries are acid washed and coated with a hydrophobizing agent. The agent is drawn into the capillary from the end opposite the pulled tip to ensure only the capillary interior becomes hydrophobic. When the internal phase in the capillary is squalane (Chapters 4 and 5 and the Appendix), the hydrophobic Dynasylan® SIVOCLEAR (Evonik Industries, Essen, Germany) coating is applied. When the

internal phase is air (Chapters 6 and 7), a 2% solution of arylalkoxy silane XIAMETER® OFS-6124 (Dow Corning, Midland, MI) in ethanol is applied. After coating, the capillaries are rinsed with ethanol and are allowed to dry overnight in a 60 ^{o}C (SIVOCLEAR) or 110 ^{o}C (XIAMETER) oven before use.

3.2.3 Solution Exchange

Chapters 4-7 all involve exchange of the bulk solution in the reservoir via two ports connected to a peristaltic pump. The inlet and outlet ports contain glass capillaries that have been bent to approximately 120^{o} angles to direct fluid flow within the reservoir. The inlet port capillary lies parallel with the bottom glass plate of the reservoir, but the outlet port capillary is angled upwards to withdraw solution from the free air-water surface. This geometry ensures that a constant solution volume remains in the reservoir during the solution exchange despite small variations in the inlet and outlet flow rates. The full volume of the reservoir is 3 mL, but typically only 2 mL of solution is used to accommodate the outlet port capillary geometry. Details for exact flow rates and rinsing times are included in each chapter, but range from 0.1 to 0.4 mL/s. Rinsing is carried out for 10-20 residence times across all experiments to ensure complete replacement of the bulk fluid with new solution. The linear flow rate past the capillary tip is sufficiently small to yield a local Reynolds number that is always $Re = \frac{\rho U R}{\mu} < 3$, where ρ is the density of the bulk fluid, U is the linear fluid velocity past the interface, R is the interface radius, and μ is the bulk fluid viscosity. The capillary number of the

system is defined as $Ca = \mu U/\gamma$ and for this system, $Ca < 1x10^{-4}$, indicating there is no interfacial deformation expected due to flow.[8]

3.3 DYNAMIC SURFACE AND INTERFACIAL TENSION

The instantaneous surface tension is calculated from the Laplace equation for a spherical cap,

$$\gamma(t) = (P_1(t) - P_2)\frac{R(t)}{2} \ , \qquad (3.1)$$

where P_1 is the pressure inside the drop or bubble, P_2 is the hydrostatic pressure of the aqueous solution at the capillary, and R is the measured interface radius. P_2 is set by the height of the aqueous solution above the capillary. The uncertainty in the calculated surface tension is $\Delta\gamma = \pm 0.5$ mN/m due to the propagation of random errors in the pressure and radius measurements.

A clean interface is generated by activating a solenoid valve that temporarily switches P_1 to a higher pressure head (between 5000 – 6000 Pa). An air bubble or oil droplet is ejected from the capillary, creating a fresh interface. The ejected air bubble immediately rises to the reservoir surface, but the oil droplet must be manually swept away from the capillary tip with a sterile stainless steel needle.

Before surface active species are introduced into the reservoir, the cleanliness of the microtensiometer cell is tested by measuring the surface tension of a clean air/water interface. The cell is considered clean if the measured surface tension $\gamma = 72.8 \pm 1$ mN/m for at least 2000 seconds.

3.4 INTERFACIAL MECHANICS

For an irreversibly adsorbed species, the Gibbs modulus E_G is defined as

$$E_G = \frac{d\gamma}{d\ln\Gamma} = \frac{d\gamma}{d\ln A} \tag{3.2}$$

where A is the interfacial area and Γ is the surface concentration. The Gibbs modulus is measured in the microtensiometer by decreasing the pressure behind the oil drop or air bubble at a constant rate with a programmable syringe pump (BS-8000, Braintree Scientific, Inc). Specific compression rates are reported in individual chapters, but range from 6-15 Pa/s. Decreasing the pressure results in a decrease in the area of the spherical cap,

$$A = 2\pi R\left(R - \sqrt{R^2 - R_c^2}\right), \tag{3.3}$$

where R_c is the radius of the capillary. The Gibbs modulus is determined by first calculating the surface tension and surface area at each time step during the compression, then calculating the slope of surface tension versus the natural log of the surface area.

The dilatational modulus E is defined as

$$E = \frac{dP^S}{d\ln A} \tag{3.4}$$

where P^S is the surface excess normal stress. The dilatational modulus is measured via small amplitude oscillation of the spherical cap. The pressure behind the spherical cap is varied sinusoidally using a 100 µL syringe connected to an oscillating motor and piston described in detail by Alvarez *et al*.[9] Oscillations can be performed over a frequency range of 0.2 to 6 rad/s and an amplitude range of 50

to 150 Pa. All measurements presented in this work are performed at a frequency of 1.9 rad/s and an amplitude of 90 Pa.

The pressure and radius are recorded as a function of time during the oscillation. There is a small time lag between the pressure and radius measurements, which is accounted for by recording the value of the lag and shifting the radius time points accordingly. The magnitude of the dilatational modulus can be written in terms of the measured pressure and radius,[10]

$$|E^*| = \frac{b_1}{1-b_1}\left(\frac{R_{eq}}{\Delta R_1}\right)\left(\frac{P_a R_{eq}}{2}\right)\sqrt{\left(\frac{\Delta R_1}{R_{eq}}\right)^2 + 2\left(\frac{\Delta R_1}{R_{eq}}\right)\cos\phi_{R1} + 1}\ , \qquad (3.5)$$

where $b_1 = \sqrt{1-\left(\frac{R_c}{R_{eq}}\right)^2}$ and $\Delta R_1 = R_a\left(\frac{P_{eq}}{P_a}\right)$. P_{eq} is the equilibrium pressure, R_{eq} is the equilibrium radius of the interface, P_a is the amplitude of the pressure oscillations, R_a is the amplitude of the radial oscillations, and ϕ_{R1} is the phase angle of the radial oscillations. The data is analyzed using a fast Fourier transform in MATLAB® to find the primary frequency, amplitude and phase angle of the pressure and radius oscillations. The amplitude of any higher harmonics present in the data must be less than 10% of the amplitude of the primary harmonic for the small amplitude assumption to be valid. The reported uncertainty in the dilatational modulus is due to the propagation of random errors in the pressure and radius measurements.

REFERENCES

(1) Rosen, M. J. *Surfactants and Interfacial Phenomena*; 3rd Edition; Wiley-Interscience: New York, 2004.

(2) Ishigami, Y.; Gama, Y.; Nagahora, H.; Yamaguchi, M.; Nakahara, H.; Kamata, T. The pH-Sensitive Conversion of Molecular Aggregates of Rhamnolipid Biosurfactant. *Chemistry Letters*, **1987**, 763–766.

(3) Alvarez, N. J.; Walker, L. M.; Anna, S. L. A Criterion to Assess the Impact of Confined Volumes on Surfactant Transport to Liquid–fluid Interfaces. *Soft Matter* **2012**, *8*, 8917–8925.

(4) Russo, P. S.; Blum, F. D.; Ipsen, J. D.; Abul-Hajj, Y. J.; Miller, W. G. The Surface Activity of the Phytotoxin Cerato-Ulmin. *Can. J. Bot.* **1982**, *60*, 1414–1420.

(5) Ravera, F.; Santini, E.; Loglio, G.; Ferrari, M.; Liggieri, L. Effect of Nanoparticles on the Interfacial Properties of Liquid/liquid and Liquid/air Surface Layers. *J. Phys. Chem. B* **2006**, *110*, 19543–19551.

(6) Alvarez, N. J.; Walker, L. M.; Anna, S. L. A Microtensiometer to Probe the Effect of Radius of Curvature on Surfactant Transport to a Spherical Interface. *Langmuir* **2010**, *26*, 13310–13319.

(7) Reichert, M. D.; Walker, L. M. Interfacial Tension Dynamics, Interfacial Mechanics, and Response to Rapid Dilution of Bulk Surfactant of a Model Oil-Water-Dispersant System. *Langmuir* **2013**, *29*, 1857–1867.

(8) Alvarez, N. J.; Vogus, D. R.; Walker, L. M.; Anna, S. L. Using Bulk Convection in a Microtensiometer to Approach Kinetic-Limited Surfactant Dynamics at Fluid-Fluid Interfaces. *J. Colloid Interface Sci.* **2012**, *372*, 183–191.

(9) Alvarez, N. J.; Anna, S. L.; Saigal, T.; Tilton, R. D.; Walker, L. M. Interfacial Dynamics and Rheology of Polymer-Grafted Nanoparticles at Air-Water and Xylene-Water Interfaces. *Langmuir* **2012**, *28*, 8052–8063.

(10) Kotula, A. P.; Anna, S. L. Regular Perturbation Analysis of Small Amplitude Oscillatory Dilatation of an Interface in a Capillary Pressure Tensiometer. *J. Rheol.* **2015**, *59*, 85–117.

CHAPTER 4

SEQUENTIAL ADSORPTION OF AN IRREVERSIBLY ADSORBED NONIONIC SURFACTANT AND AN ANIONIC SURFACTANT AT AN OIL/AQUEOUS INTERFACE[*]

4.1 INTRODUCTION

Surfactants have a wide variety of applications in industry, including lubrication, detergency, and emulsion stabilization.[1] Often, surfactant mixtures are used to achieve desired system properties; understanding multi-component interactions at fluid-fluid interfaces is critical for improved formulation efficacy. One example of a multi-surfactant formulation is the dispersant used in response to oil spills in marine environments. After the 2010 Deepwater Horizon oil spill, nearly 2 million gallons of COREXIT® dispersant were applied to the oil slick at the air/water interface and at the leaking well head.[2] This dispersant is comprised of several nonionic and anionic surfactants in a solvent mixture. Its design is optimized to disperse oil in a slick at the surface through large scale tank tests and shake/flask tests.[3,4] The behavior of the specific components at the oil/water interface is still not well understood, and its efficacy during the Deepwater Horizon spill is still being evaluated.[5] Recent investigation into the dynamic interfacial behavior of several dispersant components has highlighted the complex interactions that govern dispersant effectiveness.[6] Future dispersant formulation and application depends on the development of a better understanding of component interactions at a variety of interfacial conditions.

---

[*] Reproduced in part with permission from *Langmuir* (DOI: 10.1021/la504969v). Copyright 2015 American Chemical Society.

The multi-component system considered in this study consists of Tween® 80 and Aerosol-OT (AOT), two main components in commercial dispersants. Tween 80 is a nonionic surfactant comprised of a branched poly(ethylene oxide) head and an oleic acid tail. The adsorption of Tween 80 at an oil/water interface has been shown to be partially irreversible.[7] When an interface coated with Tween 80 is rinsed with deionized water, the interfacial tension does not return to the clean oil/water value. Instead, the final steady-state rinsed value depends on the interfacial tension at the time of rinsing. Irreversible adsorption is observed in both deionized water and simulated sea water solutions, for Tween 80 concentrations ranging from 0.5 μM to 2.5 μM. It is possible that the interface is acting to fractionate more persistent species within the commercially available surfactant. However, irreversible adsorption is consistent with recent molecular simulations, due to interactions between poly(ethylene oxide) headgroups and the interface.[8]

AOT (dioctyl sodium sulfosuccinate) is an anionic surfactant that reversibly adsorbs to an oil/aqueous interface.[9,10] Unlike Tween 80, on rinsing with deionized water, all of the AOT is removed from the interface to within measurement error. The equilibrium interfacial tension depends on the ionic strength of the aqueous solution; the presence of counterions effectively screens the electrostatic repulsion of the negative head groups of the surfactant, resulting in lower interfacial tension values.[11–14] Lower interfacial tension implies a greater surface concentration of adsorbed surfactant.

In this study we quantify the adsorption behavior of Tween 80 and AOT using a sequential adsorption approach, where only one species is exposed to the

interface at a time. This approach is particularly useful when one or more components irreversibly adsorb to the interface, persisting even when the bulk concentration is changed. Sequential adsorption has previously been applied to pendant drop systems[9,15–17] and to study interactions on solid surfaces[18]. Here, the adsorption of AOT is measured on a squalane/aqueous interface that has been pre-exposed to a solution of Tween 80. Assuming that interfacial tension is an indirect measurement of surface coverage, this approach provides a probe of the degree of adsorption of different species at the oil/water interface. Systems are prepared in both deionized water and 0.5 M NaCl solution to examine the effect of ionic strength on AOT adsorption. Additional rinsing after exposure to AOT is performed to assess the effect of the secondary surfactant on the irreversibility of Tween 80 adsorption.

4.2 MATERIALS AND METHODS

Squalane ($C_{30}H_{62}$), a branched alkane, is used as the oil phase and is purchased from Sigma (St. Louis, MO) at 98% purity. Further purification is performed by gravity filtration through a glass column packed with 1.5g of basic activated alumina (Sigma, St Louis, MO). The oil is considered sufficiently clean if the squalane/deionized water interfacial tension remains constant (52.5 ± 1 mN/m) for at least 2000 seconds.

Tween 80 and Aerosol-OT are purchased from Sigma (St. Louis, MO) and are used without further purification. Tween 80, or polysorbate 80, has a polydisperse distribution of molecular structures originating from its synthesis.

Mass spectrometry has shown that structures of Tween 80 vary widely, sometimes including only partially ethoxylated sorbitan head groups, varying lengths of the poly(ethylene oxide) chains, and multiple oleate tails.[20,21] The structure of AOT is more uniform than Tween 80, although commercial samples can include acidic impurities that are produced during synthesis or created during hydrolysis.[22,23] Additionally, AOT is partially soluble in organic solvents, but is used here in the aqueous phase. We assume negligible partitioning of AOT into the oil phase during this study, due to the limited exposure times considered herein.

All samples used in this study are prepared via dilution from concentrated stock solutions in deionized water. The stock solution concentrations are 37 mM Tween 80 and 26 mM AOT. Both stock solutions have concentrations greater than ten times the critical micelle concentration of the surfactant (12 μM[24] and 2.5 mM[25], respectively). Dilutions are made in 50 mL VWR (Batavia, IL) centrifuge tubes that have been pre-rinsed with the surfactant solutions to minimize depletion effects to the walls of the sample cell.[26]

Deionized water is prepared with a Barnstead Ultrapure water purification system to 18.2 MΩ·cm resistivity. Sodium chloride is purchased from VWR (Batavia, IL) at 99% purity and is baked at 400 ºC for 5 hours to remove hydrates and impurities. A 2 M stock solution is prepared with deionized water immediately after baking.

A microtensiometer is used to measure the dynamic interfacial tension of the oil/water systems. Described in detail in Chapter 3 and elsewhere,[7,27–29] the device consists of an Omegadyne PX409-001GV pressure transducer in line with a

capillary filled with oil, held at a specific pressure by a constant pressure head. A 3D-printed thermoplastic cell has been designed to hold a capillary, which is submerged in an aqueous solution reservoir, and imaged on a Nikon T-300 inverted light microscope. The oil forms a spherical cap at the tip of the capillary. The radius of the cap is measured in real time with the pressure jump across the interface to determine the instantaneous interfacial tension, $\gamma(t)$, from the Laplace equation for a spherical cap[30]

$$\gamma(t) = (P_1(t) - P_2)\frac{R(t)}{2} \tag{4.1}$$

where P_1 is the pressure inside the oil cap, P_2 is the hydrostatic pressure of the aqueous solution at the capillary, and R is the measured interface radius.

The capillaries are purchased from World Precision Instruments, Inc. (Sarasota, FL) with dimensions of i.d.=0.75mm, o.d.=1mm, and L=150mm, and are pulled to a tip radius of 35-45μm using custom settings on a PMP-100 capillary puller (Micro Data Instrument Inc., South Plainfield, NJ). To ensure that the three phase contact line remains pinned at the tip of the capillary, the interiors of the capillaries are acid washed and coated with hydrophobic Dynasylan® SIVOCLEAR (Evonik Industries, Essen, Germany). Capillaries are rinsed with deionized water and acetone and are baked at 60 ^{o}C for 30 minutes prior to use.

Decreasing the pressure head behind the oil droplet at a constant rate of 6 Pa/s with a Braintree BS-8000 120 V programmable syringe pump reduces the interfacial area to generate a surface pressure versus surface area isotherm.

Exchange of the bulk aqueous solution is achieved by flowing a solution (deionized water, 0.5 M NaCl, or AOT solution) through the sample reservoir via

two ports connected to a peristaltic pump. Volumetric flow rates during rinsing average 0.46 mL/s. The residence time, τ, in the 3 mL reservoir is about 10 s, estimated by dividing the reservoir volume by the flow rate. To ensure complete replacement of the bulk fluid with new solution, rinsing is carried out for a minimum of 100 s for AOT solutions and 200 s for deionized water (10 or 20 residence times), at which point the interfacial tension has reached a constant value. Inlet and outlet flow rates are monitored closely to maintain a near constant reservoir volume and hydrostatic pressure, but slight variations lead to an increase in uncertainty in the measurement of interfacial tension. Without bulk fluid flow, the uncertainty in the calculated interfacial tension is $\Delta\gamma = \pm 0.5$ mN/m due to the propagation of random errors in the pressure and radius measurements[27]. With bulk fluid flow, the uncertainty increases to $\Delta\gamma = \pm 1$ mN/m.

The linear flow rate past the oil droplet in the capillary is sufficiently small to yield a local Reynolds number that is always $Re = \frac{\rho U b}{\mu} < 3$ for the droplet sizes considered here, where ρ is the density of the bulk fluid, U is the linear fluid velocity past the interface, b is the interface radius, and μ is the bulk fluid viscosity.[31] The capillary number of the system is defined as $Ca = \mu U/\gamma$ and for this system, $Ca < 1\text{x}10^{-4}$, indicating there is no interfacial deformation expected due to flow.

4.3 RESULTS

The initial step in studying the sequential adsorption of AOT onto a Tween 80 interface is to adsorb Tween 80 onto a clean interface. Figure 4.1 shows the dynamic interfacial tension of various concentrations of Tween 80 adsorbing to a

squalane/aqueous interface. To increase the rate of transport of Tween 80 to the interface, all concentrations are allowed to equilibrate in the presence of flow, with a bulk fluid flow rate of 0.39mL/s. Convection is shown to decrease the relevant length scale for diffusion and increase the rate of transport to the interface.[7,31] Each concentration ultimately reaches a static interfacial tension value, at which point the bulk solution is exchanged with deionized water. The residence time is less than 10 seconds, and we expect complete exchange of the bulk solution after a few residence times. This results in an increase in the value of interfacial tension as the Tween 80 partially desorbs from the interface, in agreement with the desorption phenomenon previously observed at a squalane/aqueous interface.[7]

The ultimate value of interfacial tension reached, γ_∞, is seen to be a function of the bulk concentration. For example, for the 5 μM Tween 80 bulk concentration, the interfacial tension decreases from a clean value of 52.5 ± 0.5 mN/m to a value of 13.7 ± 1 mN/m. At 650 seconds, the reservoir is exchanged with deionized water, and the interfacial tension increases to a value of 18.2 ± 1 mN/m. For the two lower bulk concentrations, the interfacial tension decreases to values of 22.7 ± 1 mN/m and 28.2 ± 1 mN/m, but increases to 24.8 ± 1 mN/m and 29.4 ± 1 mN/m after exchange of the bulk with deionized water. The bulk solution exchange with deionized water occurs at longer times for the lower concentrations, 1400 seconds and 2400 seconds for 0.25 μM and 0.05 μM, respectively, to allow the interfacial tension to reach a constant value before rinsing begins.

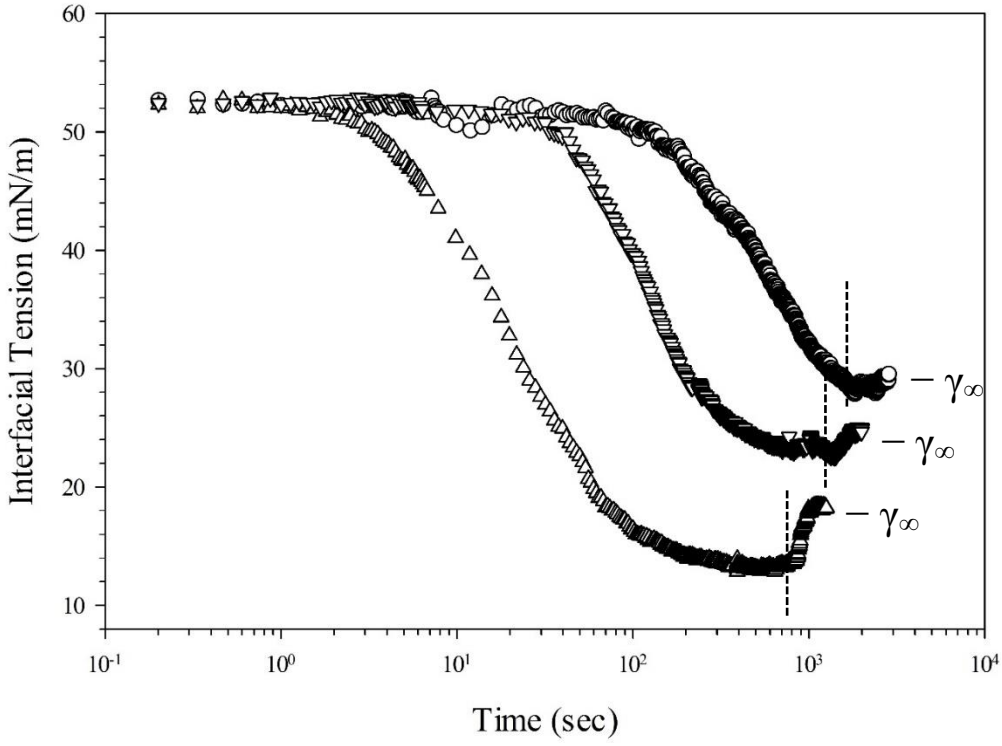

Figure 4.1: Dynamic interfacial tension versus time for Tween 80 solutions. Symbols represent concentrations of 0.05 µM (○), 0.25 µM (▽), and 5 µM (△) at a bulk fluid flow rate of 0.39 mL/s. Increases in interfacial tension at long times are due to rinsing with deionized water, which begins at times indicated by the dashed lines.

From the late-time interfacial tension values, γ_∞, an effective isotherm is generated based on the irreversibly-adsorbed portion of Tween 80. Figure 4.2 shows the surface pressure of a Tween 80 coated interface before and after being rinsed with deionized water, as a function of initial bulk concentration. Surface pressure for Tween 80 is defined as $\Pi = \gamma_0 - \gamma_\infty$, where γ_0 is the interfacial tension of the clean squalane/water interface, 52.5 ± 0.5 mN/m, and γ_∞ is the interfacial tension of the irreversibly adsorbed Tween 80 interface after rinsing with deionized water. For this range of bulk concentrations, the interfacial tension after rinsing

with deionized water is higher than it is prior to rinsing, indicating that some material desorbs from the interface. Although the system is no longer at equilibrium with a bulk surfactant solution, the surface coverage is estimated using the Gibbs equation for the maximum surface coverage (Γ_∞) of a nonionic surfactant,[32] given by

$$\Gamma_\infty = \frac{1}{nRT}\frac{d\Pi}{d\ln(C)} \tag{4.2}$$

where C is bulk surfactant concentration, Π is the surface pressure, R is the gas constant, and T is temperature. The integer n accounts for charge interactions for ionic surfactants, and has a value of $n = 1$ for nonionic species.[33] Equation (4.2) is valid at high surfactant concentrations approaching the CMC (12 μM for Tween 80),[24] where the slope of the surface pressure, Π, versus bulk concentration, C, on a semi-log plot approaches a constant value.

Applied to the isotherms shown in Figure 4.2, equation (4.2) provides an estimate of the maximum surface coverage of the irreversibly adsorbed portion of Tween 80. The maximum surface coverage of the irreversibly adsorbed Tween 80 with deionized water in the bulk is $\Gamma_\infty = 1.21 \pm 0.13$ μmol/m^2, corresponding to a minimum area of 137.1 ± 14.2 Å^2/molecule for high concentrations of Tween 80. The maximum surface coverage of Tween 80 prior to rinsing is $\Gamma_\infty = 1.45 \pm 0.12$ μmol/m^2; the higher surface concentration before rinsing again indicates that some Tween 80 desorbs from the interface upon being rinsed with deionized water. It should again be noted that the values of surface coverage of the irreversibly adsorbed portion of Tween 80 are only estimates, obtained by applying equation (4.2) to a non-equilibrium system.

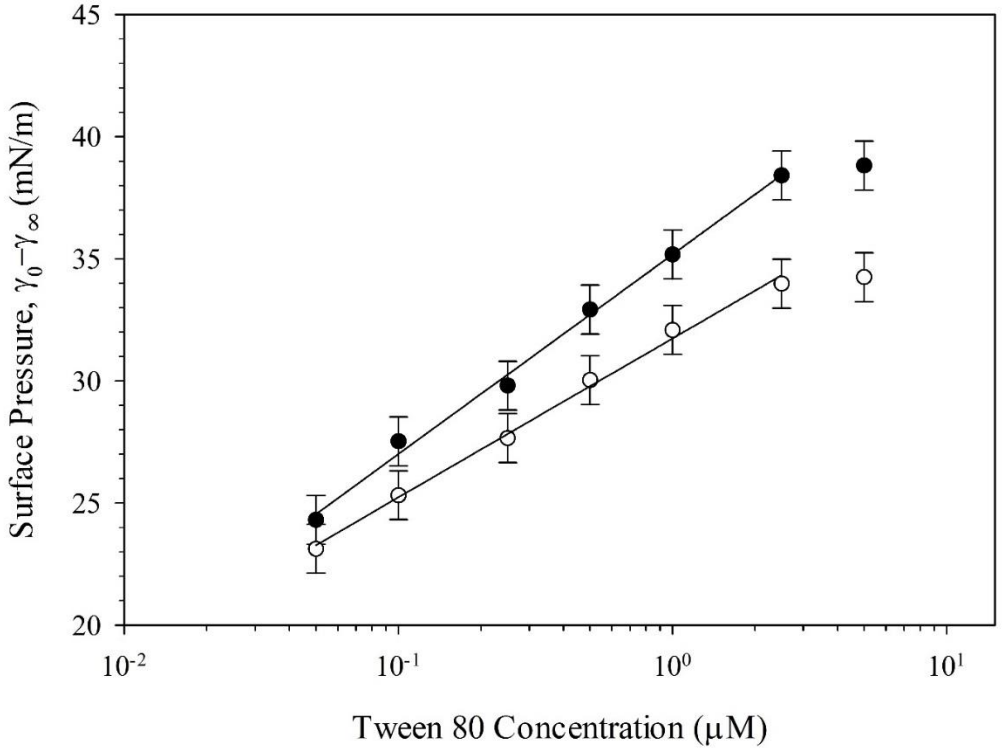

Figure 4.2: Surface pressure as a function of Tween 80 bulk concentration before (●) and after (○) being rinsed with deionized water. The surface pressure decreases after being rinsed with deionized water as some Tween 80 desorbs from the interface. The lines are best fits of equation (4.2) to the data.

To estimate surface coverage at lower values of interfacial coverage, low concentration equilibrium data is required to fit an isotherm model (such as the generalized Frumkin isotherm) to the data. The time scales required to achieve equilibrium at concentrations lower than those reported here exceed instrumental limitations, even using convection to enhance transport. Instead, to estimate the average area/molecule at lower values of interfacial coverage, a surface pressure versus surface area isotherm is generated by compressing a Tween 80 coated interface. To obtain low interfacial coverages, a 1 μM solution of Tween 80 is allowed to adsorb for a prescribed amount of time before the bulk solution is

exchanged with deionized water; rinsing occurs before the system reaches an equilibrium interfacial tension. Tween 80 irreversibly adsorbs to the interface, proportional to the interfacial tension after rinsing, γ_∞. The pressure head behind the oil droplet is then reduced at a constant rate and the interfacial area decreases in response to the lower pressure. Since the species on the interface remains irreversibly adsorbed, decreasing the interfacial area compresses the species on the interface, reducing the surface area per molecule and increasing the surface pressure. This method has been used to measure the surface pressure versus area isotherms of irreversibly adsorbing proteins at oil/water interfaces[17] as well as insoluble surfactants at air/water interfaces, and the results obtained agree well with experiments performed by compressing monolayers on a Langmuir trough.[34] Figure 4.3(a) shows the surface pressure as a function of surface area for several initial interfacial coverages (values of interfacial tension) of Tween 80. Measured areas are scaled horizontally by a parameter χ to generate a single curve, where χ is chosen for each initial interfacial tension. Without explicit knowledge of the Tween 80 interfacial coverage at each interfacial tension, the horizontal scaling is chosen such that the highest concentrations of Tween 80 have an initial area/molecule of 137.1 $Å^2$/molecule, corresponding to the maximum interfacial coverage of the irreversibly adsorbed component of Tween 80 found from equation (4.2). Figure 4.3(b) shows the collapsed surface pressure curves as a function of the scaled surface area for the irreversibly adsorbed portion of Tween 80.

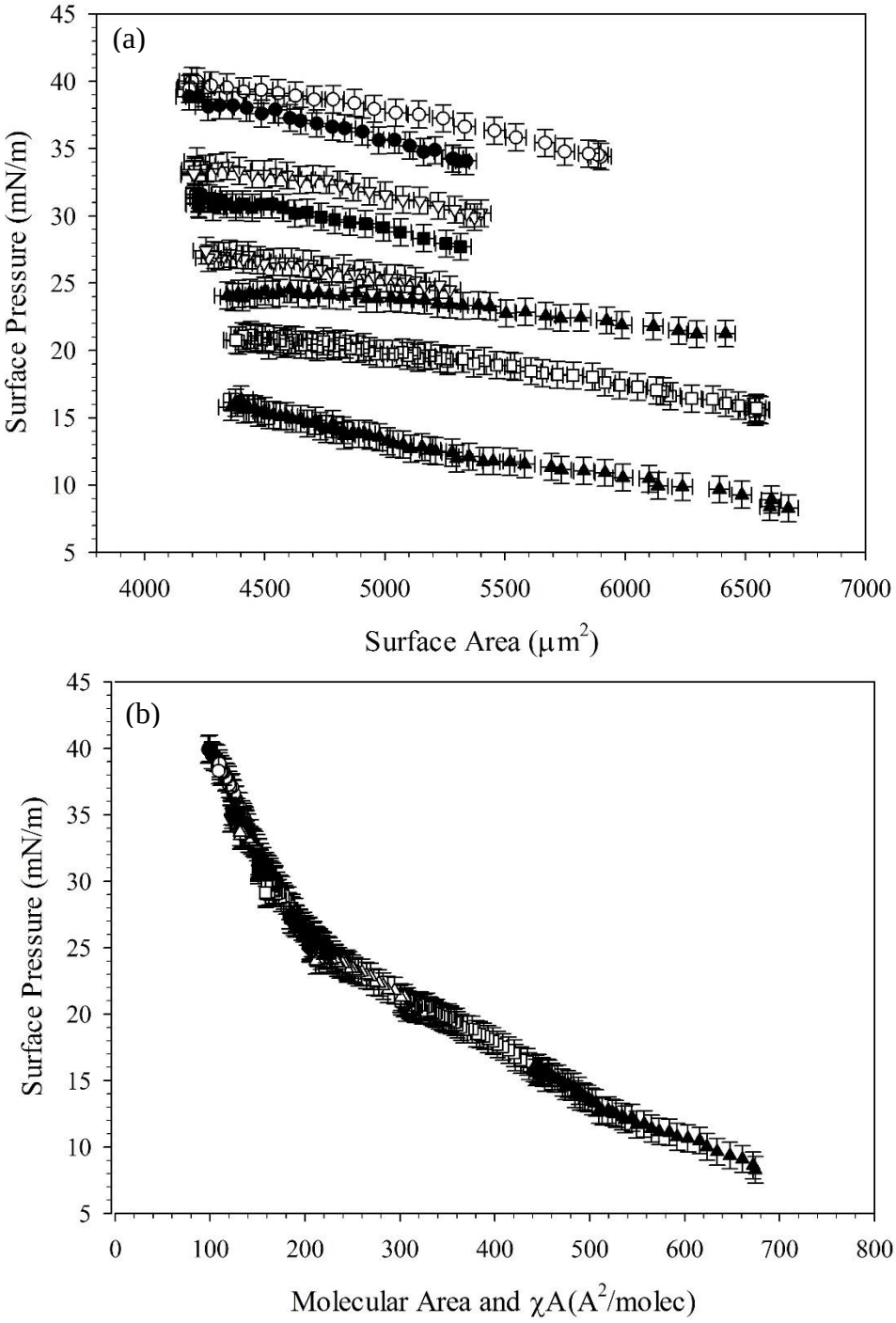

Figure 4.3: (a) Surface pressure as a function of surface area for several initial interfacial tension values of Tween 80 coated interfaces: γ_∞= 44.2 ± 1 mN/m (□), γ_∞= 36.9 ± 1 mN/m (■), γ_∞= 31.2 ± 1 mN/m (◇), γ_∞= 28.0 ± 1 mN/m (◆), γ_∞= 24.8 ± 1 mN/m (△), γ_∞= 22.3 ± 1 mN/m (▼), γ_∞= 18.4 ± 1 mN/m (○), γ_∞= 18.4 ± 1 mN/m (●)(b) The isotherms from (a) scaled by a constant horizontal shift factor χ to collapse onto a single master curve, anchored by the maximum interfacial coverage value estimated from equation (4.2), 137.1 Å^2/molecule.

The value of χ^{-1} is approximately equal to the number of Tween 80 molecules on the interface. χ^{-1} ranges from 9.9 x 10^8 molecules for a measured interfacial area of 6687 ± 41 μm^2 for the lowest initial surface pressure of 8.8 ± 1 mN/m to 4.3 x 10^9 molecules for a measured interfacial area of 5899 ± 34 μm^2 for the highest initial surface pressure of 34.3 ± 1 mN/m.

The horizontal scaling of the surface pressure data also allows the area per molecule values for low surface pressures of Tween 80 to be determined. The analysis relies on the assumption that equation (4.2) can be applied to estimate the maximum interfacial coverage of the irreversibly adsorbed portion of Tween 80. Figure 4.4 shows the estimated Tween 80 surface coverage, Γ, as a function of the interfacial tension of Tween 80 after rinsing with deionized water, γ_∞. Since each value of χ^{-1} is approximately equal to the number of molecules on the interface for a given initial interfacial coverage, Γ is estimated for each value of interfacial tension as $\Gamma = \frac{1}{N_A \chi A_0}$, where N_A is Avogadro's constant and A_0 is the initial surface area before compression. This analysis is based on the assumption that the Gibbs equation can be applied in the high concentration limit of Figure 4.2 to estimate Γ_∞. As long as the assumption holds, we are able to convert from interfacial tension values to surface concentrations of the irreversibly adsorbed portion of Tween 80 without the use of any isotherm model. Even if the assumption is not valid, the analysis provides at least an estimate of the surface coverage across various interfacial tension values.

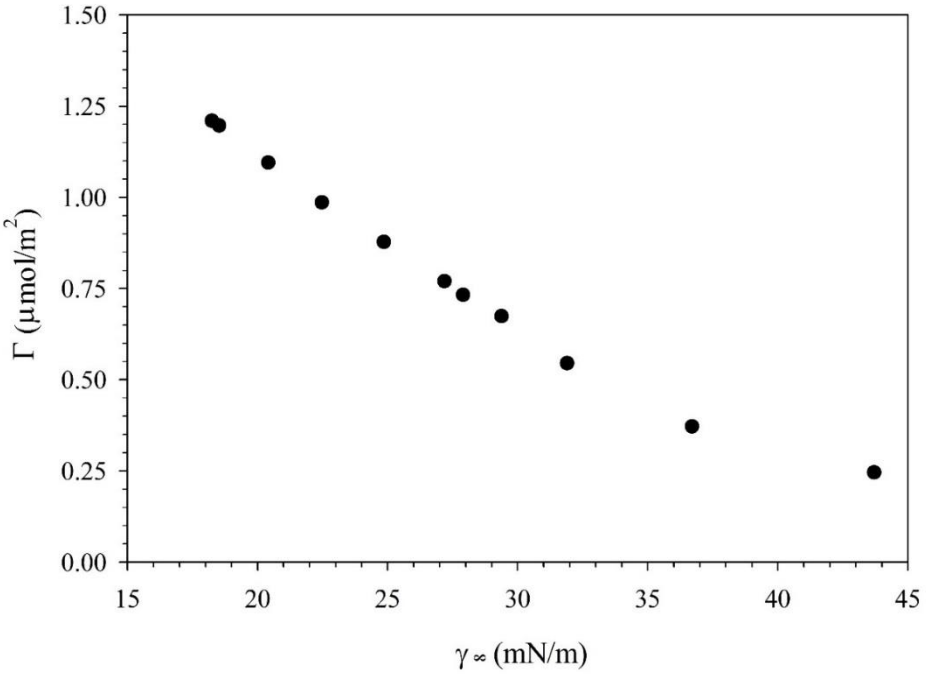

Figure 4.4: Estimated surface coverage of the irreversibly adsorbed component of Tween 80 as a function of interfacial tension after the bulk surfactant solution has been exchanged with deionized water.

With the irreversible Tween 80 adsorption characterized, a second surfactant (AOT) is introduced to an interface that has been pre-coated with Tween 80. A multistage protocol has been designed to interrogate adsorption with only one species in the bulk solution at a time. The dynamic interfacial tension for the sequential adsorption of Tween 80 and AOT on a squalane/aqueous interface is shown in Figure 4.5. In the first stage, a clean squalane droplet is exposed to 1μM Tween 80 bulk solution. The interfacial tension decreases from the clean oil/water value of 52.5 ± 0.5 mN/m as Tween 80 adsorbs to the oil/water interface, similar to the behavior seen in Figure 4.1. However, instead of allowing the system to equilibrate as is done in Figure 4.1, the bulk surfactant solution is exchanged with deionized water in Stage 2, after 150 seconds. Rinsing with deionized water before

equilibrium is reached limits the amount of Tween 80 that can adsorb at the oil/water interface. The adsorption of additional Tween 80 stops as all surfactant is removed from the bulk. There is an irreversibly adsorbed component of Tween 80 present at the oil/water interface, and the interfacial tension of the system remains constant at 34.5 mN/m ± 1 mN/m upon rinsing. No Tween 80 desorbs into the clean aqueous phase. Using the analysis in Figure 4.4, the surface coverage of Tween 80 at this stage of the experiment is $\Gamma = 0.43$ μmol/m^2.

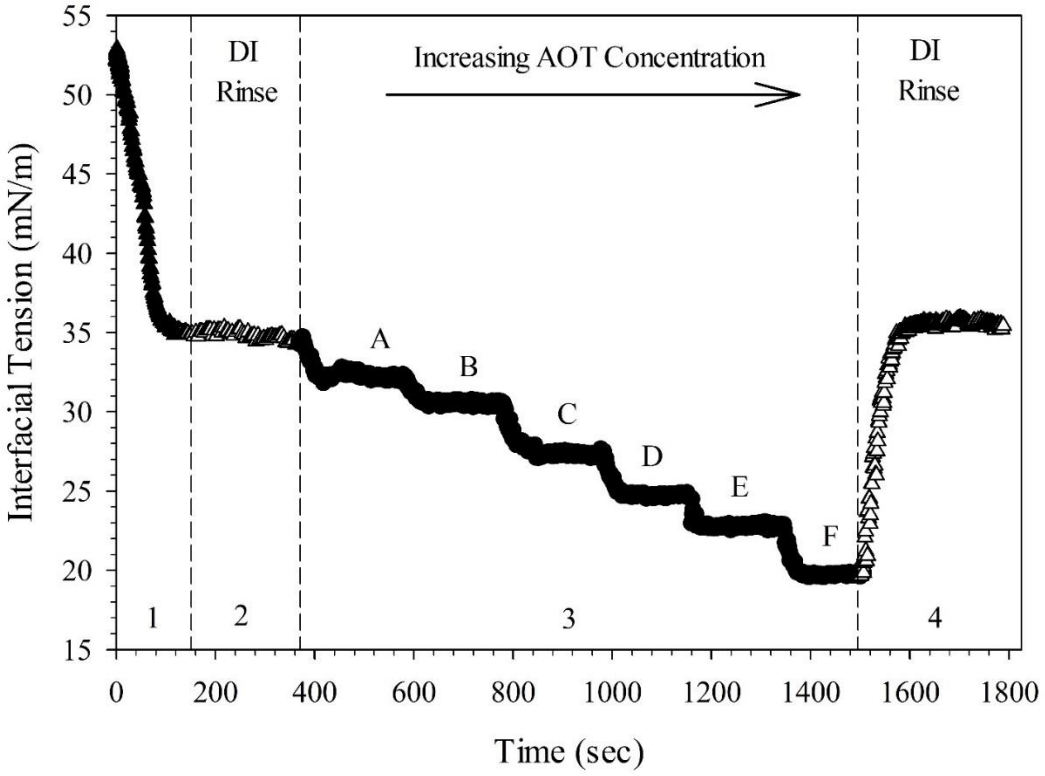

Figure 4.5: Dynamic interfacial tension at a squalane/aqueous interface during a sequential adsorption of surfactant from solution. The bulk solutions in the various stages are: 1μM Tween 80 (Stage 1), deionized water (Stage 2), a series of AOT concentrations of 0.010 mM (A), 0.032 mM (B), 0.100 mM (C), 0.178 mM (D), 0.320 mM (E), and 0.420 mM (F) (Stage 3), deionized water (Stage 4).

After exposing the Tween 80 coated interface to deionized water for at least 200 seconds to ensure no desorption occurs, 0.01 mM AOT is introduced to the

sample reservoir, replacing the deionized water (step A). The interfacial tension decreases as AOT adsorbs to the pre-coated Tween 80 interface. Note that the bulk solution is exchanged for at least 10 residence times to ensure the reservoir concentration has reached that of the rinsing solution, and the interfacial tension is monitored until a steady state value is reached. Subsequent steps B-F shown in Figure 4.5 correspond to step changes in the bulk solution with increasingly concentrated solutions of AOT. In each case, a higher concentration of AOT further decreases the interfacial tension. Each new concentration of AOT remains in the bulk for at least 200 seconds, until the interfacial tension reaches a constant value, before the next bulk AOT concentration is introduced into the reservoir. At the end of the sequence, the interfacial tension is lowered to a value of 19.6 mN/m, with a mix of AOT and Tween 80 on the interface. At this point, the bulk solution is still expected to contain only AOT.

To investigate the desorption of AOT from the mixed interface, the AOT solution is rinsed out of the sample reservoir and replaced with deionized water in Stage 4. This causes an increase in interfacial tension as there is desorption from the interface, which we assume to be primarily a result of AOT desorption. The final interfacial tension returns to a value near that of the Tween 80 interfacial tension observed prior to the introduction of AOT, $\gamma = 35.3 \pm 1$ mN/m. This value is within uncertainty of the value reached by the initial adsorption of Tween 80 to the clean interface after rinsing (Stage 2), suggesting that the irreversibly adsorbed component of Tween 80 remains adsorbed at the interface while the AOT completely desorbs from the interface.

Figure 4.5 is a representative example of the sequential adsorption method we have developed. A 1 μM Tween 80 solution is consistently used in Stage 1, but the deionized water exchange in Step 2 occurs at different times (ranging from 60 to 1200 seconds) to control the interfacial coverage of Tween 80, as determined by the value of interfacial tension at rinsing, γ_∞. In all cases, the bulk exchange is maintained for at least 200 seconds to ensure the interfacial tension value has reached a constant value before AOT is introduced to the system.

Treating the irreversibly adsorbed Tween 80 as a permanent layer onto which the AOT adsorbs, we define a surface pressure $\Pi = \gamma_\infty - \gamma_{AOT}$, where γ_∞ is the interfacial tension after the Tween 80 adsorbs and is rinsed with deionized water (Stage 2 in Figure 4.5), and γ_{AOT} is the steady state interfacial tension reached after AOT is introduced to the system at each stage (A-F in Figure 4.5), which is a function of the bulk concentration of AOT. In the case of a clean oil/water interface with no Tween 80 present, γ_∞ is taken as the clean squalane/water interfacial tension of 52.5 ± 0.5 mN/m. The steady state interfacial tension values are used to generate an effective isotherm of AOT adsorption onto different interfaces: both clean and those pre-coated with different amounts of Tween 80.

Figure 4.6 shows the surface pressure, $\Pi = \gamma_\infty - \gamma_{AOT,}$ as a function of the bulk AOT concentration on interfaces coated with different amounts of Tween 80. The amount of Tween 80 on the interface is defined by the interfacial tension after rinsing with deionized water, γ_∞. This value is varied by rinsing at different times during the initial adsorption of Tween 80. The smaller the initial value of γ_∞, the more material is expected to be present on the interface. For any value of γ_∞,

increasing the AOT concentration in the bulk results in increasing values of surface pressure, suggesting a corresponding increase in AOT adsorption.

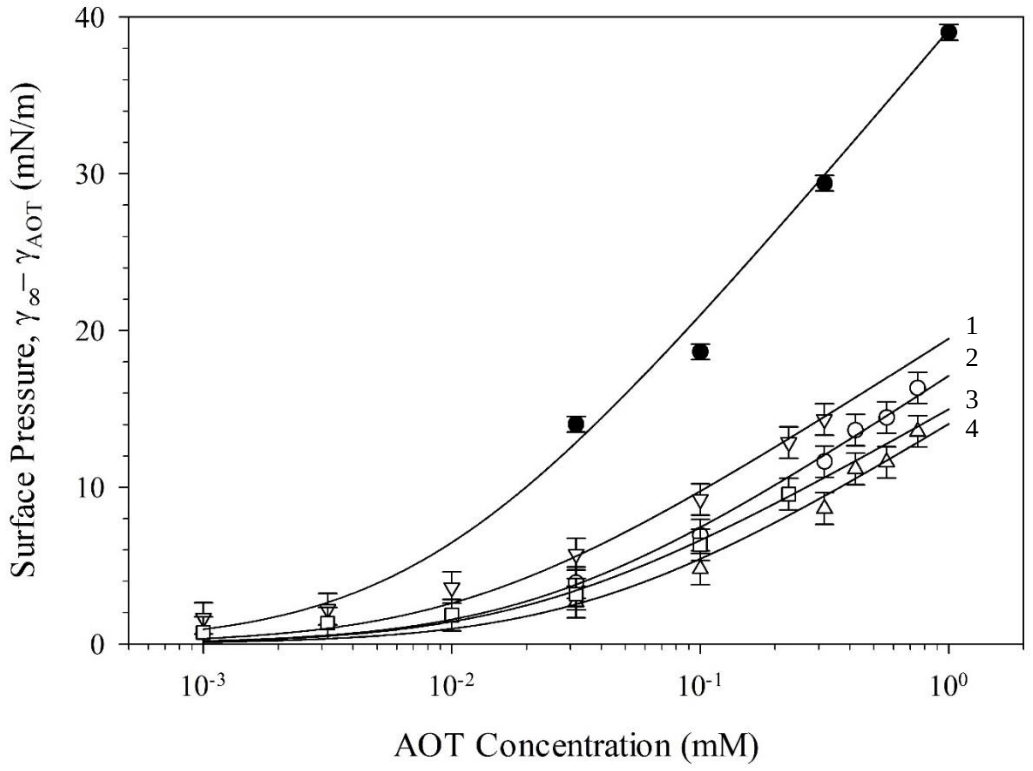

Figure 4.6: Effective AOT adsorption isotherms on a squalane/aqueous interface pre-coated with Tween 80: γ_∞=37.8 ± 1 mN/m (Γ=0.36μmol/m^2) (▽,Line 1), γ_∞=34.5 ± 1 mN/m (Γ=0.43μmol/m^2) (○, Line 2) γ_∞=30.6 ± 1 mN/m (Γ=0.58μmol/m^2) (△, Line 4), γ_∞=29.7 ± 1 mN/m (Γ=0.73μmol/m^2) (□, Line 3) , and a clean squalane/deionized water interface (●). Lines are best fits of equation (4.4) to each data set.

To parameterize the AOT adsorption, a simple model is chosen to fit the data shown in Figure 4.6. The solid lines represent a fit to the Langmuir isotherm model, given by

$$\frac{\Gamma}{\Gamma_\infty} = \frac{C}{a + C} \tag{4.3}$$

$$\Pi = \gamma_\infty - \gamma = nRT\Gamma_\infty \ln(1 + \frac{C}{a}) \tag{4.4}$$

where C is the bulk AOT concentration, a is the ratio of the desorption rate to the adsorption rate, Π is the surface pressure, R is the gas constant, and T is temperature. The integer n accounts for counterion adsorption of charged species and has a value of $n = 1$ in 0.5 M NaCl solution and $n = 2$ for deionized water solutions with no excess salt.[24] Γ is the molar coverage of AOT on the interface, and Γ_∞ is the maximum AOT coverage, which is estimated from equation (4.2). Since the CMC of AOT is 2.5 mM,[25] this limit is approached in Figure 4.6.

The surface pressure for a specific bulk concentration of AOT depends on the amount of Tween 80 already present on the interface. For interfaces with low Tween 80 coverage (larger values of γ_∞), the addition of AOT results in a larger increase in surface pressure for a given bulk concentration than for interfaces where Tween 80 has more completely saturated the interface (lower values of γ_∞). The surface pressure for a given concentration of AOT adsorbed to an interface with no Tween 80 present is over 200% greater than any of the pre-coated Tween 80 interfaces.

Each of the AOT adsorption isotherms shown in Figure 4.6 is generated using the sequential adsorption methodology described in Figure 4.5. The Langmuir isotherm model is fit to each series of AOT concentrations exposed to a single interface coated with Tween 80 to minimize variations in the initial Tween 80 coverage. To verify that the AOT adsorption depends only on the Tween 80 interfacial tension, γ_∞, and not the sequential increase of AOT concentrations, the multi-step adsorption procedure of Figure 4.5 is repeated with single AOT concentration steps in Figure 4.7. The dynamic interfacial tension is shown for the

sequential adsorption of Tween 80 and AOT at a squalane/aqueous interface. Stages 1 and 2 are similar to those described in Figure 4.5. In stage 3, only one concentration of AOT is exposed to the pre-coated Tween 80 interface before the deionized water rinse in Stage 4. The steady state interfacial tension values in Stage 3 are used to generate an effective isotherm of AOT adsorption in Figure 4.8.

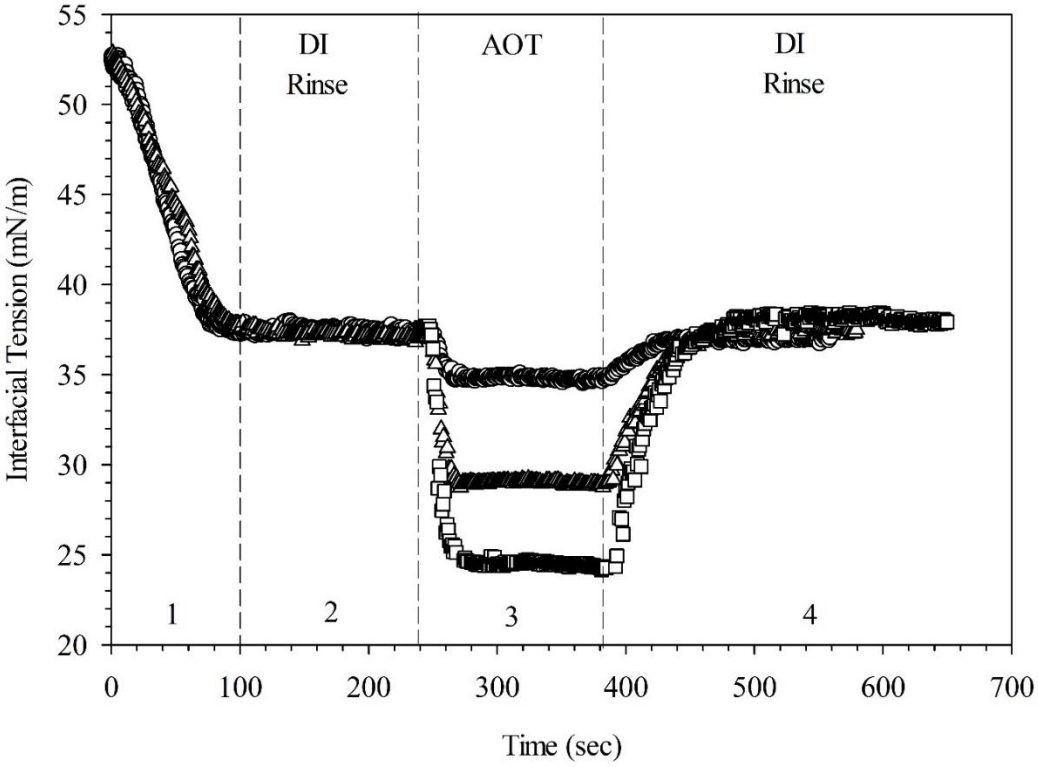

Figure 4.7: Dynamic interfacial tension at a squalane/aqueous interface during a sequential adsorption of surfactant from solution. Experimental conditions are similar to those described in Figure 4.5, but only one concentration of AOT is exposed to the Tween 80 coated interface before the deionized water rinse in Stage 4. Three AOT concentrations are shown in Stage 3: 0.01mM (○), 0.10mM (△), and 0.32mM (□).

The surface pressure values obtained through single-concentration AOT exposure steps are equivalent within uncertainty to the surface pressure values obtained through the multi-concentration AOT sequence in Figure 4.5. The small

deviations seen for some AOT concentrations are likely due to slight variations in initial Tween 80 interfacial coverage between runs, since a new Tween 80 coated interface had to be created for each AOT concentration.

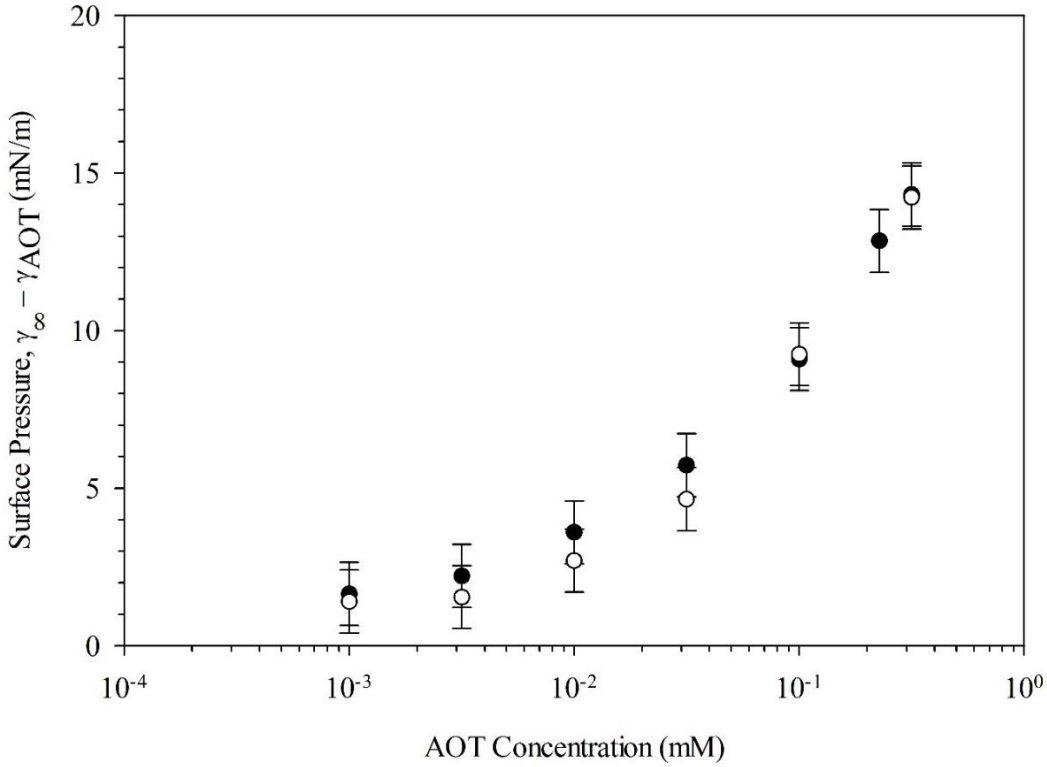

Figure 4.8: Effective AOT adsorption isotherms on a squalane/aqueous interface pre-coated with Tween 80. Filled symbols represent surface pressure of a multi-concentration sequence of AOT on Tween 80 $\gamma_\infty = 37.8 \pm 1$ mN/m. Empty symbols represent surface pressure of single-concentration AOT exposures shown in Figure 4.7 on Tween 80 with an average interfacial tension value after rinsing of $\gamma_\infty = 37.2 \pm 1$ mN/m.

The same AOT adsorption behavior in deionized water is also observed at high ionic strengths in the aqueous phase. Figure 4.9 shows the surface pressure as a function of AOT concentration in a 0.5 M NaCl bulk solution. For a clean squalane/0.5 M NaCl solution interface, $\gamma_0 = 55.0 \pm 0.5$ mN/m. This value is slightly higher than the clean squalane/deionized water interfacial tension value, which is expected, as salt increases the interfacial tension of oil/water interfaces.[35] As in the

deionized water systems, the surface pressure increases with AOT concentration at all values of Tween 80 coverage. Equivalent surface pressures are reached in 0.5 M NaCl solution at much lower AOT concentrations than in deionized water solution. For example, a surface pressure of 15 mN/m requires a bulk AOT concentration of at least C = 0.3 mM in deionized water, but only C = 0.0015 mM in 0.5 M NaCl solution. This is due to the addition of counterions that screen the repulsive electrostatic charges between AOT headgroups on the interface and increase adsorption. The Debye length of a 0.0015 mM AOT solution, for example, defined as[30] $\kappa^{-1} = \sqrt{\frac{\varepsilon\varepsilon_0 kT}{2000 N_A e^2 I}}$, where N_A is Avogadro's constant, I is the ionic strength of the solution, ε is the dielectric constant of the solution, ε_0 is the dielectric permittivity of free space, k is the Boltzmann constant, T is the temperature, and e is the electronic charge, decreases from hundreds of nanometers in deionized water down to 1.5 nm in 0.5 M NaCl.

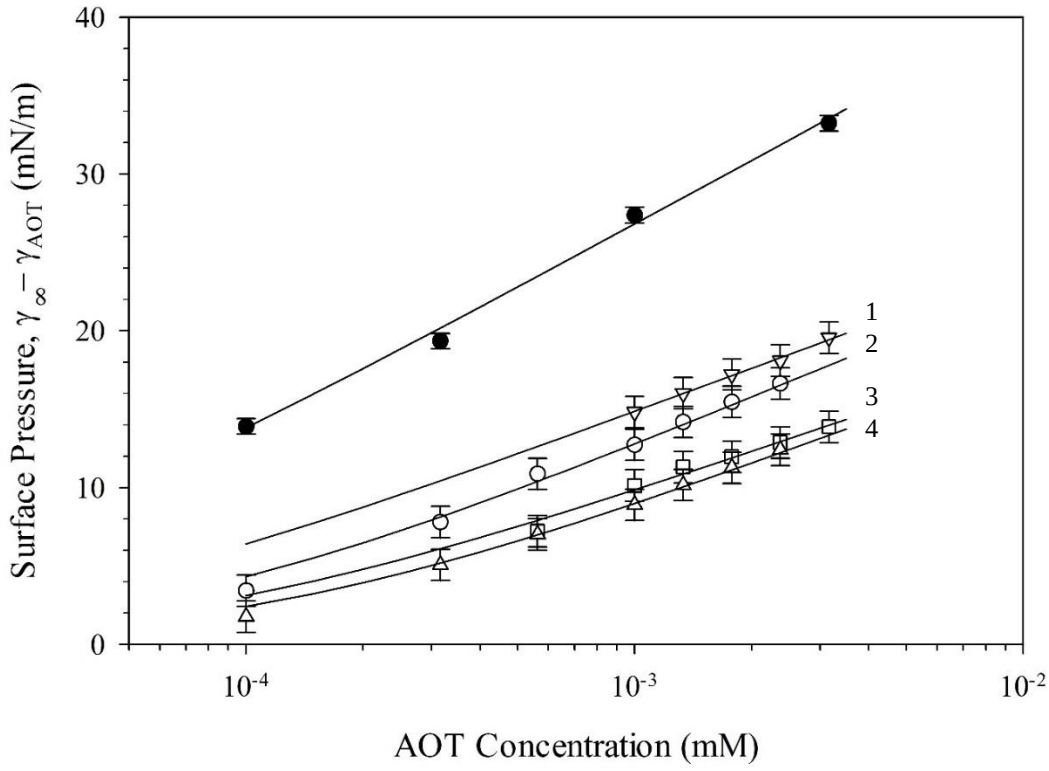

Figure 4.9: Effective AOT adsorption isotherms in a 0.5 M NaCl solution on squalane interfaces pre-coated with Tween 80: γ_∞ = 38.9 ± 1 mN/m (Γ=0.39μmol/m^2) (▽, Line 1), γ_∞ = 36.3 ± 1 mN/m (Γ=0.46μmol/m^2) (○, Line 2), γ_∞ = 32.4 ± 1 mN/m (Γ=0.63μmol/m^2) (□, Line 3), γ_∞ = 31.2 ± 1 mN/m (Γ=0.70μmol/m^2) (△, Line 4), and a clean squalane/0.5 M NaCl solution interface (●). Lines are fits of Equation (4.4) to each data set.

To quantify the amount of AOT on the interface, equation (4.2) is applied in the linear limit of each isotherm at high AOT concentration to find the maximum apparent surface coverage of AOT on the interface, Γ_∞. Figure 4.10 shows the effective maximum surface coverage of AOT, Γ_∞, in 0.5 M NaCl and deionized water solutions as a function of the coverage of Tween 80 initially irreversibly adsorbed on the interface. The Tween 80 surface concentrations are estimated from Figure 4.4, converting measured interfacial tensions, γ_∞, to surface coverages, Γ, in the manner described previously.

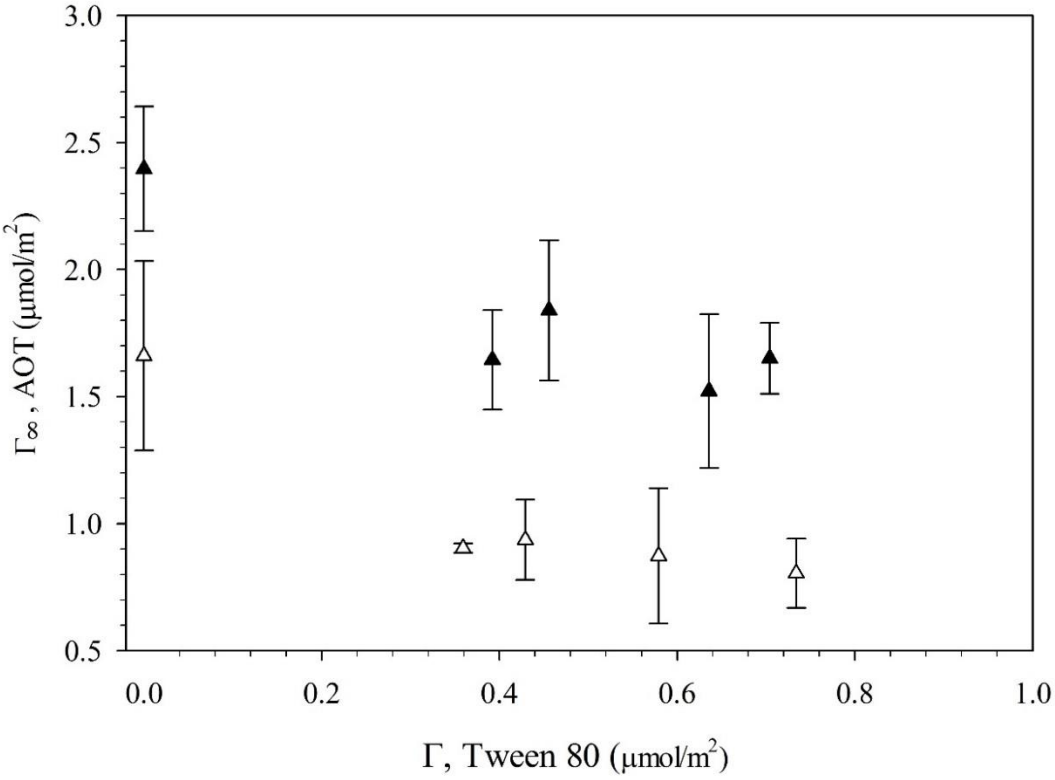

Figure 4.10: Maximum surface concentration of AOT on squalane/aqueous interfaces in 0.5 M NaCl solution (▲) and deionized water (△). AOT adsorption on a clean oil/water interface is shown above as Tween 80 $\Gamma = 0$. Error bars represent 95% confidence intervals on Γ_∞ from Equation (4.2).

In Figure 4.10, there is a noticeable decrease in the maximum coverage from AOT adsorption on a clean oil/water interface for both deionized water and 0.5 M NaCl solutions. The AOT maximum packing on a clean oil/water interface is $\Gamma_\infty = 2.40 \pm 0.25$ μmol/m^2 in 0.5 M NaCl, and $\Gamma_\infty = 1.66 \pm 0.37$ μmol/m^2 in deionized water. These values are comparable to those previously reported for AOT adsorption on an alkane/aqueous interface in 0.1 M NaCl.[10] The maximum surface coverage values of AOT on a clean oil/water interface are 130 - 200% larger than the values of maximum surface coverage on a Tween 80-coated interface,

indicating that the irreversibly adsorbed Tween 80 is changing the behavior of AOT adsorption.

The maximum packing concentration of AOT is higher with increasing ionic strength, due to the counterion screening effect. The maximum surface coverage of AOT on a clean aqueous/squalane interface in 0.5 M NaCl solution is 150% higher than in deionized water. On interfaces that have been coated with Tween 80, the maximum surface coverage of AOT in salt solution is 190% higher than in deionized water. At both ionic strengths, the maximum surface coverage of AOT is independent of the amount of Tween 80 on the interface; the presence of any Tween 80 on the interface reduces the maximum surface coverage to approximately the same value. This effect might be explained by the relatively small range of Tween 80 interfacial coverages for the interfaces exposed to AOT. Over the interfacial tension range of Tween 80 interfaces exposed to AOT, γ_∞ = 29.1 mN/m to γ_∞ = 38.9 mN/m, the area per molecule ranges from 250 to 500 $Å^2$/molecule, or Γ = 0.33 to 0.66 μmol/m^2, as found from Figure 4.4. Compared with the maximum packing concentration of irreversibly adsorbed Tween 80 estimated from Figure 4.2, (Γ_∞ = 1.21 ± 0.094 μmol/m^2), the probed Tween 80 coverage only varies from 27.4 to 54.8% of the maximum coverage. This leaves a substantial fraction of the interface available for AOT adsorption, and might explain the lack of impact that the specific Tween 80 concentration has on the maximum packing concentration of AOT.

As shown in Figure 4.5, rinsing the system with deionized water after AOT adsorption returns the interfacial tension to a value near the initial interfacial tension $\gamma_{\infty,}$ representing the irreversibly adsorbed amount of Tween 80 on the interface. Figure 4.11 shows the surface pressure after the second deionized water rinse as a function of bulk AOT concentration. A surface pressure of zero after rinsing indicates that the interfacial tension has returned to the initial Tween 80 post-rinse interfacial tension value, γ_{∞}, and suggests that all of the reversibly adsorbed AOT has been removed from the interface. The surface pressure returns to zero within uncertainty for all bulk AOT concentrations below 0.5 MM, indicating that low concentrations of AOT are unable to substantially displace Tween 80 from the interface. A negative surface pressure is observed at high AOT concentrations that approach the CMC, indicating that up to 10% of the initially adsorbed Tween 80 may have been removed from the interface. This demonstrates that although AOT is able to adsorb on the Tween 80 coated interface, it is not effective in removing Tween 80 upon rinsing.

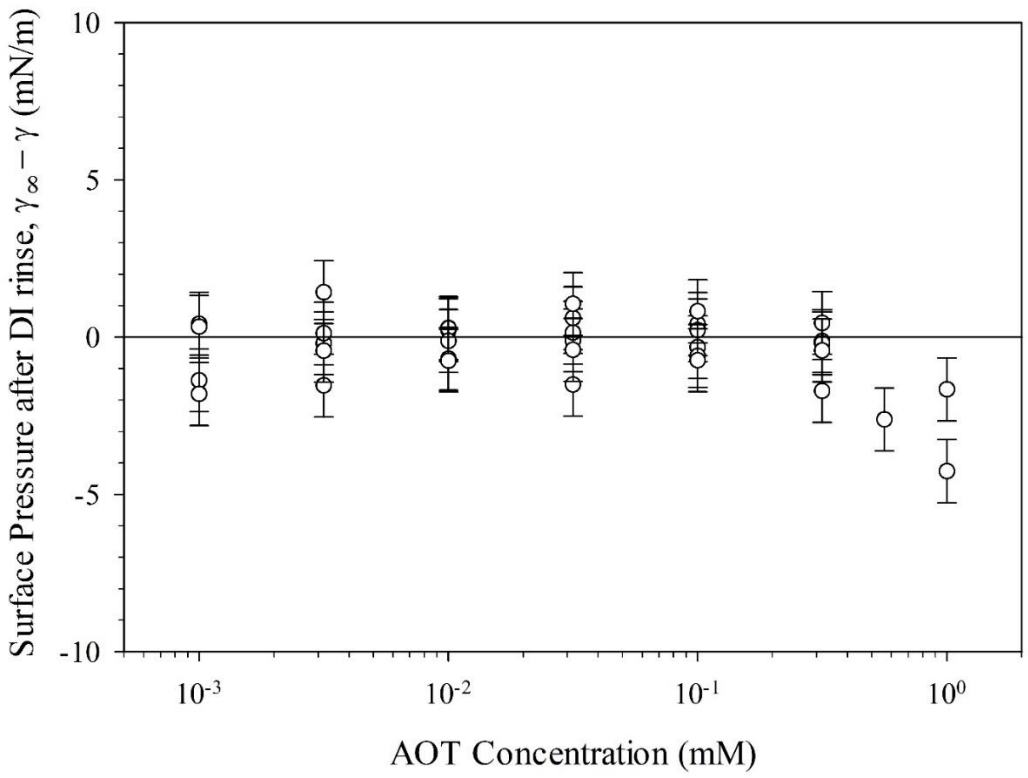

Figure 4.11: Surface pressure of a Tween 80 coated interface after exposure to AOT and a final deionized water rinse as a function of AOT bulk concentration prior to the final rinse.

4.4 DISCUSSION

The irreversible adsorption of Tween 80 to oil/water interfaces has been previously shown to depend on the interfacial tension at the time of rinsing.[7] For low interfacial coverages, Tween 80 adsorption is completely irreversible, and the interfacial tension remains constant upon rinsing. For higher interfacial coverages, however, the interfacial tension increases slightly after rinsing, indicating a small amount of Tween 80 desorption. These observations suggest that Tween 80 interfacial structure depends on interfacial coverage. Recent molecular simulations of Tween 80 at a squalane/aqueous interface show that the conformation of the PEG

headgroup is highly dependent on interfacial coverage.[8] At low coverages, the headgroups bind tightly to the oil/water interface, but at higher coverages, the PEG chains are forced off the interface and into the aqueous phase.

A critical interfacial tension of $\gamma_c \approx 32$ mN/m has been identified as the value below which some partial desorption occurs. The critical value also manifests in increased coalescence times between droplets coated with Tween 80 at interfacial tensions below $\gamma_\infty = 32$ mN/m in deionized water.[29] We do not observe any impact of the critical interfacial tension value on the adsorption of AOT. All tested interfacial tension values of Tween 80, both above and below the critical value (29.1 to 38.9 mN/m), resulted in equivalent decreases in AOT maximum surface concentration, as shown in Figure 4.10.

It should be noted that our ability to convert interfacial tension to interfacial coverage throughout our analysis is based on the assumption that the Gibbs equation can be applied to the surface pressure isotherms shown in Figure 4.2, despite the fact that the system is not at thermodynamic equilibrium after rinsing with deionized water and removing Tween 80 from the bulk solution. However, the maximum surface coverage estimated with this method is similar in value to the maximum surface coverage obtained for Tween 80 interfaces at equilibrium with Tween 80 in solution, before rinsing: $\Gamma_\infty = 1.21 \pm 0.094$ μmol/m^2 for the irreversibly adsorbed component after rinsing, while $\Gamma_\infty = 1.45 \pm 0.13$ μmol/m^2 for adsorbed Tween 80 at equilibrium with the bulk solution before rinsing. We therefore use this estimate to help quantify the interfacial coverage of the irreversibly adsorbed component of Tween 80.

The irreversibly adsorbed material remaining at the squalane/water interface is not chemically or structurally identified in this work. While we have characterized its interfacial behavior, we are unable to determine whether this material is described by the average structure of Tween 80 or some fraction of the inherently polydisperse material. Molecular simulations of various isomers of Tween 80 indicate that the interfacial tension at oil/water interfaces depends on the structure of the Tween 80 molecule.[36] However, simulations also suggest that the average structure of Tween 80 is able to irreversibly adsorb to squalane/water interfaces.[8]

4.5 SUMMARY

We present a study of AOT adsorption on oil/water interfaces pre-coated with Tween 80. We consider the Tween 80 layers to be irreversibly adsorbed after the interface is rinsed with deionized water. A surface pressure for AOT adsorption is defined relative to the initial Tween 80 interfacial tension. AOT adsorbs to the Tween 80 coated interfaces, as observed through increasing surface pressures. Adsorption increases with increasing AOT concentration. AOT adsorption is sensitive to the ionic strength of the solution, with surface pressures and maximum surface coverages increasing in the presence of counterions that screen repulsive electrostatic charges at the interface.

The presence of Tween 80 at the oil/water interface inhibits AOT adsorption. At sufficiently high AOT concentrations, the maximum surface coverage of AOT is independent of the initial Tween 80 coverage for both deionized water and 0.5 M NaCl systems. The values of maximum surface coverage

of AOT on an interface pre-coated with any initial amount of Tween 80 are at least 50% less than the coverage on a clean oil/water interface.

AOT adsorbs reversibly onto the Tween 80 coated interfaces, with surface pressures returning to zero upon rinsing with deionized water. The Tween 80 remains mostly irreversibly adsorbed at the oil/water interface, even after exposure to high concentrations of AOT. The persistence of Tween 80 on the interface is not only relevant to dispersant efficacy, but also impacts the environmental consequences of dispersant use in oil spill remediation.

REFERENCES

(1) Rosen, M. *Surfactants and Interfacial Phenomena*; 3rd Ed.; Wiley-Interscience: New York, 2004.

(2) National Commission on the BP Deepwater Horizon Oil Spill and Offshore Drilling. *Deep Water: The Gulf Oil Disaster and the Future of Offshore Drilling*; Department of Energy: Washington, DC, 2011.

(3) Clayton, J.; Payne, J.; Farlow, J. *Oil Spill Dispersants: Mechanisms of Action and Laboratory Tests*; Lewis Publishers, 1993.

(4) Canevari, G. P. Oil Slick Dispersant and Method. U.S. Patent No. 3,793,218, 1974.

(5) Paris, C. B.; Le, M.; Aman, Z. M.; Subramaniam, A.; Helgers, J.; Wang, D.; Kourafalou, V. H.; Srinivasan, A. Evolution of the Macondo Well Blowout: Simulating the Effects of the Circulation and Synthetic Dispersants on the Subsea Oil Transport. *Environ. Sci. Technol.* **2012**, *46*, 13293–13302.

(6) Riehm, D. A.; McCormick, A. V. The Role of Dispersants' Dynamic Interfacial Tension in Effective Crude Oil Spill Dispersion. *Mar. Pollut. Bull.* **2014**, *84*, 155–163.

(7) Reichert, M. D.; Walker, L. M. Interfacial Tension Dynamics, Interfacial Mechanics, and Response to Rapid Dilution of Bulk Surfactant of a Model Oil-Water-Dispersant System. *Langmuir* **2013**, *29*, 1857–1867.

(8) Huston, K. J.; Larson, R. G. Reversible and Irreversible Adsorption Energetics of Poly(ethylene Glycol) and Sorbitan Poly(ethoxylate) at a Water/Alkane Interface. *Langmuir* **2015**, *31*, 7503–7511.

(9) Svitova, T. F.; Radke, C. J. AOT and Pluronic F68 Coadsorption at Fluid / Fluid Interfaces : A Continuous-Flow Tensiometry Study. *Ind. Eng. Chem. Res* **2005**, *44*, 1129–1138.

(10) Aveyard, R.; Binks, B.; Mead, J. Interfacial Tension Minima in Oil-Water-Surfactant Systems. *J Chem Soc, Faraday Trans 1* **1986**, *82*, 1755–1770.

(11) van Voorst Vader, F. Adsorption of Detergents at the Liquid-Liquid Interface. Part I. *Trans. Faraday Soc.* **1960**, *56*, 1067–1077.

(12) Datwani, S. S.; Stebe, K. J. The Dynamic Adsorption of Charged Amphiphiles: The Evolution of the Surface Concentration, Surface Potential, and Surface Tension. *J. Colloid Interface Sci.* **1999**, *219*, 282–297.

(13) Datwani, S. S.; Stebe, K. J. Surface Tension of an Anionic Surfactant: Equilibrium, Dynamics, and Analysis for Aerosol-OT. *Langmuir* **2001**, *17*, 4287–4296.

(14) Kralchevsky, P. A.; Danov, K. D.; Broze, G.; Mehreteab, A. Thermodynamics of Ionic Surfactant Adsorption with Account for the Counterion Binding: Effect of Salts of Various Valency. *Langmuir* **1999**, *15*, 2351–2365.

(15) Maldonado-Valderrama, J.; Wege, H. A.; Rodriguez-Valverde, M. A.; Galvez-Ruiz, M. J.; Cabrerizo-Vilchez, M. A. Comparative Study of Adsorbed and Spread B-Casein Monolayers at the Water - Air Interface with the Pendant Drop Technique. *Langmuir* **2003**, *19*, 8436–8442.

(16) Miller, R.; Fainerman, V. B.; Makievski, a V; Krägel, J.; Grigoriev, D. O.; Kazakov, V. N.; Sinyachenko, O. V. Dynamics of Protein and Mixed Protein/surfactant Adsorption Layers at the Water/fluid Interface. *Adv. Colloid Interface Sci.* **2000**, *86*, 39–82.

(17) Romoscanu, A. I.; Mezzenga, R. Cross Linking and Rheological Characterization of Adsorbed Protein Layers at the Oil-Water Interface. *Langmuir* **2005**, *21*, 9689–9697.

(18) Thavorn, J.; Hamon, J.; Kitiyanan, B.; Striolo, A.; Grady, B. Competitive Surfactant Adsorption of AOT and TWEEN 20 on Gold Measured Using a Quartz Crystal Microbalance with Dissipation. *Langmuir* **2014**, *30*, 11031–11039.

(19) Svitova, T. F.; Wetherbee, M. J.; Radke, C. J. Dynamics of Surfactant Sorption at the Air/water Interface: Continuous-Flow Tensiometry. *J. Colloid Interface Sci.* **2003**, *261*, 170–179.

(20) Ayorinde, F. O.; Gelain, S. V; Johnson, J. H.; Wan, L. W. Analysis of Some Commercial Polysorbate Formulations Using Matrix-Assisted Laser Desorption/ionization Time-of-Flight Mass Spectrometry. *Rapid Commun. Mass Spectrom.* **2000**, *14*, 2116–2124.

(21) Zhang, R.; Wang, Y. Analysis of Polysorbate 80 and Its Related Compounds by RP-HPLC with ELSD and MS Detection. *J. Chromatogr. Sci.* **2012**, *80*, 1–10.

(22) Luisi, P.; Magid, L. Solubilization of Enzymes and Nucleic Acids in Hydrocarbon Micellar Solution. *Crit. Rev. Biochem. Mol. Biol.* **1986**, *20*, 409–474.

(23) Sager, W. F. C. Systematic Study on the Influence of Impurities on the Phase Behavior of Sodium Bis(2-Ethylhexyl) Sulfosuccinate Microemulsions. *Langmuir* **1998**, *14*, 6385–6395.

(24) Yeom, I.; Ghosh, M.; Cox, C.; Robinson, K. Micellar Solubilization of Polynuclear Aromatic Hydrocarbons in Coal Tar-Contaminated Soils. *Environ. Sci. Technol.* **1995**, *29*, 3015–3021.

(25) Li, Z. X.; Lu, J. R.; Thomas, R. K. Aerosol-OT at the Air / Water Interface : The Surface Excess. *Langmuir* **1997**, *7463*, 3681–3685.

(26) Alvarez, N. J.; Walker, L. M.; Anna, S. L. A Criterion to Assess the Impact of Confined Volumes on Surfactant Transport to Liquid–fluid Interfaces. *Soft Matter* **2012**, *8*, 8917–8925.

(27) Alvarez, N. J.; Walker, L. M.; Anna, S. L. A Microtensiometer to Probe the Effect of Radius of Curvature on Surfactant Transport to a Spherical Interface. *Langmuir* **2010**, *26*, 13310–13319.

(28) Alvarez, N. J. An Experimental and Theoretical Study of Surfactant Dynamics at Microscale Interfaces. Ph.D. Thesis, Carnegie Mellon University, 2011.

(29) Reichert, M. D. Using Microscale Interfaces to Connect Transport Dynamics, Interfacial Mechanics, and Coalescence Behavior for a Model Oil- Dispersant-Aqueous System. Ph.D. Thesis, Carnegie Mellon University, 2013.

(30) Berg, J. C. *An Introduction to Interfaces and Colloids*; 1st Ed.; World Scientific: New Jersey, 2010.

(31) Alvarez, N. J.; Vogus, D. R.; Walker, L. M.; Anna, S. L. Using Bulk Convection in a Microtensiometer to Approach Kinetic-Limited Surfactant Dynamics at Fluid-Fluid Interfaces. *J. Colloid Interface Sci.* **2012**, *372*, 183–191.

(32) Gibbs, J. W. *The Collected Works of J W Gibbs Volume 1*; Longmans, New York, 1928.

(33) Eastoe, J.; Nave, S.; Downer, A.; Paul, A. Adsorption of Ionic Surfactants at the Air-Solution Interface. *Langmuir* **2000**, *16*, 4511–4518.

(34) Kotula, A. P. Dilatational Rheology and Controlled Generation of Microscale Complex Fluid Interfaces. Ph.D. Thesis, Carnegie Mellon University, 2014.

(35) Aveyard, R.; Saleem, S. Interfacial Tensions at Alkane-Aqueous Electrolyte Interfaces. *J. Chem. Soc., Faraday Trans. 1* **1976**, 1609–1617.

(36) Tang, X.; Huston, K. J.; Larson, R. G. Molecular Dynamics Simulations of Structure-Property Relationships of Tween 80 Surfactants in Water and at Interfaces. *J. Phys. Chem. B* **2014**, *118*, 12907–12918.

CHAPTER 5

CHARACTERIZING THE DYNAMIC ADSORPTION BEHAVIOR OF RHAMNOLIPID BIOSURFACTANTS AT AIR/WATER AND OIL/WATER INTERFACES

5.1 INTRODUCTION

Biosurfactants are a structurally diverse group of amphiphilic molecules produced by microorganisms. The molecular structures consist of a hydrophilic portion (typically saccharides, peptides, carboxylate or phosphate groups) and a hydrophobic portion (fatty acids or fatty alcohols).[1] Biosurfactants have been considered as attractive alternatives to conventional surfactants due to their increased biodegradability and lower toxicity for use in environmental remediation, food and consumer products, and pharmaceuticals.[2–4]

Rhamnolipids are glycolipid biosurfactants that consist of one or two rhamnose groups linked to fatty acid chains, as shown in Figure 5.1.[5] Rhamnolipids are produced by the oil-metabolizing bacteria *Pseudomonas aeruginosa*. The biosurfactant acts to increase the hydrophobicity of the cell, enhancing the ability of the bacteria to adhere to oil interfaces for increased oil uptake.[2] There is particular interest in utilizing rhamnolipid biosurfactants in environmental applications, where improved biocompatibility outweighs the high production costs relative to traditional synthetic surfactants.[1,6,7]

Effective use of rhamnolipids as surfactants for any specific application requires knowledge and detailed characterization of their adsorption behavior at air/water and oil/water interfaces. The adsorption of both mono- and di-rhamnolipids at air/water interfaces has been characterized using surface tension

measurements under a variety of environmental conditions. At low concentrations, mono-rhamnolipids have a larger effect on the magnitude of the surface tension than di-rhamnolipids at similar bulk concentrations by about 5 mN/m, likely due to more efficient packing of the smaller molecule at the surface.[8,9] Mixtures of mono- and di-rhamnolipids produce an intermediary effect on the surface tension that depends on the ratio of mono- to di-rhamnolipid.[10–12] Rhamnolipids are negatively charged at neutral pH due to the carboxyl groups adjoining the alkane chains; decreasing the pH or increasing the ionic strength decreases the CMC and surface tension due to reduced electrostatic repulsion between molecules.[13–15]

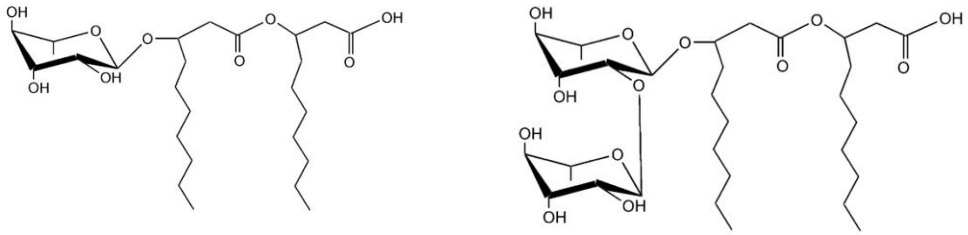

Figure 5.1: Characteristic mono- and di-rhamnolipids produced by *P. aeruginosa*.

While there has been substantial characterization of equilibrium rhamnolipid adsorption at air/water interfaces, we have found no reports of their adsorption dynamics at the air/water interface. Further, rhamnolipid adsorption at oil/water interfaces has been studied to a much lesser degree, despite significant interest in their potential use in oil/water systems. Özdemir *et al.*[14] report the equilibrium values of interfacial tension of rhamnolipids at decane/water and hexadecane/water interfaces, but most previous studies that consider oil/water systems simply characterize the bulk emulsification ability of rhamnolipids through turbidity measurements or emulsion layer heights.[5,16]

A commercial mixture of mono- and di-rhamnolipids has recently been made available. In this study, we use surface and interfacial tension measurements to characterize the dynamics of adsorption of rhamnolipids at a spherical air/water and squalane/water interface. Adsorption reversibility at both interfaces is assessed through bulk solution exchange with deionized water. Finally, the interaction of rhamnolipids with an irreversibly-adsorbed nonionic surfactant is characterized using a sequential adsorption procedure. This chapter provides insight into the adsorption mechanisms governing rhamnolipid adsorption at both air/water and oil/water interfaces.

5.2 MATERIALS AND METHODS

A mixture of mono- and di-rhamnolipids is purchased from Sigma-Aldrich (St. Louis, MO) at 95% purity and used as received. The ratio of di- to mono-rhamnolipids is between 3:2 and 4:1 as reported by the manufacturer, corresponding to an estimated average molecular weight of 606 g/mol. A stock solution is prepared at a concentration of 42 mg/L (69 μM) in deionized water from a Barnstead Ultrapure water purification system to 18.2 MΩ·cm resistivity. The measured pH of the unbuffered stock solution in deionized water is 6.9, indicating the rhamnolipids are negatively charged in solution.[14] Dilutions used for interfacial measurements are made volumetrically in acid washed glass vials that have been pre-rinsed with rhamnolipid solution to minimize depletion to the container walls.[17] Tween 80 is purchased from Sigma (St. Louis, MO) and is used without further purification.

All rhamnolipid solutions are stored at 35 ^{o}C to ensure full solubility in solution. The stock rhamnolipid solution is unstable at room temperature (21 ± 1 ^{o}C); after several hours at room temperature, crystals begin to appear in solution. The Krafft temperature of micellar solutions of mono-rhamnolipids is 31.8 ^{o}C and of di-rhamnolipids is 21.3 ^{o}C.[18] We expect the mixture used in this study to have a similar Krafft temperature. All interfacial measurements presented here are made at room temperature despite this concern to compare with previous studies in the literature. No crystallization is observed in the dilute solutions during the timescale of the experiments, which typically last for 1000 seconds or less. The surface tension of select concentrations of rhamnolipid was measured at 35 ^{o}C to identify any effect of temperature on interfacial measurements; equivalent equilibrium values of surface tension were obtained for all tested concentrations.

Squalane ($C_{30}H_{62}$) is used as the oil phase, purchased from Sigma (St. Louis, MO) at 98% purity. The oil is filtered by gravity in a column packed with 1.5g of basic activated alumina. The oil is considered clean if the interfacial tension against pure deionized water remains constant at γ = 52.5 ± 1 mN/m for at least 1000 seconds.

A microtensiometer is used to measure the dynamic interfacial tension of the air/water and oil/water interface. The platform is described in detail in Chapter 3 and elsewhere.[19–21] Briefly, the microtensiometer consists of a capillary filled with air or oil in line with a pressure transducer. The capillary is placed in a 3-D printed thermoplastic cell, submerged in an aqueous solution reservoir, and imaged on a Nikon T-300 inverted light microscope. The air or oil forms a spherical cap at

the tip of the capillary. The radius of the cap is measured along with the pressure jump across the interface to determine the instantaneous surface tension, $\gamma(t)$, using the Laplace equation.

Capillaries are purchased from World Precision Instruments, Inc. (Sarasota, FL) with dimensions of i.d.=0.75mm, o.d.=1mm, and L=150mm, and are pulled to a tip radius of 35-42μm using custom settings on a PMP-100 capillary puller (Micro Data Instrument Inc., South Plainfield, NJ). The interiors of the capillaries are acid washed and coated with hydrophobic Dynasylan® SIVOCLEAR (Evonik Industries, Essen, Germany) as described in Chapter 3 to ensure the three phase contact line remains pinned at the tip of the capillary.

Exchange of the bulk aqueous solution is achieved by flowing solution through the sample reservoir via two ports connected to a peristaltic pump. Flow is maintained for a minimum of 200 s to ensure complete replacement of the reservoir solution (the residence time of the 3 mL reservoir is about 10 s). Flow rates are chosen to maintain a local Reynolds number $Re < 3$ and capillary number $Ca < 1x10^{-4}$, so that there is no interfacial deformation due to flow.

5.3 RESULTS

5.3.1 Adsorption at Air/Water and Oil/Water Interfaces

Rhamnolipid adsorption at an air/water interface is characterized with dynamic surface tension measurements. Figure 5.2 shows surface tension as a function of time for seven different concentrations of rhamnolipid. The surface tension begins at a clean value of 72.8 ± 0.5 mN/m, and decreases as rhamnolipid

adsorbs to the interface. The bubble radius decreases throughout the adsorption while the pressure is held constant. The radius varies from 40 to 52 μm across all experiments in Figure 5.2, decreasing by an average of 2 μm during each individual run (corresponding to less than a 5% change). The equilibrium surface tension decreases with increasing rhamnolipid concentration, as does the time required to reach equilibrium. The equilibrium surface tension values fall between the expected pure mono- and di- rhamnolipid values reported by Özdemir *et al.*[13] at neutral pH, suggesting a mixture of both mono- and di- rhamnolipids present at the interface.

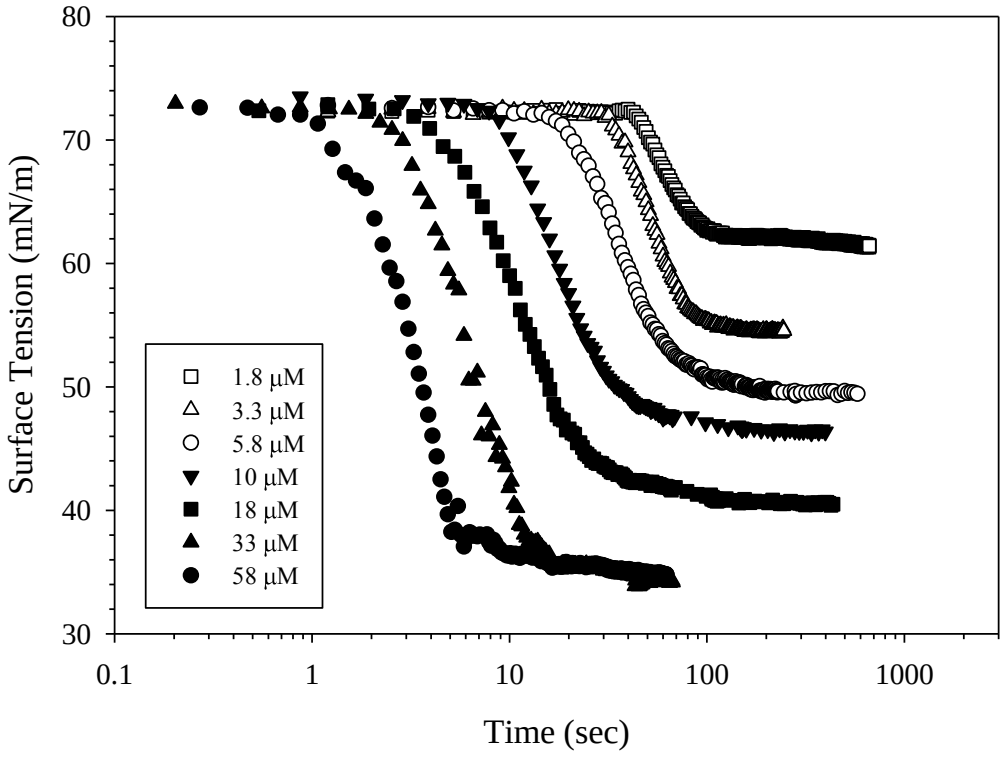

Figure 5.2: Surface tension as a function of time during the adsorption of rhamnolipid to an air/water interface. The bubble radius for each concentration is between 40 and 52 μm, decreasing by an average of 2 μm during adsorption (<5% change).

Increasing the concentration beyond 33 μM does not correspond to a further change in surface tension, indicating the CMC of the rhamnolipid mixture has been reached. This agrees with prior surface tension measurements of pure mono- and di- rhamnolipids, which identify the CMC values to be between 40 and 70 μM, respectively, in deionized water.[8] Equilibrium is reached in less than 1000 seconds for all concentrations.

Figure 5.3 shows the interfacial tension as a function of time for the adsorption of seven different concentrations of rhamnolipid to a squalane/water interface. As at air/water interfaces, increasing the bulk rhamnolipid concentration decreases both the equilibrium interfacial tension and the time required to reach equilibrium. The range of bulk concentrations in Figure 5.3 is lower than those in Figure 5.2, yet corresponds to similar changes in the magnitude of the interfacial tension. The drop radius varies from 56 to 120 μm across all concentrations at the oil/water interface, with an average decrease of 17 μm during adsorption (corresponding to an 18% change). Larger initial radii are needed to accommodate the entire range of interfacial tension values achieved by the rhamnolipids at an oil/water interface.

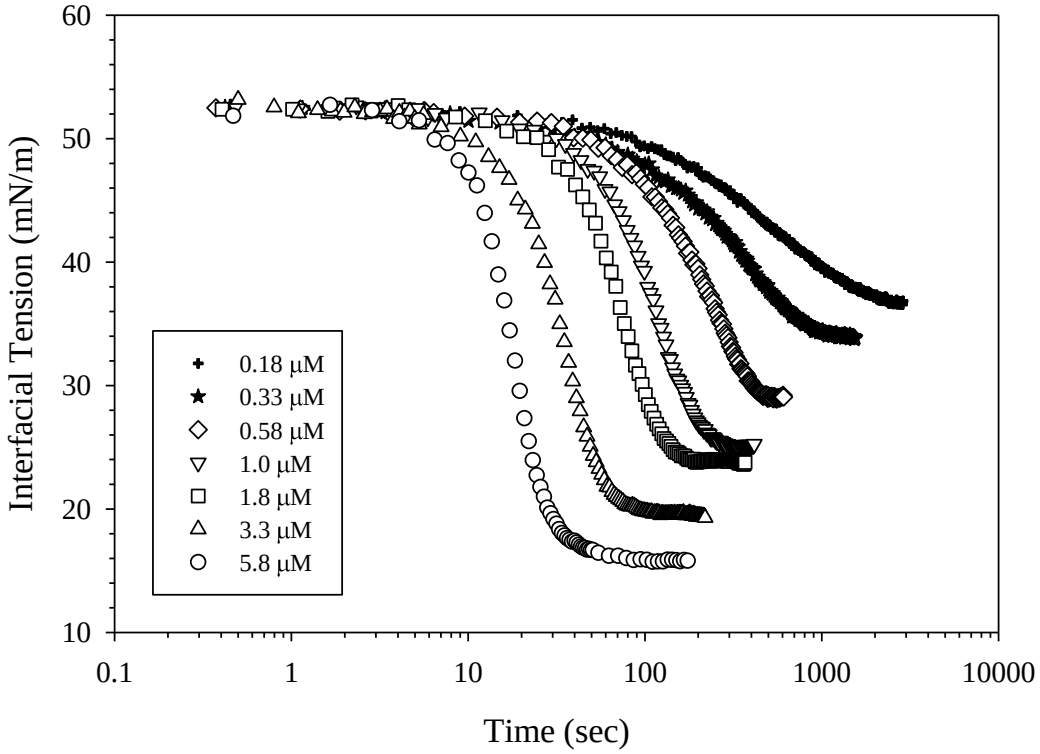

Figure 5.3: Interfacial tension as a function of time during the adsorption of rhamnolipid to a squalane/water interface. The drop radius across all experiments is between 56 and 120 μm, with an average decrease of 17 μm during each adsorption (<18% change).

To directly compare the adsorption of rhamnolipid at air/water and oil/water interfaces, the equilibrium surface pressure is plotted as a function of concentration in Figure 5.4, where surface pressure is defined as $\Pi = \gamma - \gamma_0$. A clean air/water interface has a measured surface tension of γ_0 = 72.8 ± 0.5 mN/m and a clean oil/water interface has a measured interfacial tension of γ_0 = 52.5 ± 0.5 mN/m. For a given concentration of rhamnolipid, the surface pressure at the oil/water interface is 15 – 20 mN/m larger than at the air/water interface.

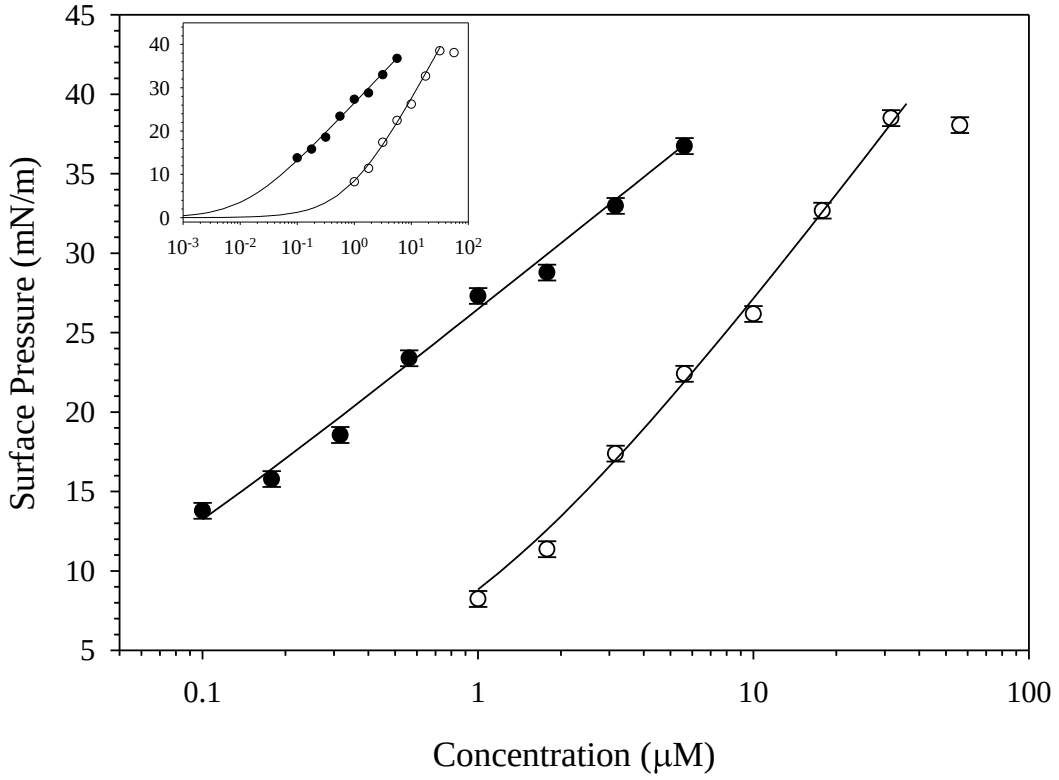

Figure 5.4: Surface pressure isotherms of rhamnolipid adsorption at air/water (○) and squalane/water (●) interfaces. Lines are best fit to equation (5.1) using values of Γ_∞ obtained from equation (5.2). Inset shows an extrapolation of the Langmuir fit to $\Pi = 0$.

The surface pressure at each interface can be modeled by the Langmuir isotherm,

$$\Pi = -nRT\Gamma_\infty \ln\left(\frac{a}{C+a}\right), \tag{5.1}$$

where R is the gas constant, T is the temperature, Γ_∞ is the maximum surface concentration, C is the bulk rhamnolipid concentration and a is the ratio of the desorption rate constant, α, to the adsorption rate constant, β, such that $a = \alpha/\beta$. The integer n accounts for counterion adsorption, and has a value of n = 2 for negatively charged rhamnolipid at neutral pH.[22] Equation (5.1) has two unknown parameters, a and Γ_∞. It is possible to determine Γ_∞ directly using the Gibbs equation for charged species,[23]

$$\Gamma_{\infty} = \frac{1}{nRT}\frac{d\Pi}{d\ln C}. \qquad (5.2)$$

Equation (5.2) is applied to the high concentration data in Figure 5.4, where the slope of the surface pressure data approaches a constant value. By calculating Γ_{∞} from equation (5.2), the only freely adjustable parameter in equation (5.1) is *a*. The best-fit values of Γ_{∞} and *a* are shown in Table 5.1 for rhamnolipid adsorption at an air/water and oil/water interface. The isotherm model is plotted for each interface in Figure 5.4 as a solid line. The Figure 5.4 inset extrapolates the Langmuir isotherm to show concentrations that would give a value of surface pressure equal to zero.

Table 5.1: Langmuir model fit parameters for rhamnolipid adsorption

	Γ_{∞} (μmol/m^2)	*a* (μmol/m^3)
Air/water	2.06 ± 0.04	743
Squalane/water	1.22 ± 0.07	13

The maximum surface concentrations obtained from equation (5.2) are similar to values previously reported for mixtures of mono- and di-rhamnolipid at air/water[8,12] and hexadecane/water[14] interfaces. The value of the maximum surface concentration at air/water interfaces is larger than at oil/water, suggesting more efficient rhamnolipid packing at air/water interfaces at concentrations approaching the CMC.

To characterize the transport of rhamnolipid to the air/water and oil/water interface, we use the results of fitting the Langmuir isotherm model to convert the dynamic surface tension and interfacial tension data in Figures 5.2 and 5.3 to surface concentration, Γ. This analysis assumes the surface tension is solely a

function of surface concentration and provides an estimate of surface coverage as a function of time without requiring additional fitted parameters. Figure 5.5 shows the dimensionless surface coverage, ϕ, at air/water and oil/water interfaces as a function of time, where $\phi = \Gamma(t) / \Gamma_{eq}$. Only concentrations below the CMC are included. Each concentration begins with a clean interface ($\Gamma = 0$) and reaches an equilibrium coverage ($\Gamma = \Gamma_{eq}$). As observed in Figures 5.2 and 5.3, increasing the bulk rhamnolipid concentration increases the rate at which equilibrium coverage is obtained. By scaling the dynamic curves in Figure 5.5, the differences in the shape of the curves is more obvious. At air/water interfaces, the shape of the surface coverage curve with time is constant across all concentrations, and simply shifts horizontally to shorter times as the bulk concentration is increased. At oil/water interfaces, however, the shape of the curves evolves with concentration. Surface coverage increases at a slower overall rate at low concentrations than at high concentrations, seen in the changing slope of the curves in Figure 5.5(b).

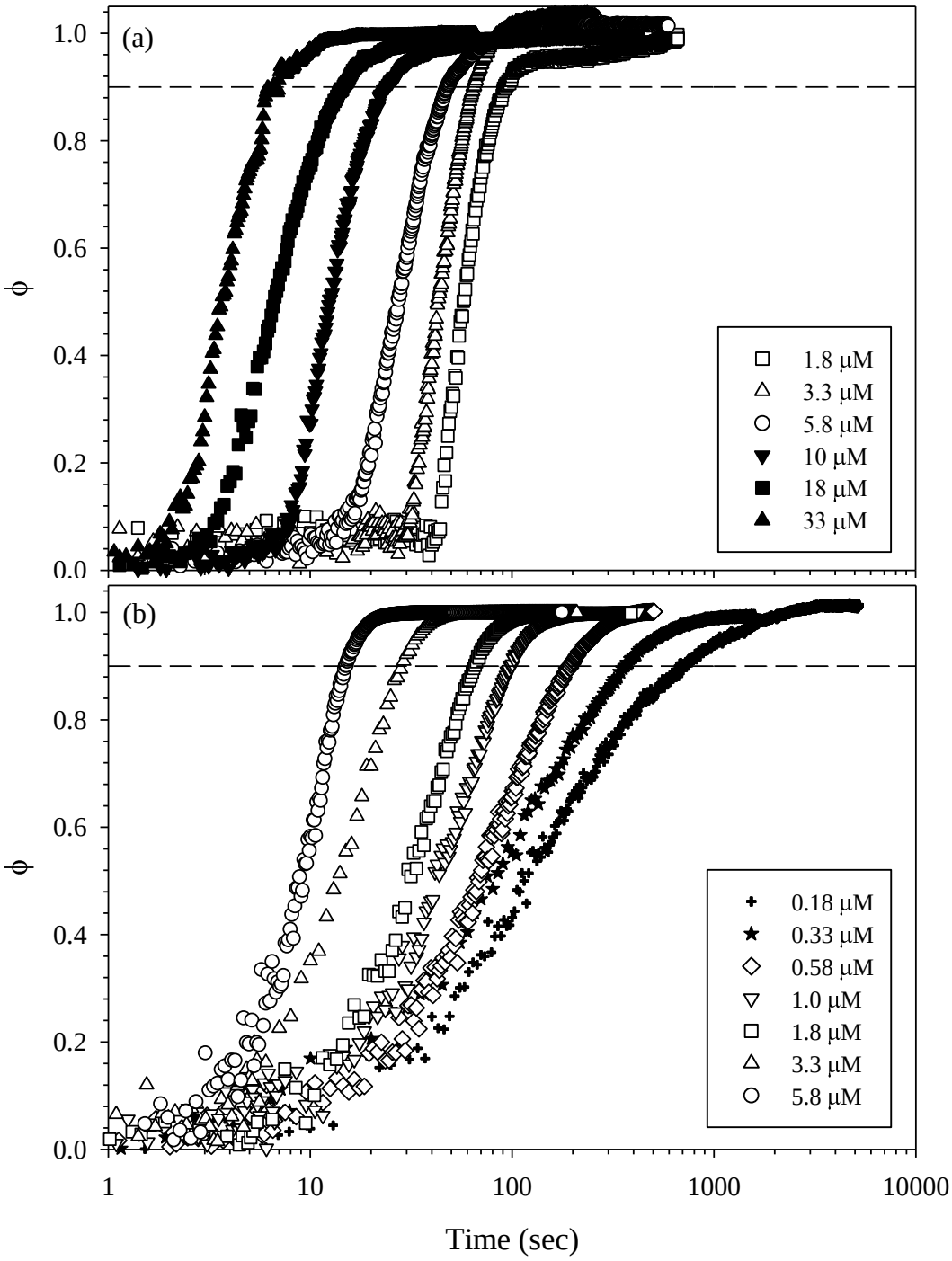

Figure 5.5: Surface coverage as a function of time at an (a) air/water and (b) squalane/water interface. Data from Figures 5.2 and 5.3 is converted to surface coverage assuming the Langmuir isotherm model. Dashed line indicates a fractional coverage of $\phi = 0.9$.

To compare characteristic timescales of adsorption for each concentration, an experimental adsorption timescale is defined as the time required to achieve a surface coverage $\phi = 0.9$ (indicated by the dashed line). The timescale values are reported in Table 5.2.

Table 5.2: Experimental adsorption timescales at air/water and oil/water interfaces as a function of bulk rhamnolipid concentration

Concentration (μM)	$\tau_{,a/w}$ (s)	$\tau_{,o/w}$ (s)
0.18	--	686
0.33	--	360
0.58	--	194
1.0	--	97.5
1.8	111	65.5
3.3	64.3	29.0
5.8	46.8	15.0
10	23.2	--
18	13.7	--
33	6.0	--

To determine the dominant transport mechanism for each rhamnolipid concentration, we use a scaling analysis developed by Alvarez *et al.*[19,20] to compare the experimental adsorption timescale to the characteristic timescale for diffusion to a spherical interface. Surfactant adsorption is commonly assumed to occur via two primary mechanisms: diffusion to the interface and kinetic exchange at the interface. If the adsorption is diffusion-limited, the timescale for adsorption depends on the interfacial curvature. As the interfacial radius decreases, the ratio of the surface area of the bubble to the volume surrounding the bubble also decreases. This effectively increases the availability of molecules for adsorption to a spherical interface compared to a planar interface, and reduces the timescale for diffusion.

The characteristic timescale for diffusion to an interface is defined as $\tau_D = l^2 / D$, where l is a length scale across which diffusion must occur and D is the diffusion coefficient. For a planar interface, $\tau_{D,p} = h_p^2 / D$, where h_p is the planar diffusion depth, $h_p = \Gamma_{eq} / C$. Γ_{eq} is the equilibrium surface coverage, and C is the bulk surfactant concentration. Alvarez *et al.*[19,20] identified the timescale for diffusion to a spherical interface as

$$\tau_{D,s} = \frac{\left(h_s^3 h_p\right)^{1/2}}{D}, \tag{5.3}$$

where $h_s = R\left[\left(3\frac{h_p}{R}+1\right)^{1/3} - 1\right]$ and R is the radius of the interface. Using this definition, experimental adsorption timescales to a spherical bubble or drop can be compared to the characteristic diffusion timescales to determine the primary adsorption mechanism. If the experimental values agree with the diffusion timescales, the dynamics are assumed to be diffusion limited.[21]

Figure 5.6 shows the experimental timescales from Table 5.2, normalized by the planar diffusion timescale $\tau_{D,p} = h_p^2 / D$ and plotted as a function of dimensionless drop radius R / h_p. Although the radius of the interface decreases throughout each adsorption experiment, the total change corresponds to less than a 5% difference at air/water interfaces and less than 18% at oil/water interfaces. The value of R is taken as the average radius throughout the adsorption to scale the data in Figure 5.6. The planar diffusion depth h_p is calculated using the Langmuir isotherm to estimate Γ_{eq} for each concentration. The diffusion coefficient is

estimated with a correlation by Wilke and Chang[24] for the diffusion of an organic molecule in dilute aqueous solution as $D = 3.75 \times 10^{-10}\ m^2/s$.

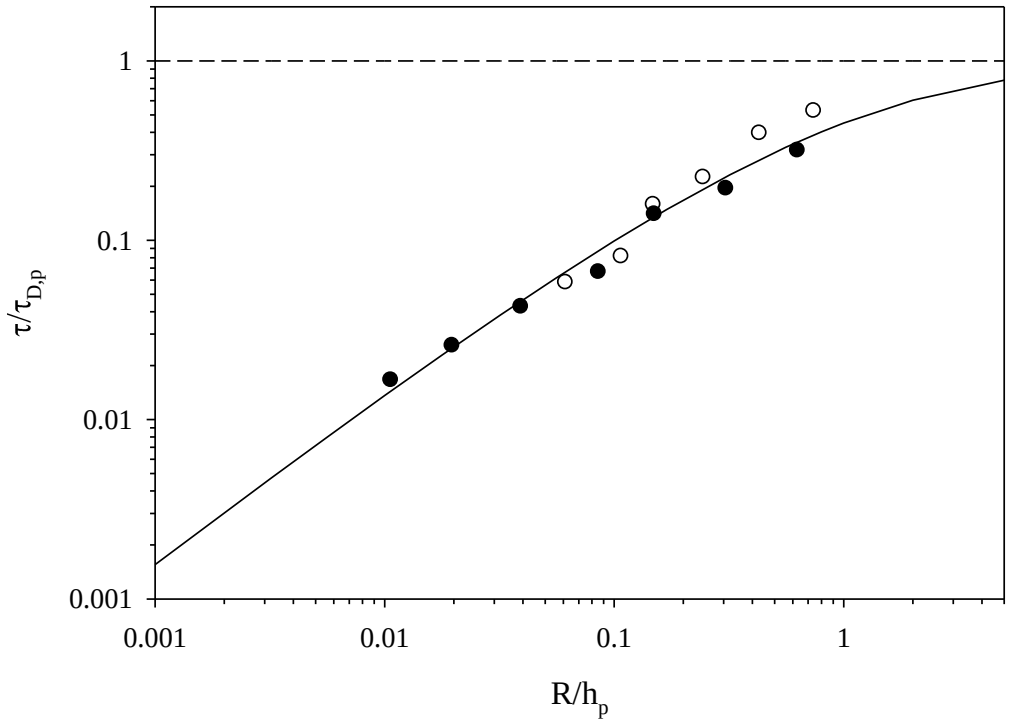

Figure 5.6: Scaled experimental timescales for rhamnolipid adsorption to an air/water (○) and oil/water (●) interface. Solid line is the diffusion timescale for a spherical interface normalized by the planar diffusion timescale, dashed line is the normalized timescale for diffusion to a planar interface.

The solid line in Figure 5.6 is the dimensionless timescale for diffusion to a spherical interface, $\tau_{D,s} / \tau_{D,p}$. The oil/water adsorption timescale data shows good agreement with the spherical diffusion timescale, indicating the adsorption is diffusion limited for all concentrations. The highest air/water concentrations deviate slightly from the spherical diffusion curve, possibly indicating a transition from diffusion-limited adsorption to a regime where adsorption kinetics are relevant.[21]

If the dynamic data presented in Figures 5.2 and 5.3 is diffusion limited, we can estimate a lower bound on β, the kinetic adsorption rate constant, by comparing the diffusion timescale, τ_D, to the kinetic timescale, τ_K. The kinetic timescale is obtained by solving the Langmuir kinetic equation for adsorption to an interface,[23]

$$\frac{\partial \Gamma}{\partial t} = \beta C \Gamma_\infty \left(1 - \frac{\Gamma}{\Gamma_\infty}\right) - \alpha \Gamma, \tag{5.4}$$

where α and β are the desorption and adsorption rate constants, respectively. From equation (5.4), a kinetic timescale is identified as

$$\tau_K = \frac{1}{\beta C + \alpha}. \tag{5.5}$$

The minimum value of β that yields $\tau_D > \tau_K$ provides the lower bound on β for diffusion-limited adsorption. Using the experimental timescales in Table 5.2 as τ_D and the values of the isotherm parameter $a = \alpha / \beta$ from Table 5.1, we obtain $\beta \geq 5.2$ m^3/mol/s for rhamnolipid adsorption at air/water interfaces and $\beta \geq 12$ m^3/mol/s for adsorption at oil/water interfaces. The values are the same order of magnitude as values of β obtained for C_iE_j surfactants at air/water and oil/water interfaces estimated using the same scaling analysis,[21,25] which have molecular weights similar to rhamnolipids.

Figure 5.6 also highlights the strong effect of curvature on adsorption time for diffusion-limited systems. For the lowest values of R / h_p (low rhamnolipid concentrations), the diffusive timescale for adsorption to a spherical interface is almost two orders of magnitude lower than the timescale for adsorption to a planar interface. In the case of 1.8 μM rhamnolipid, for example, we achieve $\phi = 0.9$ in

less than 700 seconds for adsorption to an interface with R = 59 μm. The same concentration would require over 19 hours to reach equivalent coverage at a planar interface.

Additional characterization of rhamnolipid adsorption at air/water and oil/water interfaces is performed by assessing adsorption reversibility. After a solution of rhamnolipid has been allowed to adsorb to the interface, the surfactant solution is exchanged with deionized water using the method described in Chapter 4. Figure 5.7 shows the surface pressure before and after rinse for air/water and oil/water interfaces exposed to various concentrations of rhamnolipid solution. In all experiments, the value of the surface pressure after rinsing is greater than zero, but less than the surface pressure before rinsing, indicating partially irreversible adsorption. The surface pressure after rinsing is always larger at oil/water interfaces than at air/water interfaces, and is nearly independent of the initial surface pressure.

The difference in reversibility is also reflected in the values of *a* in Table 5.1, where *a* is the ratio of the desorption rate constant to the adsorption rate constant. The value of *a* for rhamnolipid adsorption at air/water interfaces is an order of magnitude greater than at oil/water interfaces, suggesting a much slower desorption rate at oil/water interfaces that corresponds to the higher surface pressure observed after rinsing. We estimate a timescale for desorption at each interface as $\tau_{des} = 1/\alpha$, where α is obtained using the minimum values of β calculated above and the values of the isotherm parameter *a* in Table 5.1. For rhamnolipid adsorbed at an air/water interface, the value of the desorption timescale is τ_{des} ~ 260 seconds; at an oil/water interface, the value increases to τ_{des} ~ 6400 s.

Rinsing is carried out for about 500 seconds to ensure complete replacement of the surfactant solution with deionized water, but the estimate of the desorption timescale suggests that 500 seconds may be insufficient for full rhamnolipid desorption from an oil/water interface.

We attribute the slight increase in irreversibility at oil/water interfaces to greater rhamnolipid partitioning into the oil phase. To test the solubility of rhamnolipid in squalane, a small volume of oil was exposed to a concentrated rhamnolipid solution for 24 hours. The oil was then exposed to clean deionized water and the surface pressure was measured. After two hours, the surface pressure reached a value of 4 mN/m, which is above the 1 mN/m cutoff required for a "clean" squalane/water interface, suggesting minimal rhamnolipid solubility in the oil phase.

We note that the analysis presented in Figures 5.4 – 5.6 was developed for small-molecule surfactants, whose adsorption is fully reversible. We have applied it to the rhamnolipid system here to show that even for larger, more complicated structures, timescales can be used to characterize the dynamics of surfactant adsorption.

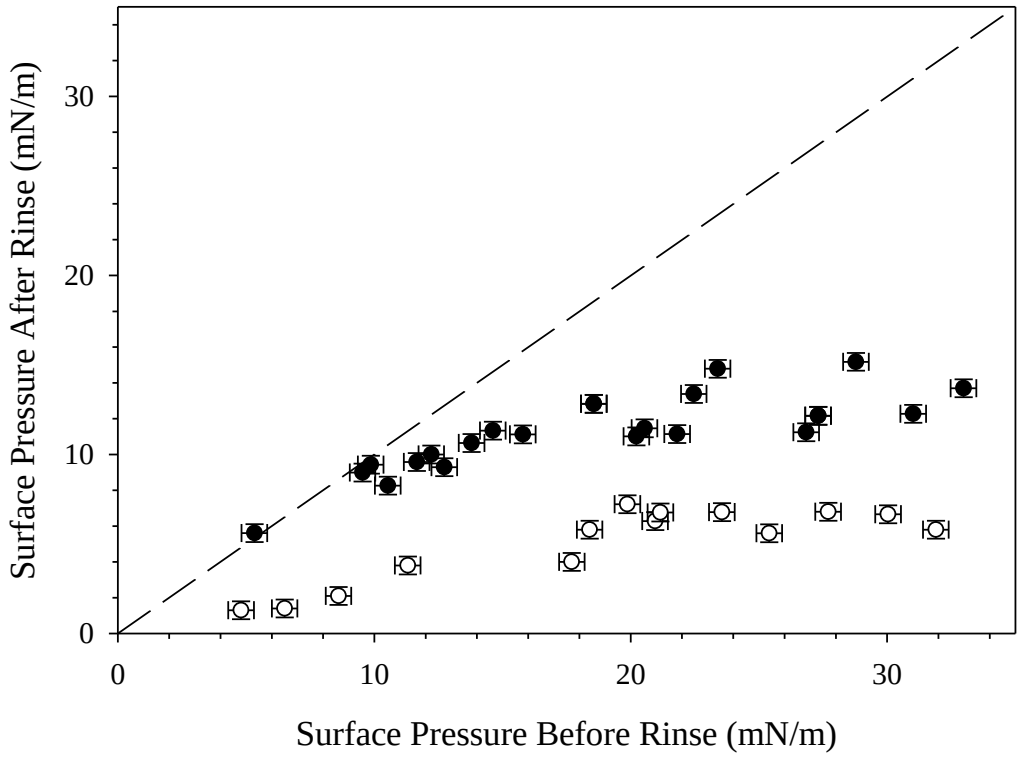

Figure 5.7: Surface pressure before and after bulk rhamnolipid solution is exchanged with deionized water for air/water (○) and oil/water (●) interfaces. Dashed line is a one to one line indicating completely irreversible adsorption.

5.3.2 Sequential Adsorption with Tween 80

The co-adsorption of rhamnolipid with synthetic surfactants is of interest in a variety of applications where multiple surface-active species are present. In the case of oil spill dispersants, there is interest in understanding the interaction of rhamnolipid with Tween 80, a nonionic surfactant that has been shown to adsorb irreversibly at oil/water interfaces.[26] Using a sequential adsorption procedure described previously[27] and in Chapter 4, we assess the adsorption of rhamnolipid at an oil/water interface pre-coated with various amounts of Tween 80. Figure 5.8 shows the surface pressure as a function of rhamnolipid concentration for the

adsorption of rhamnolipid on Tween 80-coated squalane/water interfaces. A modified surface pressure is defined as $\Pi = \gamma_\infty - \gamma$, where γ_∞ is the surface tension of the irreversibly adsorbed component of Tween 80. The modified surface pressure corresponds to the rhamnolipid contribution to the overall measured surface pressure. For all Tween 80 coverages, the surface pressure increases with rhamnolipid concentration, indicating the rhamnolipid is able to co-adsorb on the pre-coated interfaces.

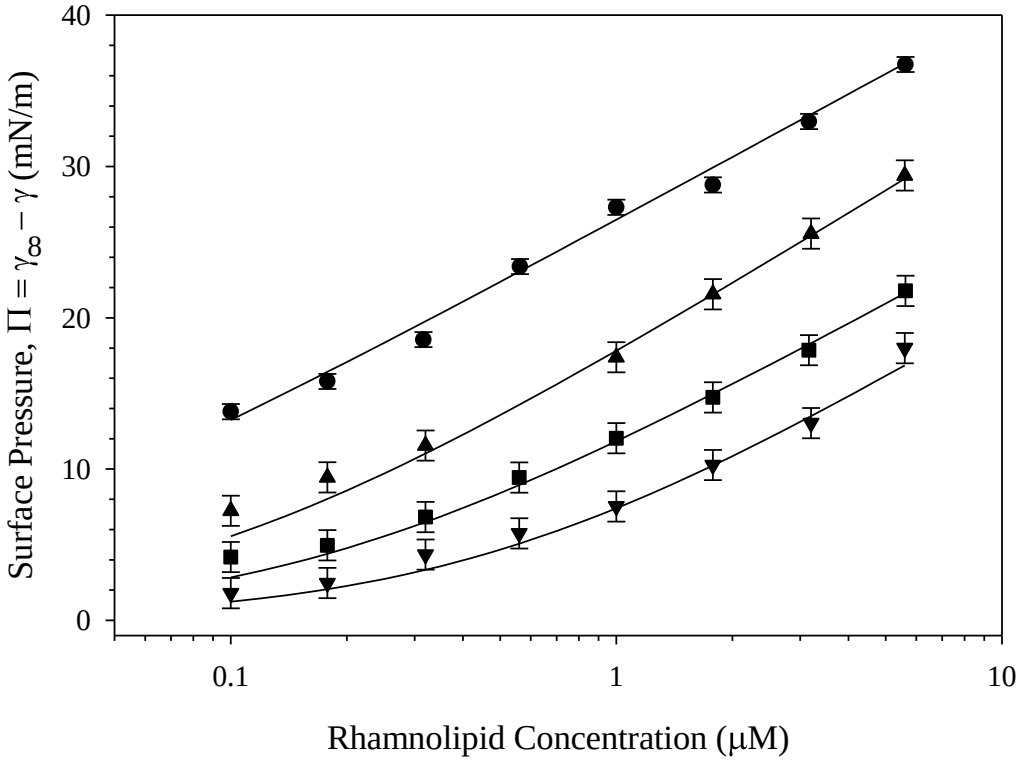

Figure 5.8: Surface pressure as a function of rhamnolipid concentration at a clean squalane/water interface (●) and squalane/water interfaces pre-coated with Tween 80: γ_∞ = 43.4 ± 0.9 mN/m (▲), γ_∞ = 36.5 ± 0.7 mN/m (■), and γ_∞ = 30.9 ± 0.7 mN/m (▼). Lines are best fits of equation 5.2 to each data set.

The Langmuir isotherm model is fit to the data in Figure 5.8 for each Tween 80-coated interface. Table 5.3 shows the parameters from the best fit to equation

5.2. Surprisingly, the maximum surface concentration is roughly constant, independent of Tween 80 initial coverage, indicating rhamnolipid adsorption at high concentrations is not inhibited by the presence of Tween on the interface. This contrasts with the result obtained for the co-adsorption of AOT, a simple anionic surfactant, on interfaces pre-coated with Tween 80 in Chapter 4. The value of *a* increases with increasing Tween 80, suggesting a change in the kinetic adsorption constants that depends on Tween 80 coverage.

Table 5.3: Langmuir model fit parameters for rhamnolipid adsorption at oil/water interfaces pre-coated with Tween 80

	Γ_∞ (μmol/m^2)	a (μmol/m^3)
Clean squalane/water	1.23 ± 0.07	12.5
Tween 80 γ_∞ = 43.4 mN/m	1.40 ± 0.06	80
Tween 80 γ_∞ = 36.5 mN/m	1.25 ± 0.16	170
Tween 80 γ_∞ = 30.9 mN/m	1.37 ± 0.48	500

Adsorption reversibility of the rhamnolipid is assessed using the same rinsing procedure described above. Figure 5.9 shows the surface pressure after bulk solution exchange with deionized water for each Tween 80 coverage. The value of the modified surface pressure after rinsing is greater than zero for all Tween coated interfaces, indicating some irreversibly adsorbed material remains adsorbed despite rinsing. From interfacial tension data alone we cannot determine the relative composition of rhamnolipid and Tween 80 on the interface, but hypothesize that the initially adsorbed Tween 80 remains unaffected by rhamnolipid adsorption, and any elevated surface pressure in Figure 5.9 is due to the presence of some irreversibly adsorbed rhamnolipid after rinsing. If this is the case, the rinsed surface pressure in the presence of Tween is not as high as for pure rhamnolipid adsorption

on a clean oil/water interface. For a given rhamnolipid concentration, the value of the surface pressure after rinsing decreases with increasing initial Tween 80 coverage. At the highest Tween 80 coverage, rhamnolipid adsorption appears to be fully reversible across most tested concentrations. The increase in adsorption reversibility as a function of Tween 80 coverage is also reflected in the values of the isotherm parameter *a*. Increasing Tween 80 coverage results in an increase in *a*, corresponding to an increase in the rate of desorption relative to that of adsorption.

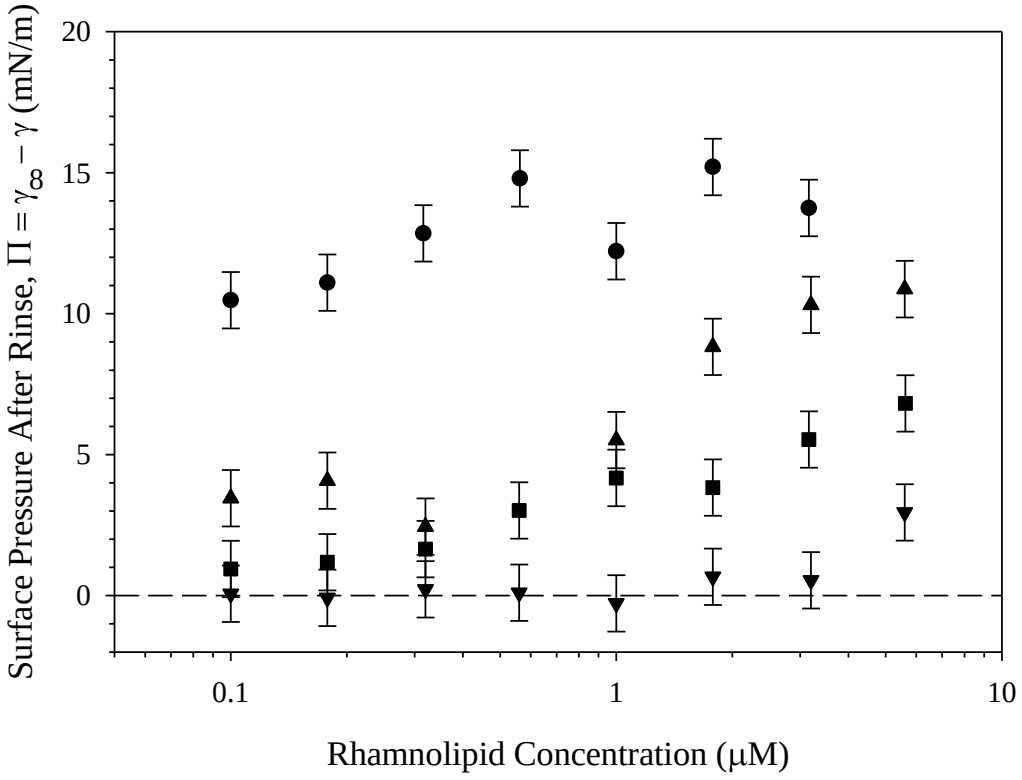

Figure 5.9: Surface pressure after bulk solution exchange with deionized water as a function of bulk rhamnolipid concentration before rinsing for a clean squalane/water interface (●) and for different initial Tween 80 coated interfaces, where γ_∞ = 43.4 ± 0.9 mN/m (▲), γ_∞ = 36.5 ± 0.7 mN/m (■), and γ_∞ = 30.9 ± 0.7 mN/m (▼).

5.4 SUMMARY

We have characterized the dynamic and equilibrium adsorption of mono- and di-rhamnolipid biosurfactants at spherical air/water and oil/water interfaces. The adsorption is modeled using the Langmuir isotherm to quantify the surface coverage as a function of bulk concentration. Although rhamnolipid has a larger effect on the surface pressure of oil/water interfaces than that of air/water interfaces at low concentrations, the maximum surface coverage of rhamnolipid is larger at air/water interfaces. Using a timescale analysis for adsorption to spherical interfaces, the adsorption of rhamnolipids appears to be diffusion-limited for the concentrations considered here. The adsorption of rhamnolipid is partially irreversible at both oil/water and air/water interfaces and is roughly independent of the surface pressure before rinsing.

Rhamnolipid adsorbs to oil/water interfaces that have been pre-coated with the nonionic surfactant Tween 80, forming mixed interfaces. The maximum surface concentration of rhamnolipid is unaffected by Tween 80 coverage, indicating that adsorption at high concentrations is not suppressed by the presence of a secondary surfactant. When the mixed interfaces are rinsed, the surface pressure does not always return to a value of zero, indicating that some combination of Tween 80 and rhamnolipid surfactant remains on the surface. The persistence of rhamnolipid at interfaces both alone and in the presence of a secondary surfactant highlights the complex nature of their adsorption.

REFERENCES

(1) Lang, S.; Wullbrandt, D. Rhamnose Lipids--Biosynthesis, Microbial Production and Application Potential. *Appl. Microbiol. Biotechnol.* **1999**, *51*, 22–32.

(2) Mulligan, C. N. Environmental Applications for Biosurfactants. *Environ. Pollut.* **2005**, *133*, 183–198.

(3) Desai, J. D.; Banat, I. M. Microbial Production of Surfactants and Their Commercial Potential. *Microbiol. Mol. Biol. Rev.* **1997**, *61*, 47–64.

(4) Churchill, S. A.; Griffin, R. A.; Jones, L. .; Chirchill, P. . Biodegradation Rate Enhancement of Hydrocarbons by an Oleophilic Fertilizer and a Rhamnolipid Biosurfactant. *J. Environ. Qual.* **1995**, *24*, 19–28.

(5) Lang, S. Biological Amphiphiles (Microbial Biosurfactants). *Curr. Opin. Colloid Interface Sci.* **2002**, *7*, 12–20.

(6) Urum, K.; Pekdemir, T. Evaluation of Biosurfactants for Crude Oil Contaminated Soil Washing. *Chemosphere* **2004**, *57*, 1139–1150.

(7) Zhang, Y.; Miller, R. M. Enhanced Octadecane Dispersion and Biodegradation by a Pseudomonas Rhamnolipid Surfactant (Biosurfactant). *Appl. Environ. Microbiol.* **1992**, *58*, 3276–3282.

(8) Chen, M. L.; Penfold, J.; Thomas, R. K.; Smyth, T. J. P.; Perfumo, a.; Marchant, R.; Banat, I. M.; Stevenson, P.; Parry, a.; Tucker, I.; et al. Solution Self-Assembly and Adsorption at the Air-Water Interface of the Monorhamnose and Dirhamnose Rhamnolipids and Their Mixtures. *Langmuir* **2010**, *26*, 18281–18292.

(9) Zhong, H.; Zeng, G. M.; Liu, J. X.; Xu, X. M.; Yuan, X. Z.; Fu, H. Y.; Huang, G. H.; Liu, Z. F.; Ding, Y. Adsorption of Monorhamnolipid and Dirhamnolipid on Two Pseudomonas Aeruginosa Strains and the Effect on Cell Surface Hydrophobicity. *Appl. Microbiol. Biotechnol.* **2008**, *79*, 671–677.

(10) Peker, S.; Helvaci, Ş.; Özdemir, G. Interface-Subphase Interactions of Rhamnolipids in Aqueous Rhamnose Solutions. *Langmuir* **2003**, *19*, 5838–5845.

(11) Abalos, A.; Pinazo, A.; Infante, M. R.; Casals, M.; García, F.; Manresa, A. Physicochemical and Antimicrobial Properties of New Rhamnolipids Produced by Pseudomonas Aeruginosa AT10 from Soybean Oil Refinery Wastes. *Langmuir* **2001**, *17*, 1367–1371.

(12) İkizler, B.; Arslan, G.; Kipcak, E.; Dirik, C.; Çelenk, D.; Aktuğlu, T.; Helvacı, Ş. Ş.; Peker, S. Surface Adsorption and Spontaneous Aggregation of Rhamnolipid Mixtures in Aqueous Solutions. *Colloids Surfaces A Physicochem. Eng. Asp.* **2016**.

(13) Helvaci, S. S.; Peker, S.; Özdemir, G. Effect of Electrolytes on the Surface Behavior of Rhamnolipids R1 and R2. *Colloids Surfaces B Biointerfaces* **2004**, *35*, 225–233.

(14) Özdemir, G.; Peker, S.; Helvaci, S. S. Effect of pH on the Surface Behavior of Rhamnolipids R1 and R2. *Colloids Surfaces A* **2004**, *35*, 135–143.

(15) Abbasi, H.; Noghabi, K. A.; Hamedi, M. M.; Zahiri, H. S.; Moosavi-Movahedi, A. A.; Amanlou, M.; Teruel, J. a.; Ortiz, A. Physicochemical Characterization of a Monorhamnolipid Secreted by Pseudomonas Aeruginosa MA01 in Aqueous Media. An Experimental and Molecular Dynamics Study. *Colloids Surfaces B Biointerfaces* **2013**, *101*, 256–265.

(16) Lovaglio, R. B.; dos Santos, F. J.; Jafelicci, M.; Contiero, J. Rhamnolipid Emulsifying Activity and Emulsion Stability: PH Rules. *Colloids Surfaces B Biointerfaces* **2011**, *85*, 301–305.

(17) Alvarez, N. J.; Walker, L. M.; Anna, S. L. A Criterion to Assess the Impact of Confined Volumes on Surfactant Transport to Liquid–fluid Interfaces. *Soft Matter* **2012**, *8*, 8917–8925.

(18) Ishigami, Y.; Gama, Y.; Nagahora, H.; Yamaguchi, M.; Nakahara, H.; Kamata, T. The pH-Sensitive Conversion of Molecular Aggregates of Rhamnolipid Biosurfactant. *Chemistry Letters*, 1987, 763–766.

(19) Alvarez, N. J.; Walker, L. M.; Anna, S. L. A Microtensiometer to Probe the Effect of Radius of Curvature on Surfactant Transport to a Spherical Interface. *Langmuir* **2010**, *26*, 13310–13319.

(20) Alvarez, N.; Walker, L.; Anna, S. Diffusion-Limited Adsorption to a Spherical Geometry: The Impact of Curvature and Competitive Time Scales. *Phys. Rev. E* **2010**, *82*, 11604.

(21) Alvarez, N. J.; Lee, W.; Walker, L. M.; Anna, S. L. The Effect of Alkane Tail Length of CiE8 Surfactants on Transport to the Silicone Oil-Water Interface. *J. Colloid Interface Sci.* **2011**, *355*, 231–236.

(22) Eastoe, J.; Nave, S.; Downer, A.; Paul, A. Adsorption of Ionic Surfactants at the Air-Solution Interface. *Langmuir* **2000**, *16*, 4511–4518.

(23) Rosen, M. J. *Surfactants and Interfacial Phenomena*; 3rd Editio.; Wiley-Interscience: New York, 2004.

(24) Wilke, C. .; Chang, P. Correlation of Diffusion Coefficients in Dilute Solutions. *AIChE J.* **1955**, 264–270.

(25) Alvarez, N. J.; Vogus, D. R.; Walker, L. M.; Anna, S. L. Using Bulk Convection in a Microtensiometer to Approach Kinetic-Limited Surfactant Dynamics at Fluid-Fluid Interfaces. *J. Colloid Interface Sci.* **2012**, *372*, 183–191.

(26) Reichert, M. D.; Walker, L. M. Interfacial Tension Dynamics, Interfacial

Mechanics, and Response to Rapid Dilution of Bulk Surfactant of a Model Oil-Water-Dispersant System. *Langmuir* **2013**, *29*, 1857–1867.

(27) Kirby, S. M.; Anna, S. L.; Walker, L. M. Sequential Adsorption of an Irreversibly Adsorbed Nonionic Surfactant and an Anionic Surfactant at an Oil/Aqueous Interface. *Langmuir* **2015**, *31*, 4063–4071.

CHAPTER 6

FORMATION OF A RIGID HYDROPHOBIN FILM AND DISRUPTION BY AN ANIONIC SURFACTANT AT AN AIR/WATER INTERFACE*

6.1 INTRODUCTION

Hydrophobins are a family of small, surface-active proteins produced by filamentous fungi. All hydrophobins share a similar rigid, globular structure stabilized by a network of disulfide bonds between cysteine residues in the amino acid sequence.[1] The location of polar and nonpolar amino acids relative to these bonds gives rise to an amphiphilic macromolecule that readily adsorbs to surfaces and interfaces and exhibits unique surface properties.[2–5] Hydrophobins form strong membranes at the air/water interface, with shear elasticities that are reported to be an order of magnitude larger than other proteins.[6] The elastic surface membrane allows hydrophobins in solution to stabilize non-equilibrium bubble shapes that resist bubble shrinkage and wrinkle upon compression.[7–9] Unlike many other commonly studied proteins, hydrophobins do not easily denature in solution or at interfaces, instead adsorbing as rigid structures that do not undergo large conformational changes.[10]

Observation of the unusual interfacial behavior of hydrophobins has led to interest in their potential industrial applications, particularly in surface coatings, food foams and emulsions, and as dispersants.[4,11,12] Substantial work has been done to characterize the surface properties of one hydrophobin in particular, HFBII from

* Reproduced in part with permission from *Langmuir* (DOI:10.1021/acs.langmuir.6b00809). Copyright 2016 American Chemical Society.

the fungus *Trichoderma reesei*, but its adsorption behavior can vary widely across measurement techniques. Using neutron reflectivity, Zhang *et al.*[13] observed that HFBII adsorbs as a monolayer, and that the adsorbed surface concentration of HFBII is approximately constant at 0.39×10^{-6} mol/m^2, independent of bulk concentration. Stanimirova *et al.*[14] obtained a similar surface concentration measured with ellipsometry, but through AFM measurements found that HFBII adsorption is patchy, with regions of monolayer, trilayer, and void space.

Protein adsorption is also probed through surface tension measurements, which are sensitive even to small amounts of adsorbed species. However, the formation of a rigid hydrophobin film at the surface can complicate surface tension measurements. Cox *et al.*[8] measured surface tension using a Wilhelmy plate, but observed that the plate becomes "locked" in position at high HFBII concentrations. Alexandrov *et al.*[15] used a pendant drop tensiometer to measure surface tension, but the solidification of the surface film at high concentrations no longer allowed the bubble to be fit by the Laplace equation. Similar issues arise when the HFBII surface is compressed to obtain a measure of surface elasticity. Depending on the instrument and technique used, the modulus has been observed to increase monotonically with surface pressure,[14] or exhibit a maximum over a range of surface pressures.[15–18] The modulus can also depend on the rate of compression; pausing during the compression allows the hydrophobin to relax on the surface, changing the measured surface tension and elasticity.[14,15] The nature of the protein film formed likely depends on the formation method, and the variation in reported

measurements highlights the importance of controlling for measurement technique when reporting values of surface tension or elasticity.

In addition to understanding HFBII adsorption as a single species, there is interest in understanding how hydrophobin adsorption is altered in the presence of surfactants or other proteins, as multiple surface-active species are often present in industrial formulations.[19] The presence of high concentrations of surfactant often limits protein adsorption, due to the formation of protein-surfactant complexes in bulk.[20,21] Zhang *et al.*[13] observed the phenomenon for HFBII in the presence of three surfactants: $C_{12}E_6$, CTAB, and SDS, where HFBII adsorption is reduced to zero at surfactant concentrations near the CMC of the surfactant. Similar behavior is observed for protein-protein systems; the introduction of secondary proteins such as β-casein or β-lactoglobulin results in co-adsorption of the proteins and synergistic effects on the surface rheology.[6,22]

To investigate surfactant-hydrophobin interaction at an interface, the formation of complexes in the bulk phase must be avoided. One method to achieve this is to employ a sequential adsorption technique, exposing the air/water interface to solutions with only one species present in the bulk at a time. This approach has been used to characterize the behavior of multiple surfactants at an interface,[23–25] and can easily be applied to protein-surfactant systems. Stanimirova *et al.*[16] compared parallel and sequential adsorption of HFBII with SDS, observing that SDS dominates the interface during parallel adsorption, but pre-coating the interface with HFBII prevents its displacement by SDS. Due to the complicated nature of measuring the interfacial properties of a rigid film, no sequential

adsorption studies have been performed on hydrophobin films that have fully solidified before exposure to surfactants.

Cerato-ulmin (CU) is a hydrophobin produced by *Ophiostoma ulmi* that exhibits strong surface activity.[26] While the crystal structure of CU is unknown, we expect it to have similar features to HFBII due to the similarities in amino acid sequence length and location of the structure-defining disulfide bonds.[2,27] Russo *et al.*[26,28] observed similar surface behavior for CU, including the formation of strong surface films and non-spherical bubbles in solution; however, detailed investigations into the mechanics of the CU films have not been performed.

The work presented here characterizes CU adsorption at an air/water interface using surface tension and dilatational rheology measurements performed on a microtensiometer, a platform based on a capillary tensiometer. We investigate CU adsorption from bulk solution and assess its reversibility by exchanging the bulk solution with deionized water. Using a previously developed sequential adsorption methodology,[23] we assess the impact of a secondary surfactant, SDS, on the surface pressure and dilatational modulus of CU surface films.

6.2 MATERIALS AND METHODS

Cerato-ulmin is a gift of Wayne Richards of the Canadian Forest Service. It is produced by a strain of *C. ulmi* (RDT2) and purified according to the methods of Takai and Richards[29] and Stevenson *et al.*[30] Sample dryness is maintained by storing at ambient temperature and pressure inside a sealed vial, held in a screw-top jar containing Drierite® ($CaSO_4$) and sealed with Parafilm®. A stock solution of

0.02 mg/mL CU is prepared by dispersing the hydrophobin in deionized water. CU sample solutions (0.002 mg/mL) are diluted volumetrically from the concentrated stock solution in acid-washed glass vials. Vials are pre-rinsed with dilute solution to minimize depletion from the bulk solution via adsorption to glass walls. The sample solution is placed in a sonication bath immediately prior to use to eliminate any microscopic bubbles stabilized by CU.[26] Sodium dodecyl sulfate (SDS) is purchased from Fisher Scientific (Waltham, MA) and used without further purification. Deionized water is supplied by a Barnstead Ultrapure water purification system to 18.2 MΩ·cm resistivity.

A microtensiometer is used to measure the surface tension and dilatational modulus of the air/water interfaces. The device is described in detail in Chapter 3 and elsewhere,[31–34] and consists of a pressure transducer in line with a capillary filled with air and held at a constant pressure by a pressure head. The capillary is held in a 3-D printed thermoplastic cell, submerged in an aqueous solution reservoir and imaged on an inverted light microscope. The air in the capillary forms a spherical cap at the tip of the capillary, and the radius is measured in real time with the pressure jump across the curved interface to determine the instantaneous surface tension from the Laplace equation for a spherical cap,

$$\gamma(t) = \frac{(P_1(t) - P_2)R(t)}{2}, \tag{6.1}$$

where P_1 is the pressure of the air inside the capillary, P_2 is the hydrostatic pressure of the aqueous solution at the capillary, and R is the measured radius of the interface. A fresh interface is produced at the beginning of each experiment by ejecting a slug of air from the capillary tip. The air is ejected by temporarily

increasing the pressure head behind the capillary using a solenoid valve. The uncertainty in the calculated interfacial tension is $\Delta\gamma = \pm 0.5$ mN/m due to the propagation of random errors in the pressure and radius measurements.

The capillaries are purchased from World Precision Instruments, Inc. (Sarasota, FL) with dimensions of ID = 0.75mm, OD = 1 mm, L = 150 mm. The capillaries are pulled to a tip radius of 35-38 μm using custom settings on a PMP-100 capillary puller (micro Data Instrument Inc, South Plainfield, NJ). The interior of the capillaries is acid washed and coated with the hydrophobic coating arylalkoxy silane XIAMETER® OFS-6124 from Dow Corning (Midland, MI) according to manufacturer instructions. The hydrophobic coating ensures that the air/water interface is pinned at the tip of the capillary for the duration of the experiment.

Exchange of the bulk solution is achieved via two reservoir ports connected to a peristaltic pump, as described in Chapter 3. To ensure complete fluid exchange, flow is maintained for a minimum of 10 residence times (at least 100 seconds). The flow rates and bubble sizes used in this study yield a local Reynolds number $Re = \rho UR/\mu < 3$ and capillary number $Ca = \mu U/\gamma < 1 \times 10^{-4}$, where ρ is the density of the bulk fluid, U is the linear fluid velocity past the interface (measured with particle tracking), R is the radius of the interface, and μ is the viscosity of the bulk fluid. These values of *Re* and *Ca* indicate that interfacial deformation due to induced flow should not be expected.

The dilatational modulus of the interface is measured by imposing a low-amplitude pressure oscillation and measuring the oscillatory response of the radius of the interface. The dilatational modulus E is defined as,

$$E = \frac{dP^S}{d\ln A} \ , \tag{6.2}$$

the derivative of the surface excess normal stress, P^S, with respect to the surface area of the interface, A. The interface forms a spherical cap at the tip of the capillary in the microtensiometer, and the surface area is calculated from the radius of the interface by $A = 2\pi R\left(R - \sqrt{R^2 - R_C^2}\right)$, where R_c is the radius of the capillary. The magnitude of the dilatational modulus can be written in terms of the measured pressure and radius,[35]

$$|E^*| = \frac{b_1}{1-b_1}\left(\frac{R_{eq}}{\Delta R_1}\right)\left(\frac{P_a R_{eq}}{2}\right)\sqrt{\left(\frac{\Delta R_1}{R_{eq}}\right)^2 + 2\left(\frac{\Delta R_1}{R_{eq}}\right)\cos\phi_{R1} + 1} \quad , \tag{6.3}$$

where $b_1 = \sqrt{1-\left(\frac{R_c}{R_{eq}}\right)^2}$ and $\Delta R_1 = R_a\left(\frac{P_{eq}}{P_a}\right)$. P_{eq} is the equilibrium pressure, R_{eq} is the equilibrium radius of the interface, P_a is the amplitude of the pressure oscillations, R_a is the amplitude of the radial oscillations, and ϕ_{R1} is the phase angle of the radial oscillations. All oscillations reported here are performed at a frequency of 1.9 rad/sec, which is in the frequency-independent range for CU adsorption. The data is analyzed using a fast Fourier transform in MATLAB® to find the primary frequency, amplitude and phase angle of the pressure and radius oscillations. The amplitude of any higher harmonics present in the data must be less than 10% of the amplitude of the primary harmonic for the small amplitude assumption to be valid.

Equation (6.3) is then applied to extract |E*|, the magnitude of the dilatational modulus, which we will refer to as the dilatational modulus. The uncertainty in the dilatational modulus is due to the propagation of random errors in the pressure and radius measurements.

The Gibbs modulus E_G is defined as,

$$E_G = \frac{d\gamma}{d\ln A} = -\frac{d\Pi}{d\ln A}, \tag{6.4}$$

where Π is the surface pressure, or the difference between the surface tension of the clean air/water surface and the instantaneous measured surface tension. The Gibbs modulus is measured by decreasing the pressure behind the interface with a syringe pump (BS-8000, Braintree Scientific, Inc) at a constant rate of 11 Pa/s. Decreasing the pressure corresponds to a decrease in the surface area of the spherical cap. The areal compression rate is not constant due to the spherical cap geometry, but has an average value of 1000 μm^2/min. The Gibbs modulus is calculated from a slope based on a linear fit of surface tension versus the natural log of the surface area. Reported error in the Gibbs modulus is based error propagation from the measured pressure jump and radius.

6.3 RESULTS

6.3.1 Cerato-ulmin Adsorption

The dynamics of adsorption of Cerato-ulmin to an air/water interface from bulk solution are characterized by measuring the surface pressure and dilatational modulus of the interface as a function of time. Figure 6.1(a) shows the surface pressure versus time for three subsequent adsorption experiments of a dilute 0.002

mg/mL CU solution to an air/water interface, where the instantaneous surface pressure is defined as $\Pi = \gamma_0 - \gamma$, the difference between the surface tension of the clean air/water surface (γ_0 = 72.8 ± 0.5 mN/m) and the instantaneous measured surface tension of the CU solution, γ. The surface pressure increases with time as CU adsorbs to the surface. At 200 to 300 second intervals, the pressure inside the bubble is oscillated to measure the dilatational modulus. The oscillations correspond to the vertical "bars" in Figure 6.1(a). The time range for the final oscillation is expanded in the figure inset to show the measured sinusoidal oscillations in the surface pressure. The small amplitude oscillations do not affect the dynamic surface tension over time. The dilatational modulus for each of the oscillatory measurements is calculated using equation (6.3), and is shown in Figure 6.1(b) as a function of time for each experiment. The dilatational measurements made over time were not made on an equilibrium interface, but serve as a probe of the interfacial mechanics.

The three experiments shown in Figure 6.1 were made on the same dilute sample of CU, taken sequentially. The first experiment began immediately after the sample was loaded into the microtensiometer reservoir (○), the second experiment began 1500 seconds after loading (▽), and the third began 3000 seconds after loading (■). The differences in the dynamics between experiments is likely a consequence of the extremely dilute hydrophobin concentration used. Once the hydrophobin solution is placed in the reservoir of the microtensiometer, the CU adsorbs not only to the air/water interface at the capillary, but also simultaneously adsorbs to the reservoir walls and to the free air/water surface of the reservoir.

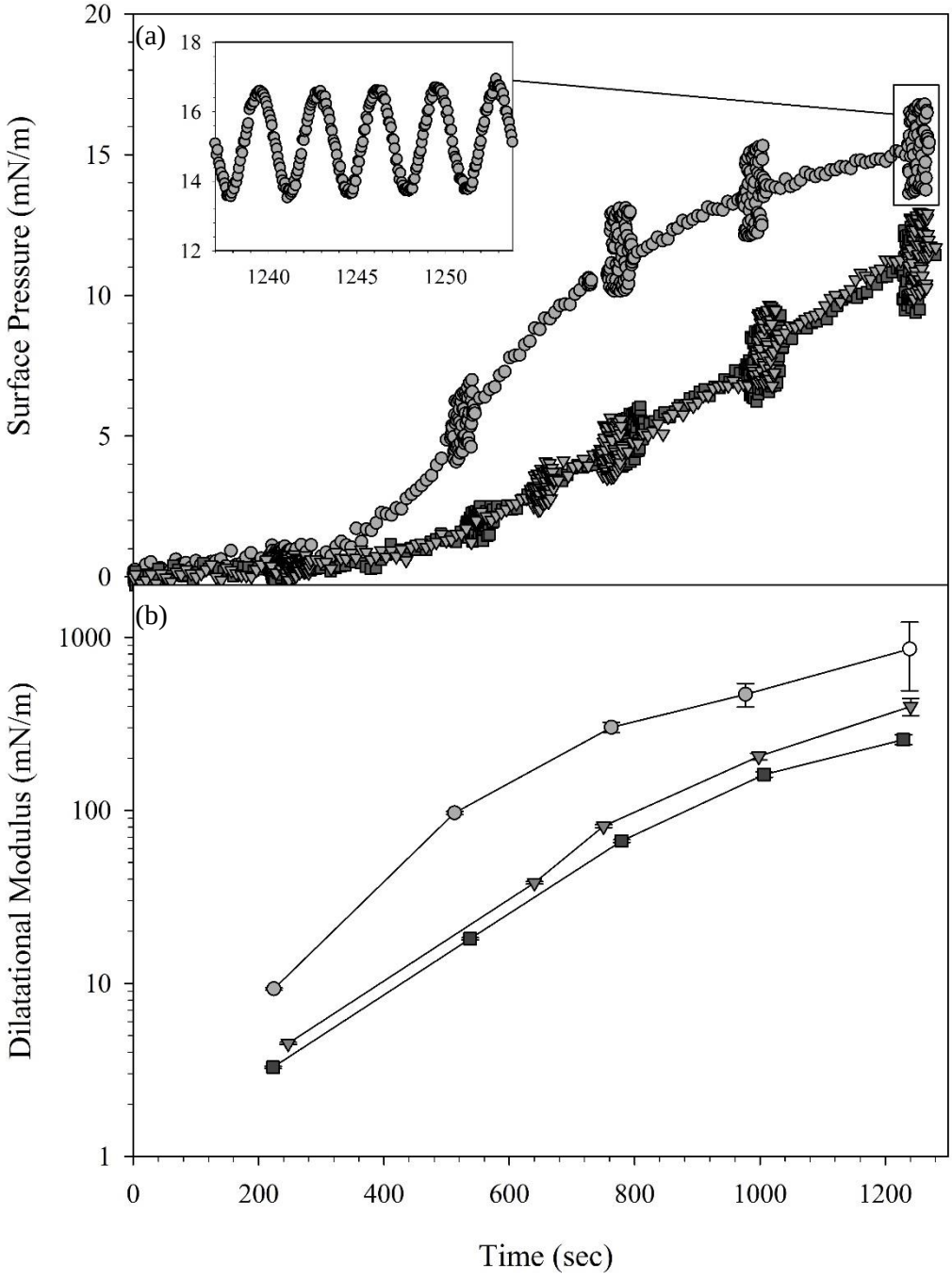

Figure 6.1: (a) Dynamic surface pressure and (b) dilatational modulus as a function of time for three sequential adsorption experiments of a 0.002 mg/mL solution of Cerato-ulmin at an air/water interface: immediately after pouring the sample into the reservoir (○), a reservoir residence time of 1500 seconds (▽), and a residence time of 3000 seconds (■). Vertical "bars" in (a) indicate pressure oscillations to measure the dilatational modulus shown in (b). The inset shows the oscillations in surface pressure resulting from the imposed pressure oscillations. Lines are added in (b) to guide the eye.

Assuming CU adsorption to the free air/water surface and reservoir walls approaches the maximum surface concentrations for HFBII at each surface (0.39 μmol/m^2 for an air/water interface,[13] 0.17 μmol/m^2 for a Teflon surface,[36] and 0.6 μmol/m^2 for a glass surface[37]), the bulk solution concentration of CU can potentially be depleted by up to 50%. Because surface pressure measurements are extremely sensitive to bulk concentration, especially in dilute solutions,[32] the reduction of CU in the bulk solution results in slower adsorption dynamics the longer the solution resides in the reservoir. In Figure 6.1, the surface pressure and dilatational modulus increase at much slower rates during the second and third measurements, after the CU has had sufficient time to adsorb to the walls and free surface. Once the adsorption to the walls and free surface is complete, the dynamics become reproducible across multiple runs.

At long surface ages, the mechanics of the interface show one of the interesting features of CU adsorption. In the first experiment, as shown in Figure 6.1 (●), the dilatational modulus increases until the magnitude becomes too large to measure. This occurs when the modulus is so large that the imposed pressure oscillations do not result in measurable oscillations in the bubble radius. The change in magnitude of the radial oscillations as the modulus increases is shown in Figure 6.2. The data in Figure 6.2(a) is obtained 18 seconds after a clean interface is exposed to the CU solution, and the data in Figure 6.2(b) is obtained after 1008 seconds. The amplitude of the pressure oscillation P_a = 90 Pa is the same in both Figure 6.2(a) and (b); however, the amplitude of the radial response decreases substantially, from R_a = 1.2 μm in Figure 6.2(a) to R_a < 0.1 μm in Figure 6.2(b).

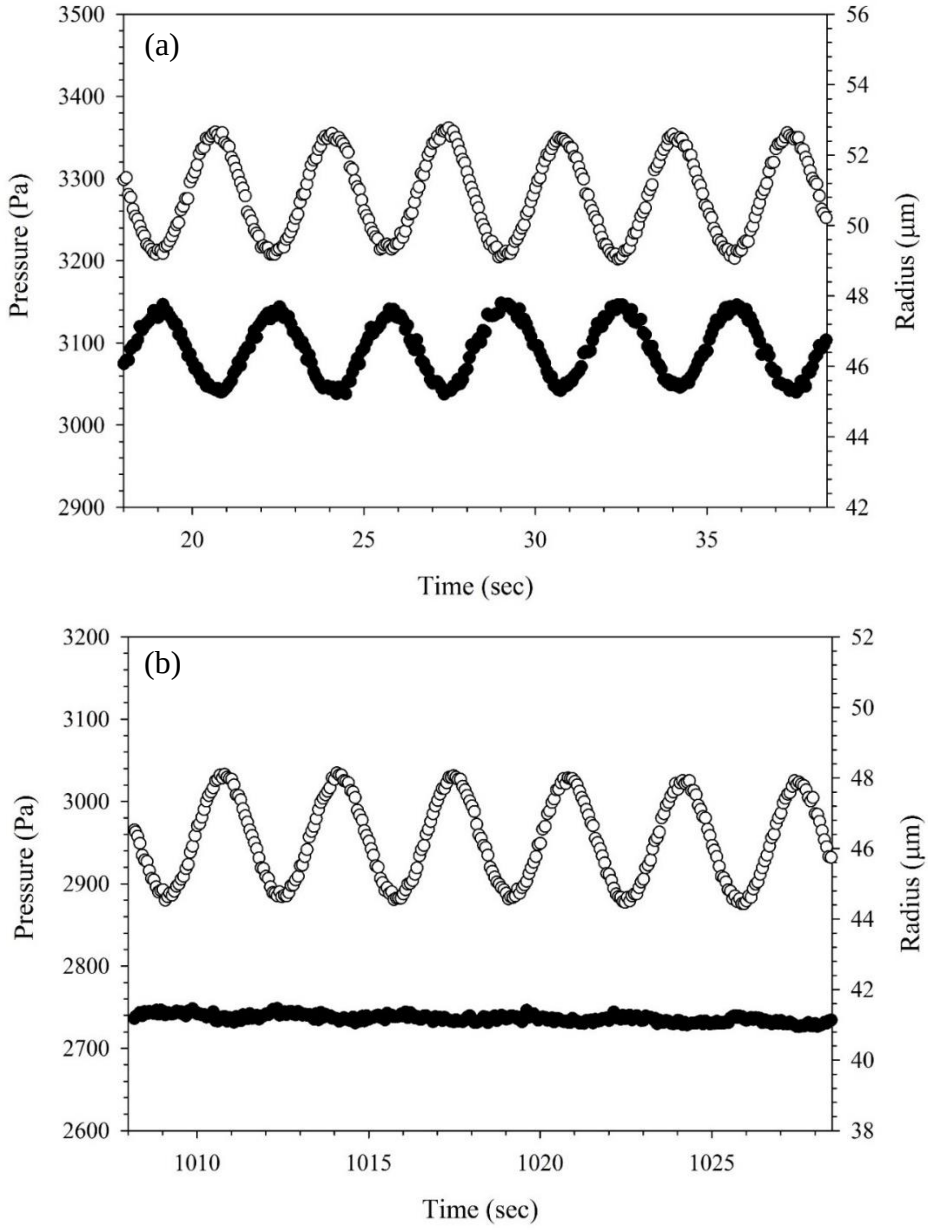

Figure 6.2: Oscillations in the pressure (○) and radius (●) during the measurement of the dilatational modulus of and air/water interface (a) at short times and (b) long times after the interface is exposed to a 0.002 mg/mL CU solution. The dilatational modulus becomes too large to measure at long times, when the amplitude of the radial oscillations decreases below 0.1 μm, the resolution of the imaging method.

At long adsorption times, the value of the amplitude of the radial oscillations decreases to within the noise of the measurement. In these cases, we estimate the minimum possible value of the modulus of the interface from equation (6.3),

assuming the amplitude of the radial oscillations, R_a, is approximately equal to the measurement uncertainty of 0.1 μm. The value of the minimum possible modulus is plotted in Figure 6.1(b) with an open symbol and indicates the lower bound on the dilatational modulus. The reported uncertainty in the minimum modulus calculations arises from the assumption of a value for R_a, as well as the propagation of measurement uncertainty in R_{eq}, P_{eq}, P_a, and R_c in equation (6.3), which can all vary across experiments.

While we are able to mitigate the variability shown in Figure 6.1 by pre-rinsing the reservoir with dilute CU solution, we present the full range of dynamics observed across various initial reservoir residence times and rinsing conditions in Figure 6.3 to highlight the dependence of long-time film formation on bulk solution concentration. Figure 6.3(a) shows the surface pressure as a function of time, and Figure 6.3(b) shows the magnitude of the dilatational modulus as a function of time for repeated adsorption experiments of 0.002 mg/mL CU solution at various initial residence times in the microtensiometer reservoir. Each value of surface pressure in Figure 6.3(a) corresponds to the instantaneous surface pressure during the dilatational modulus measurement at the same time point in Figure 6.3(b). Depleted solutions with low concentrations (such as ▽ and ■ in Figure 6.1) do not obtain the large values of surface pressure and dilatational modulus that are observed in more concentrated solutions, highlighting the importance of timescales in CU adsorption behavior.

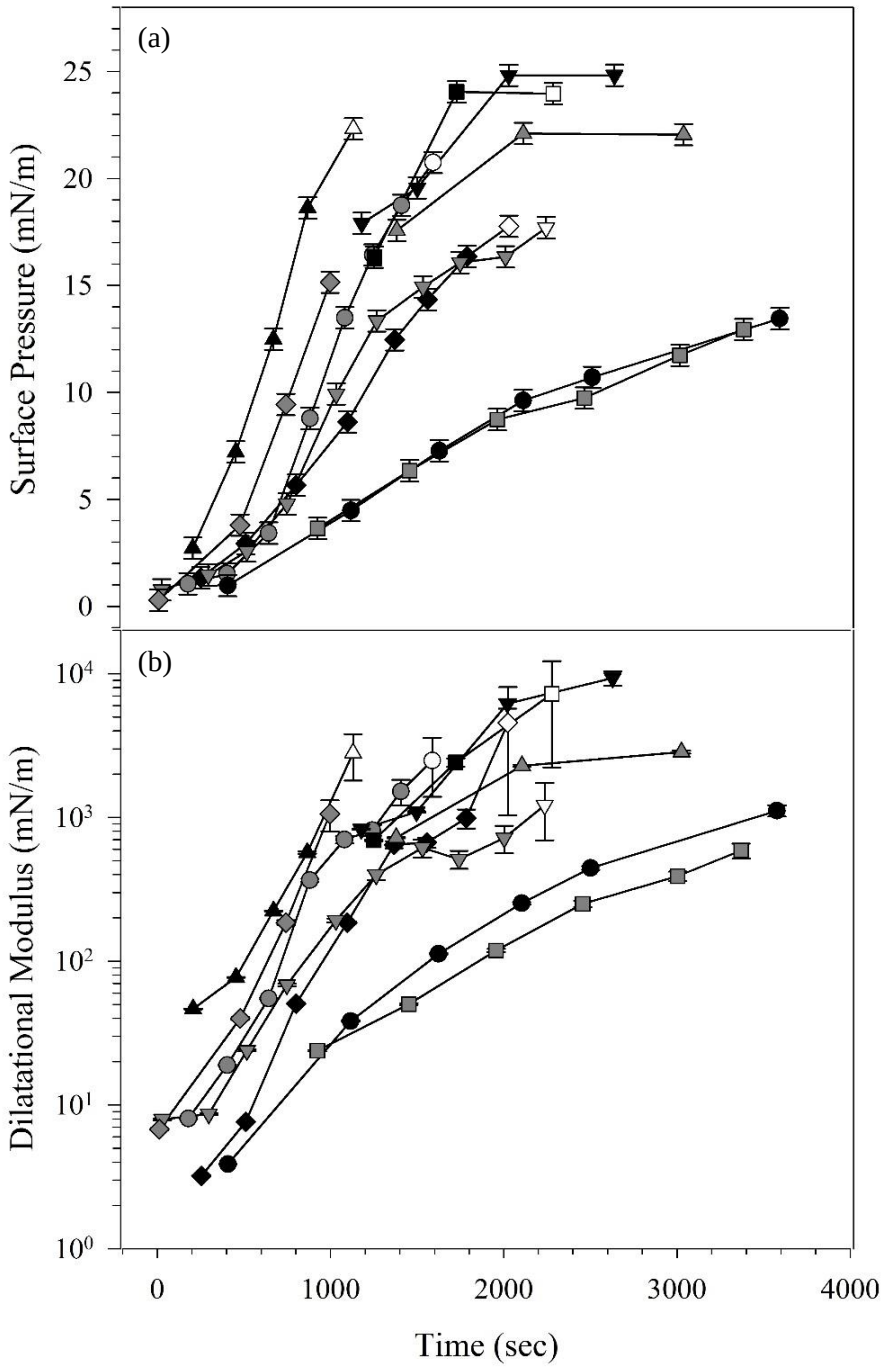

Figure 6.3: (a) Surface pressure and (b) dilatational modulus as a function of time for ten experiments with a 0.002 mg/mL solution of CU. Data points for individual experiments are joined by lines to guide the eye. Both the surface pressure and dilatational modulus increase with time, although the dynamics vary from run to run. Open symbols represent surfaces that have a dilatational modulus too large to measure with small amplitude oscillations; the plotted values represent the minimum modulus for the surface at that time.

Even pre-rinsing the reservoir with dilute CU solution cannot fully eliminate depletion, as each new sample introduced to the reservoir will introduce a new free air/water surface, which still corresponds to a decrease in concentration of about 10%. As such, the true concentration of CU solution will always be less than 0.002 mg/mL, despite all experimental attempts to limit depletion. This issue is likely present in all hydrophobin systems, particularly in instruments that have a small sample volume to surface area ratios, and might explain some of the discrepancies in surface behavior reported in the literature.

The data from Figure 6.3 is used to generate a parametric plot of the dilatational modulus as a function of the surface pressure, shown in Figure 6.4. The variability observed in the individual surface relaxation curves is significantly reduced, and the individual experiments appear to collapse to a single curve, in which the dilatational modulus increases with surface pressure. Assuming that surface pressure is a measure of the degree of surface adsorption, Figure 6.4 indicates that the dilatational modulus is a function of CU surface concentration. The collapse of the data indicates that the interfacial properties (surface pressure and dilatational modulus) are functions of the surface concentration, while the dynamics are driven by transport from bulk solution. In several experiments, the dilatational modulus becomes too large to measure at long times, and the minimum possible values of the modulus are plotted as open symbols. Using both measured and estimated data, we obtain dilatational moduli greater than 1000 mN/m at large surface pressures. These values are much larger than moduli measured for most

other globular protein systems, which typically range from 50 – 150 mN/m,[38–40] and are similar to values obtained for particle-laden interfaces.

To compare the dilatational modulus directly to surface concentration, we apply an equation of state to relate surface pressure and surface concentration. The Volmer model has been applied to other globular proteins at air/water interfaces,[41] and assumes the proteins behave as non-interacting spheres on the interface. The Volmer equation of state is given by the expression,

$$\Pi = \frac{RT}{\left(\frac{1}{\Gamma} - \frac{1}{\Gamma_\infty}\right)} , \tag{6.5}$$

where Γ is the surface concentration, Γ_∞ is the maximum surface concentration, R is the gas constant and T is the temperature. The Volmer model results in an expression for the Gibbs modulus as a function of surface concentration, given by,

$$E_G = -\Gamma \frac{d\Pi}{d\Gamma} = \frac{RT\Gamma\Gamma_\infty^2}{(\Gamma_\infty - \Gamma)^2} . \tag{6.6}$$

The Gibbs modulus predicted using the Volmer equation of state is shown by the solid line plotted in Figure 6.4. The only adjustable parameter in equation (6.6) is the maximum surface concentration. The solid line in Figure 6.4 uses a value of Γ_∞ = 0.39 μmol/m^2, taken from neutron reflectivity studies of HFBII adsorbed at an air/water interface,[13] which we assume has a similar maximum surface concentration to CU.

At low surface pressures, the dilatational modulus agrees qualitatively and quantitatively with the predicted Gibbs modulus, indicating that the measured dilatational modulus is predominantly a result of surface tension changes that occur

as the area of the interface oscillates. At higher surface pressures above 10 mN/m, however, the dilatational modulus begins to deviate from the predicted Gibbs modulus, indicating additional contributions to the modulus beyond surface tension changes arising from dilatational stresses and potential protein-protein interactions. At higher surface pressures and dilatational moduli, the interface becomes incompressible as a rigid protein film forms (as seen in Figure 6.2(b)), indicated by open symbols.

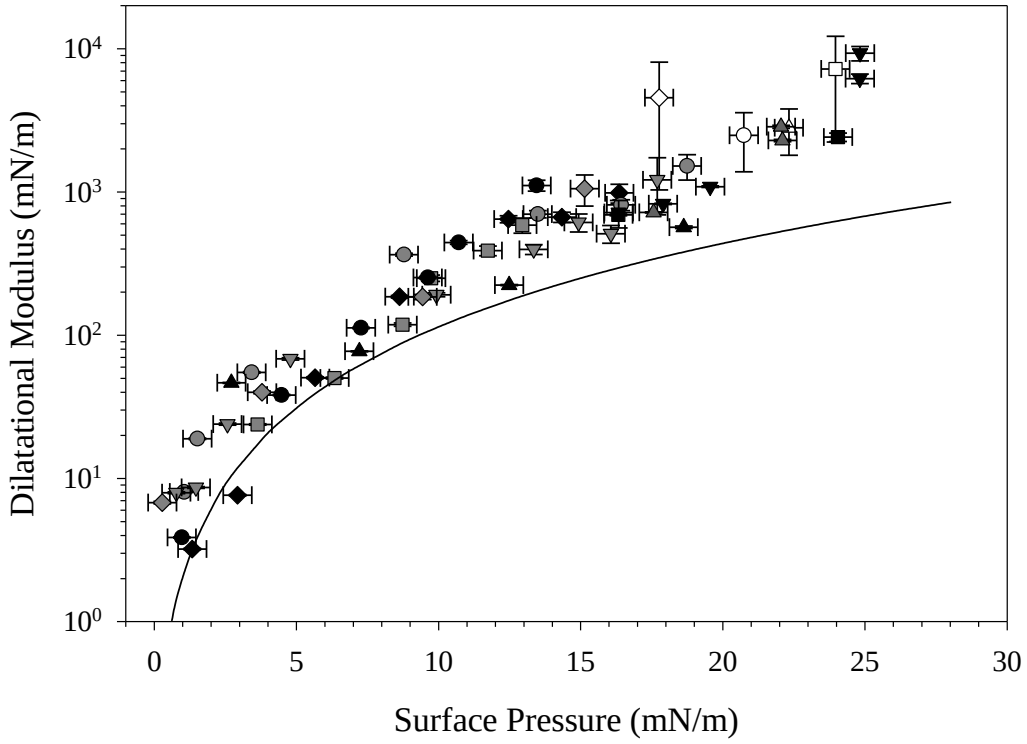

Figure 6.4: Dilatational modulus as a function of surface pressure. The data from Figure 6.3 is plotted parametrically and shown to collapse to a single curve, independent of differences in adsorption dynamics. The solid line is the Gibbs modulus predicted using the Volmer equation of state (equation (6.6)), with a maximum surface concentration of $\Gamma_\infty = 0.39$ μmol/m^2.[13] Open symbols represent surfaces that have a dilatational modulus too large to measure; the plotted values represent the minimum modulus for the surface at that time.

The behavior of the CU film is in agreement with observations of films formed by HFBII.[7–9] In the presence of film formation there is also the potential for bending stresses to become non-negligible, although we have neglected bending stresses in the estimation of the dilatational modulus.

Once a hydrophobin film has formed, we exchange the CU solution with deionized water. The dynamic surface tension during the exchange of the bulk fluid is shown in Figure 6.5. For the first 1650 seconds, the reservoir is filled with 0.002 mg/mL CU solution and the surface pressure increases as the CU adsorbs to the air/water interface, represented by the filled symbols. At 1650 seconds, deionized water is introduced to the reservoir and the CU solution is withdrawn using a peristaltic pump, represented by the open symbols. Flow is maintained for 100 seconds (10 residence times) to ensure complete fluid exchange. After the exchange is complete, the surface pressure is monitored for an additional 200 seconds to ensure the system reaches a steady state surface pressure. At steady state, the dilatational modulus is measured. We assess the effect of the bulk fluid exchange on the protein film by comparing the surface pressure and dilatational modulus before and after rinsing. As shown in Figure 6.5, CU is allowed to adsorb to a clean air/water interface before the bulk fluid is exchanged with deionized water. Rinsing is performed at various adsorption times to assess adsorption irreversibility at different stages of film formation. Figure 6.6(a) compares the surface pressure with CU present in the bulk ("before rinse") to the surface pressure after exchange with deionized water ("after rinse"). Points that coincide with the dashed one to one line exhibit no measurable change in surface tension, indicating completely irreversible

adsorption. Irreversible adsorption is observed for all initial surface pressures greater than 13 mN/m. At lower initial surface pressures, the fluid exchange results in a slight decrease in surface pressure, potentially indicating slight desorption or rearrangement on the interface at low surface coverages.[15,42]

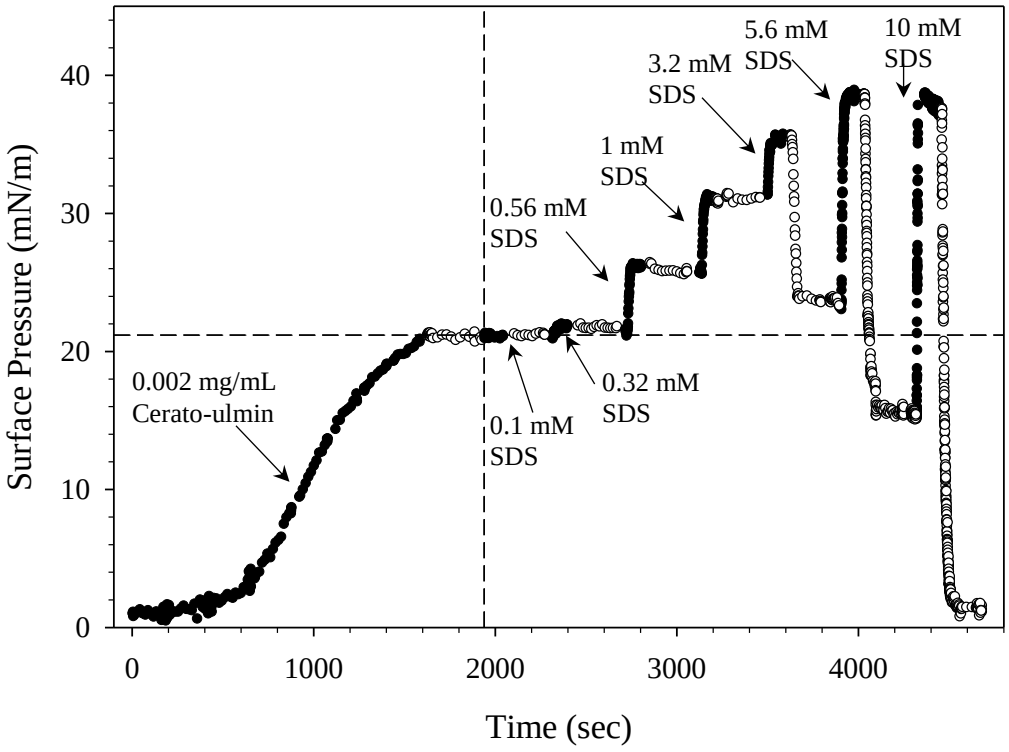

Figure 6.5: Dynamic surface pressure versus time for an air/water interface undergoing several bulk solution exchange steps. Filled symbols indicate adsorption from bulk solution, and open symbols indicate bulk fluid exchange with deionized water. Initially, the Cerato-ulmin adsorbs to the interface. The bulk fluid is exchanged with deionized water starting at 1650 seconds, once a protein film has formed. A 0.1mM SDS solution is introduced to the reservoir at 1950 seconds, indicated by the vertical dashed line. The surface pressure is allowed to reach steady state before the reservoir fluid is again exchanged with deionized water. This process is repeated with several increasing concentrations of SDS, up to 10mM (greater than the critical micelle concentration).

Figure 6.6(b) compares the dilatational modulus of the interface with CU present in the bulk solution to the dilatational modulus after exchange with

deionized water. Each point in Figure 6.6(b) corresponds to a point in Figure 6.6(a). The filled symbols represent systems with low surface pressures and low dilatational moduli that were rinsed before the protein film rigidified. Open symbols represent systems with high surface pressures in which the protein film has rigidified prior to bulk exchange. These interfaces have immeasurably large dilatational moduli, so the minimum possible calculated moduli have been plotted. Half-filled points represent interfaces that exhibited measurable moduli prior to bulk exchange, but became incompressible after rinsing. For the majority of systems, the dilatational modulus remains constant before and after rinsing with deionized water. In two instances, (labeled A and B in Figure 6.6), a significant increase in dilatational modulus is observed upon rinsing, while the surface pressure remains constant. In these cases, we hypothesize that the rinsing procedure results in a slight increase in adsorption or surface rearrangement, induced by convection from the bulk at the beginning of the fluid exchange process.[43] Points A and B suggest that near the rigidification of the CU film, the additional adsorption or rearrangement of CU on the surface has a larger impact on the dilatational modulus than it does on the surface pressure. Across the majority of experiments, however, we observe that rinsing does not have a significant effect on the magnitude of either the surface pressure or the dilatational modulus, indicating that the protein film is adsorbed irreversibly.

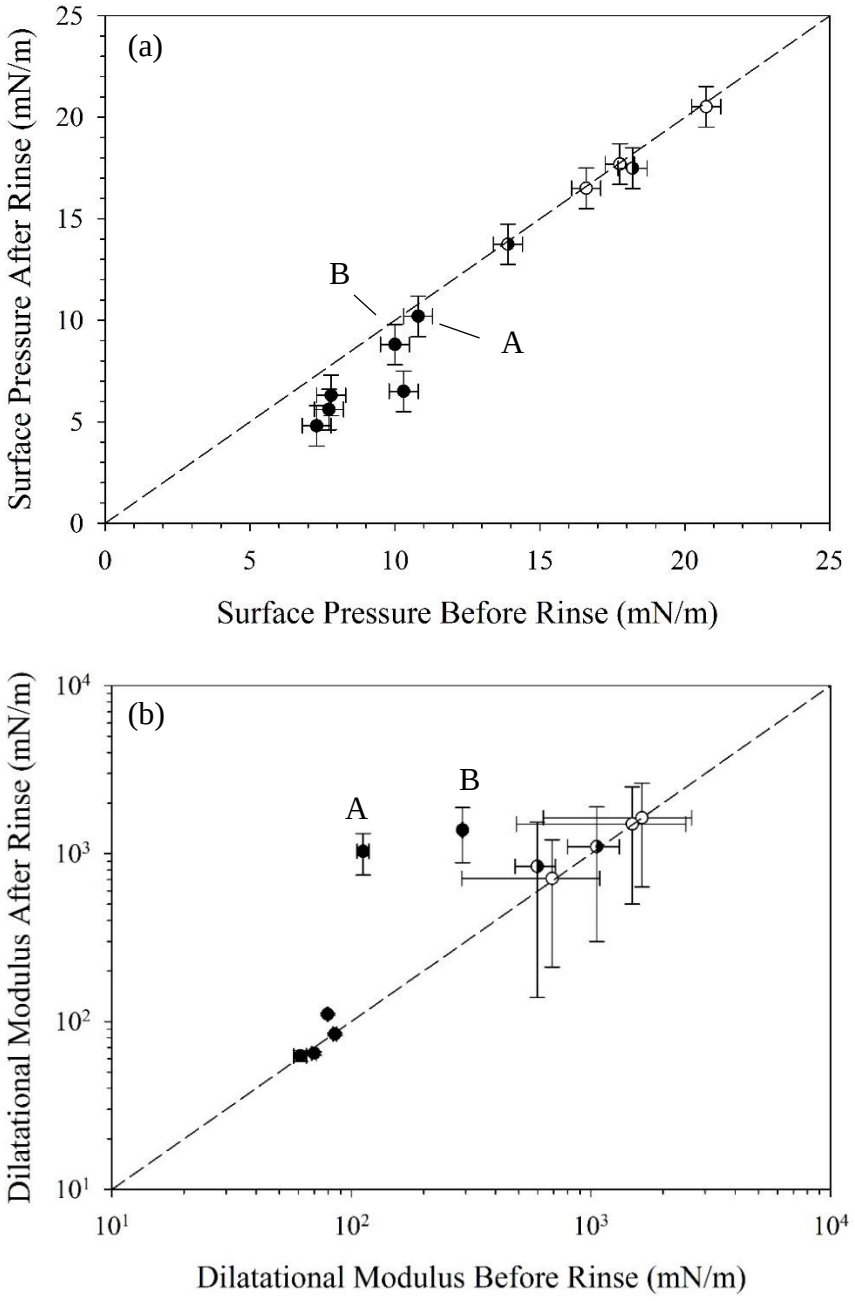

Figure 6.6: (a) Surface pressure before and after exchanging the CU solution with deionized water. Rinsing at low surface coverage (filled symbols) results in a slight decrease in the final surface pressure. Rinsing at high surface coverage (empty symbols) results in a constant surface pressure, indicating irreversible adsorption. (b) Dilatational modulus before and after bulk solution exchange. Surfaces rinsed at low surface coverages (filled symbols) exhibit low dilatational moduli that remain constant after rinsing. Surfaces rinsed at high surface coverages (open symbols) exhibit dilatational moduli too large to measure, and the minimum possible moduli are plotted. Rinsing at intermediate surface coverages results in an increase in the dilatational modulus upon bulk exchange (points A and B).

Assuming CU has a similar structure to HFBII, irreversible adsorption behavior is expected. The energy required to remove one protein molecule from the interface is calculated as $E = \pi r^2 \gamma (1 \pm \cos\theta)^2$, where r is the radius of the protein, γ is the surface tension of the interface, and θ is the contact angle of the protein.[44] Using the HFBII value of r = 1.5 nm,[2] the average measured surface tension at CU film formation, γ = 55 mN/m, and estimating θ = 90°, the energy required for detachment is about 100 kT, indicating irreversible particulate adsorption at air/water interfaces. While irreversible adsorption has been observed for other proteins that denature at interfaces,[45,46] the four strong disulfide bonds responsible for the amphiphilic structure of the hydrophobin prevent denaturation at the interface and suggest particle-like adsorption.

After the bulk solution is exchanged with deionized water, the interface is coated in an irreversibly adsorbed CU film with no species present in the bulk solution. An additional measurement of interfacial mechanics can be obtained by performing a large amplitude compression of the rinsed interface. Figure 6.7 shows the compression and expansion of an interface that has been coated with CU and subsequently rinsed with deionized water. The CU film was not allowed to fully rigidify before rinsing; bulk solution exchange was imposed after the surface pressure reached 6.3 ± 0.5 mN/m and the dilatational modulus reached 115 ± 5 mN/m (conditions similar to the filled points in Figure 6.6). Once the bulk solution was completely replaced with deionized water, the pressure in the capillary was reduced at a constant rate of 11 Pa/s to compress the interface. The resulting surface pressure as a function of surface area is shown in Figure 6.7. As the pressure is

decreased, the surface area of the interface decreases and the surface pressure increases (arrow 1). After compressing, the interface is expanded beyond the initial surface area (arrow 2). The compression is then repeated, beginning from the new larger area (arrow 3) and re-expanded (arrow 2). There is a measurable hysteresis between the compression and expansion of the interface, due to possible rearrangement or reorientation of the adsorbed hydrophobin. The first and second compression cycles overlap, indicating no hydrophobin desorption is induced by the compression.

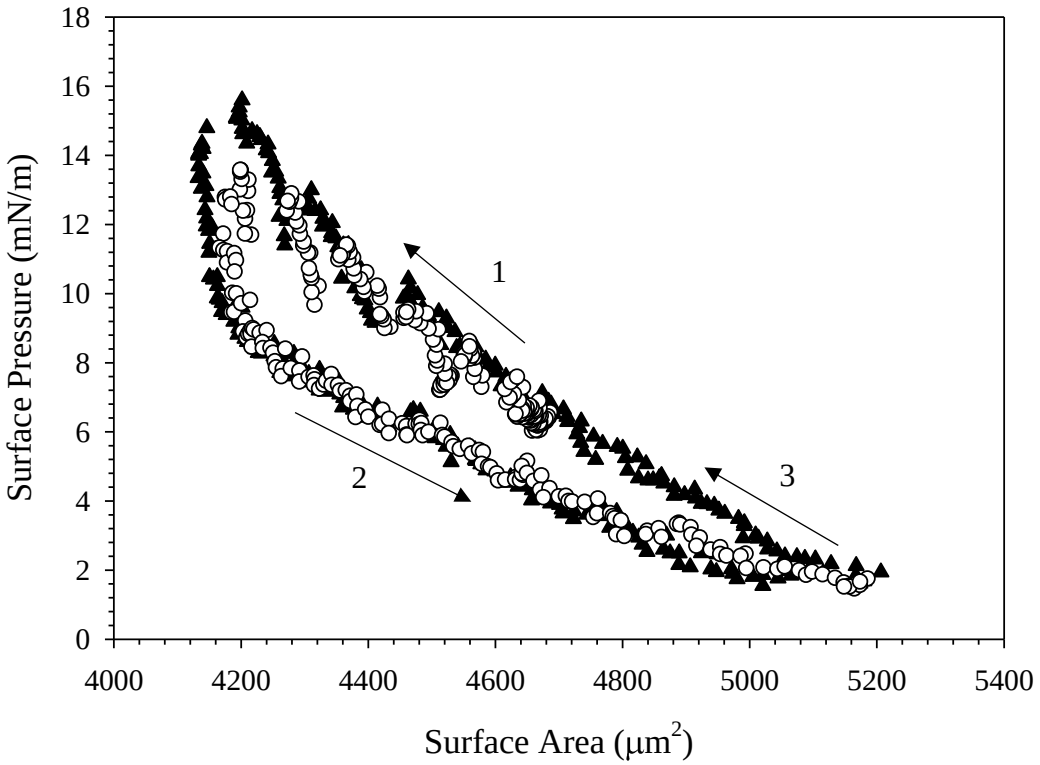

Figure 6.7: Surface pressure as a function of surface area during two compression/expansion cycles of an air/water interface coated with irreversibly adsorbed CU. The first cycle (○) and second cycle (▲) compression isotherms overlap, indicating no desorption due to the compression.

The compression data is used to estimate the Gibbs modulus of the CU film as a function of surface pressure from equation (6.4). Figure 6.8 shows the Gibbs modulus as a function of surface pressure for both compression/expansion cycles in Figure 6.7. The modulus increases with surface pressure, reaching values over 100 mN/m. There is substantial scatter in the Gibbs modulus data, due to the hysteresis between the compression and expansion cycles. The measured Gibbs modulus is larger upon compression than expansion for a given surface pressure.

At approximately 100 μm^2 intervals in Figure 6.7, the large amplitude compression/expansion is paused, and the interface is oscillated using the small-amplitude method to measure the dilatational modulus as a function of surface pressure. After the oscillation the large amplitude compression or expansion is then resumed. In some cases, pausing the compression results in a slight decrease in the surface pressure. The effect is most pronounced at low surface areas, where the surface pressure decreases by up to 4 mN/m during the pause. Similar relaxation behavior has been observed by Stanimirova *et al.*[14] for the stepwise compression of HFBII on a Langmuir trough, and is attributed to hydrophobin rearrangement on the interface,[15] similar to the hysteresis observed between compression and expansion.

The dilatational modulus values obtained during the paused compression/expansion cycles of Figure 6.7 are shown in Figure 6.8 as filled symbols. The values of the dilatational modulus are greater than the values of the Gibbs modulus, indicating the presence of additional contributions to the dilatational modulus beyond changes in surface tension. The Gibbs modulus

predicted by the Volmer model in equation (6.6) is plotted in Figure 6.8 as a solid line. As in Figure 6.4, the model under-predicts the values of the dilatational moduli, but shows improved agreement with the Gibbs modulus data. The only adjustable parameter in equation (6.6) is the maximum surface concentration, taken as $\Gamma_\infty = 0.39$ μmol/m^2 as in Figure 6.4. Despite the hysteresis visible in Figure 6.7, the values of the dilatational modulus for both compression and expansion cycles overlap, again confirming the irreversible adsorption of CU.

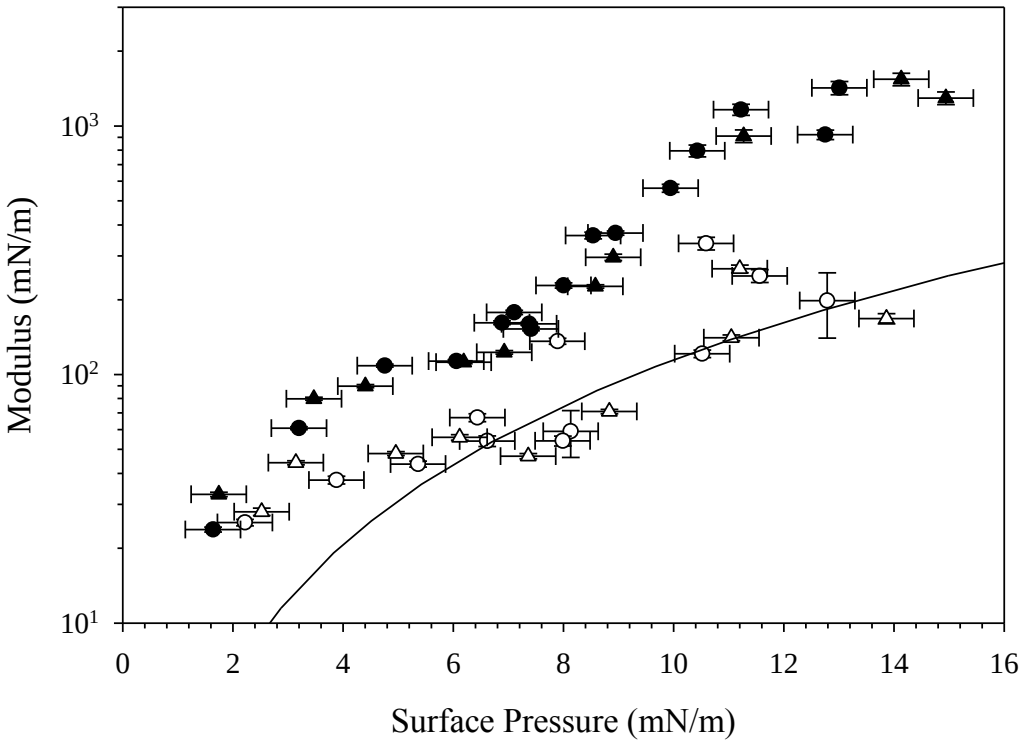

Figure 6.8: Dilatational modulus (filled symbols) and Gibbs modulus (empty symbols) as a function of surface pressure during the first (○) and second (△) compression and expansion cycles of an interface coated with irreversibly adsorbed CU. The solid line is the predicted Gibbs modulus from the Volmer model (equation (6.6)).

We note that this compression analysis can only be performed on interfaces that have not been allowed to rigidify during adsorption. Figure 6.9(a) shows the surface pressure as a function of surface area during the attempted compression of a rigidified interface. The decrease in pressure does not correspond to a change in surface area; instead, the surface pressure increases while the area remains constant. This can be seen more clearly in the raw pressure and radius data obtained for the compression, shown in Figure 6.9(b). Despite a constant decrease of the pressure behind the interface, the bubble radius remains constant until a critical pressure is reached, at which point the interface buckles and collapses. Before the collapse, the Gibbs modulus approaches a value of infinity. Gibbs modulus values of that magnitude are only obtained for interfaces that have been allowed to rigidify through free adsorption from bulk solution. Despite large values of the dilatational modulus reported in Figure 6.8 at high surface pressures, the interface never fully solidifies through manual compression when rinsed at short adsorption times.

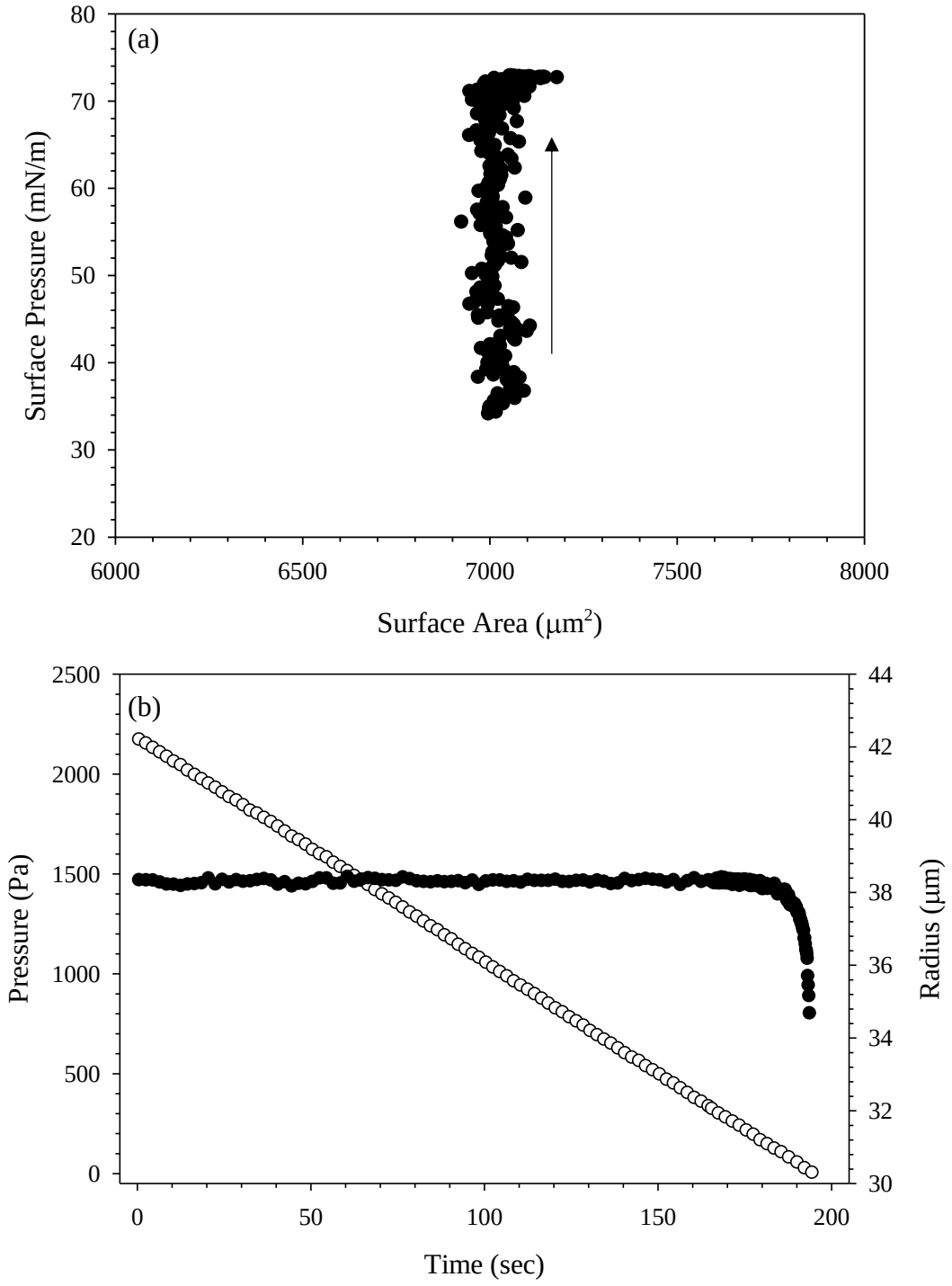

Figure 6.9: (a) Surface pressure as a function of surface area during the compression of a rigid CU film. (b) Pressure (○) and radius (●) as a function of time during the compression experiment in (a). The pressure is reduced at a steady rate of 11 Pa/sec. There is no change in the measured radius until the film buckles and collapses, at 180 seconds.

6.3.2 Sequential Adsorption

For the remainder of this study, we focus on protein films that have fully formed and completely rigidified prior to fluid exchange with deionized water. To characterize the effect of surfactant addition on the incompressible CU films, we introduce sodium dodecyl sulfate (SDS) to the pre-formed protein films. Following the procedure illustrated in Figure 6.5, we expose the air/water interface coated with the CU film to a dilute SDS solution starting at 1950 seconds, indicated by the vertical dashed line. After the system reaches a steady state surface pressure (at least 200 seconds after the completion of the bulk exchange), the dilatational modulus is measured. The surfactant solution is then exchanged with deionized water, and the surface pressure and dilatational modulus are measured with no species present in the reservoir fluid. The procedure is repeated with SDS solutions of increasing concentration until the critical micelle concentration (CMC = 8.2 mM)[47] of SDS is reached.

To quantify changes in the surface pressure and dilatational modulus of the film resulting from exposure to SDS, we define Π_∞ as the surface pressure of the rigidified hydrophobin film after rinsing with deionized water, but before any surfactant is introduced to the system. For example, in Figure 6.5, Π_∞ = 21.8 mN/m, indicated by the horizontal dashed line. A normalized surface pressure is then defined as $\Pi = \frac{\Pi_{SDS}}{\Pi_\infty}$, where Π_{SDS} is the steady state surface pressure with SDS in the reservoir. The normalized surface pressure as a function of bulk SDS concentration is plotted in Figure 6.10(a) for three different CU films, each with a different initial surface pressure, Π_∞ of 13.9 mN/m (■), 17.1 mN/m (▼), and 21.8

mN/m (●). All films were fully rigidified before rinsing and exposure to SDS, with moduli values greater than 800 mN/m. At low SDS concentrations, the normalized surface pressure remains at a value of unity; i.e., the surface pressure does not change when SDS is added to the system. At SDS concentrations greater than 0.32 mM, the normalized surface pressure increases with increasing SDS concentration. We assume that CU does not desorb from the air/water interface, so an increase in the normalized surface pressure suggests that SDS co-adsorbs to the pre-formed hydrophobin layer. The vertical dashed line indicates the concentration above which a significant increase in normalized surface pressure is observed. An increase in surface pressure at SDS concentrations of 0.32 mM and greater is consistent with SDS adsorption behavior at a clean air/water interface.[47] The concentrations of SDS that result in increased surface pressures are 100-10,000 times more concentrated than the initial CU solution. At the highest concentrations of SDS, the largest increase in surface pressure is observed for the system with the lowest initial surface pressure (Π_∞ = 13.9 mN/m, ■).

For adsorption of SDS to cause an increase in the surface pressure, the molecules must adsorb to available space on the air/water interface, either between the CU molecules or at the CU/air/water contact line. Neutron reflectivity measurements of HFBII indicate that the maximum adsorption volume fraction is about 0.7,[13] leaving sufficient surface area available for SDS adsorption. To compare SDS adsorption on a pre-formed CU film to SDS adsorption at a clean air/water interface, we estimate the SDS surface coverage using the Frumkin isotherm,[48] assuming that any increase in surface pressure above Π_∞ is exclusively

due to the adsorption of SDS at the air/water interface. This provides an estimate of the effective surface concentration of SDS from the measured change in surface pressure. The inset in Figure 6.10 plots the normalized SDS surface concentration, Γ/Γ_∞, as a function of bulk SDS concentration for each CU film. The solid curve is the normalized SDS surface concentration at a clean air/water interface calculated from the Frumkin model, using a maximum surface concentration value of $\Gamma_\infty = 3.9$ $\mu mol/m^2$.[48] Below bulk SDS concentrations of 2 mM, the predicted SDS surface concentration in the mixed interface is greater than the SDS surface concentration at a clean interface. This suggests that the presence of CU enhances SDS adsorption at the interface, despite CU molecules occupying a substantial amount of the interfacial area available for SDS adsorption. For bulk SDS concentrations of 5.6 mM and greater, the surface coverage on the mixed interface is slightly less than the predicted adsorption at a clean interface.

When SDS is added to the reservoir, there is also the possibility of SDS adsorption to the reservoir walls and complex formation with any CU adsorbed there. To ensure these potential complexes are not the sources of the increased surface pressures in Figure 6.10(a), we performed a control experiment to test complex adsorption at the air/water interface of the capillary. In a reservoir that was exposed to CU solution and rinsed with deionized water, we introduced a 2 mM SDS solution to a clean air/water interface at the capillary and monitored the surface tension and dilatational modulus. The values we obtained are identical to those of a pure 2 mM SDS solution, indicating that any complex formation at the walls do not migrate to the measured air/water interface in the timescales of the experiment.

The increased surface pressures in Figure 6.10(a) are due to positive SDS-CU interactions at the interface, rather than any complex adsorption.

Figure 6.10(b) shows the dilatational modulus of the interface as a function of SDS concentration. For all three CU films, the dilatational modulus before exposure to SDS is too large to measure. At low concentrations of SDS, the modulus remains too large to measure, and the lower bound on the modulus is plotted using open symbols. As the SDS concentration increases, the dilatational modulus decreases, indicating that the SDS acts to decrease the rigidity of the CU film. At 10 mM SDS, which is a concentration slightly larger than the CMC of SDS, the modulus has decreased to a value less than 20 mN/m for all three films, representing a decrease of at least two orders of magnitude from that of the initial hydrophobin film. At this concentration, the dilatational modulus is equivalent to that of a pure 10 mM SDS solution, indicating that the SDS has likely displaced the CU from the interface entirely. Measuring the dilatational modulus while SDS is present in the bulk solution is complicated by surfactant transport to the interface.[32,49,50] These measurements are performed at a single frequency (1.9 rad/sec) to illustrate the co-adsorption of SDS to the pre-formed CU film. The dilatational modulus measurements themselves do not impact SDS adsorption behavior. All oscillations are performed within the small amplitude limit, and the surface pressure remains constant before and after the oscillations for every SDS concentration.

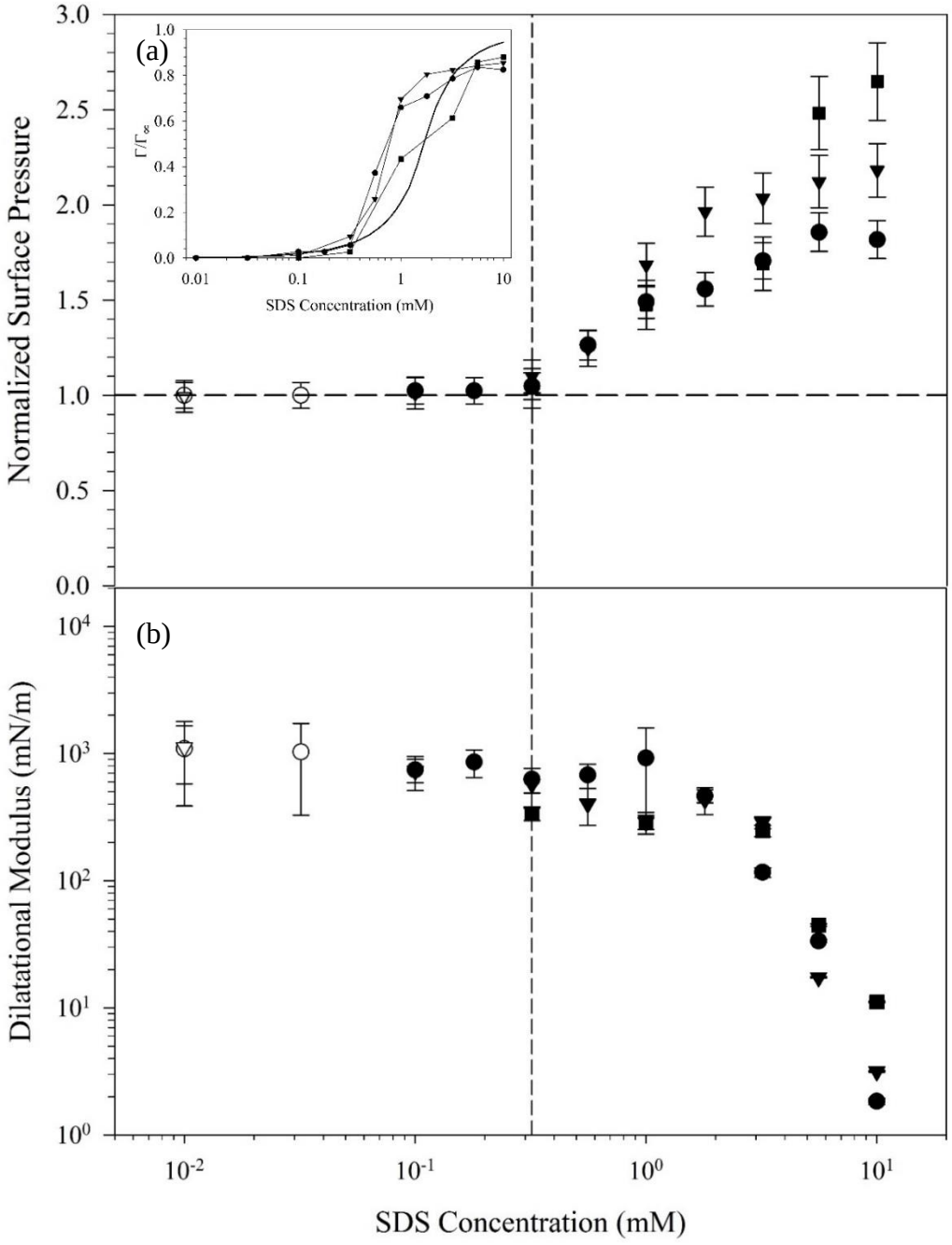

Figure 6.10: (a) Normalized surface pressure as a function of bulk SDS concentration. All surfaces were incompressible prior to exposure to SDS. Each data set corresponds to a different initial surface pressure: 13.9 mN/m (■), 17.1 mN/m (▼), and 21.8 mN/m (●). Inset: normalized surface concentration of SDS as a function of bulk concentration. The solid curve is the surface concentration for SDS adsorption at a clean air/water interface. (b) Dilatational modulus as a function of bulk SDS concentration. The dilatational modulus is initially too large to measure.

Figure 6.10 shows that SDS is able to adsorb to the CU film and lower the dilatational modulus of the film while SDS is present in the bulk solution. The state of the interface at each rinsing step with no surfactant present in the reservoir, shown as open symbols in Figure 6.5, provides a measure of the persistence of the CU film after exposure to surfactant. SDS itself adsorbs reversibly to air/water interfaces; in the absence of CU, exchanging the bulk solution with deionized water would be expected to remove SDS from the interface. To compare the surface pressure of the original CU film with that of the interface that has been exposed to SDS and rinsed with deionized water, we now define a normalized surface pressure as $\Pi = \frac{\Pi_{rinsed}}{\Pi_{\infty}}$, where Π_{rinsed} is the surface pressure of the interface after SDS exposure and rinsing. Figure 6.11(a) plots the normalized surface pressure of the rinsed interface as a function of the SDS concentration that had been in the reservoir prior to rinsing. At low concentrations, there is no measurable change in surface pressure. At concentrations greater than 0.32 mM (indicated by the vertical dashed line) and less than 5.6 mM, the normalized surface pressure increases, consistent with the observation when SDS is present in the bulk solution (Figure 6.10(a)). The increase in normalized surface pressure corresponds to an increase in SDS adsorption. SDS adsorbs reversibly to clean air/water interfaces; the persistent increase in normalized surface pressure indicates that the presence of CU allows some SDS to remain adsorbed at the interface even after rinsing.

The formation of hydrophobin-surfactant complexes in the bulk observed for HFBII[20] suggests that SDS is likely adsorbing to the CU molecules themselves at the air/water interface. Simply assuming monolayer adsorption of SDS around a

CU molecule would increase the estimated adsorption energy by almost an order of magnitude for the CU-SDS complex, supporting the observation of persistent SDS adsorption despite rinsing. The SDS concentrations that result in increased surface pressures after rinsing in Figure 6.11(a) coincide with increased SDS adsorption compared to a clean air/water interface, as shown in the Figure 6.7 inset.

For SDS concentrations greater than 5.6 mM, the normalized surface pressure decreases below a value of unity, and at 10 mM SDS the normalized surface pressure approaches zero. A normalized surface pressure less than unity means the surface pressure has decreased below the surface pressure of the original rigidified CU film after rinsing, but prior to the introduction of SDS; this original surface pressure is shown as the horizontal dashed line in Figure 6.5. Assuming that surface pressure is a measure of surface coverage, the decrease in normalized surface pressure below unity indicates that some of the initial CU has desorbed from the air/water interface. A normalized surface pressure of zero indicates total desorption of CU and SDS from the interface, and is achieved only at the highest SDS concentration.

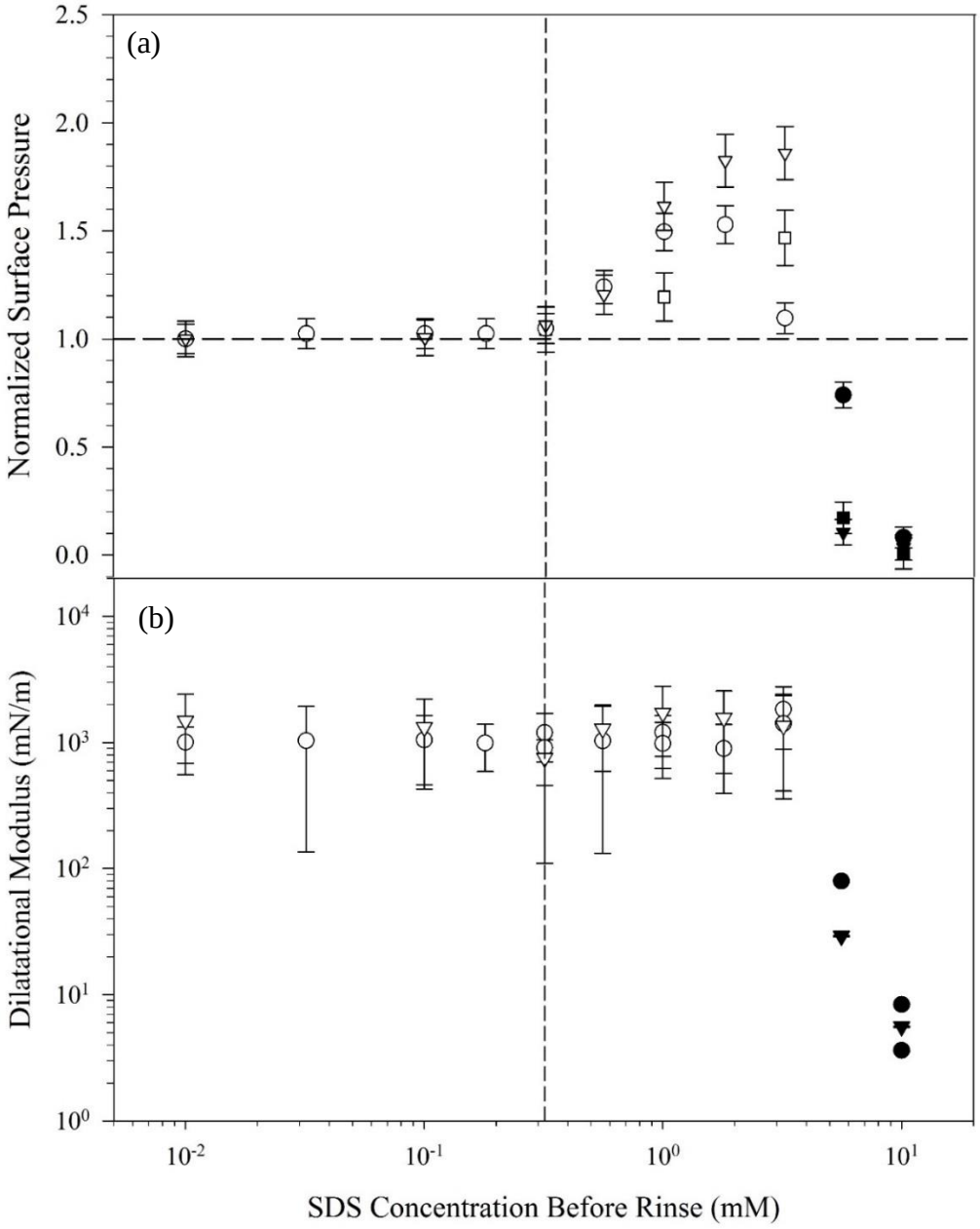

Figure 6.11: (a) Normalized surface pressure for the rinsed interface as a function of SDS concentration before exchanging the bulk solution with deionized water. Initial surface pressures for each CU film are 13.9 mN/m (■), 17.1 mN/m (▼), and 21.8 mN/m (●). At concentrations below 0.32 mM SDS, there is no observed change in the surface pressure. (b) Dilatational modulus of the rinsed interface as a function of SDS concentration before rinsing with deionized water. For concentrations less than 5.6 mM SDS, the modulus remains too large to measure, represented by open symbols.

Figure 6.11(b) shows the dilatational modulus as a function of the SDS concentration in the reservoir immediately prior to rinsing. For SDS concentrations less than 5.6 mM, the dilatational modulus remains too large to measure, and the lower bounds of the moduli are plotted as open symbols. This behavior deviates from the dilatational moduli measured with SDS in the bulk phase at the same concentrations (shown in Figure 6.10(b)), where the values of the moduli were signficantly smaller. The immeasurably large dilatational modulus values obtained after rinsing indicate that the low moduli reported in Figure 6.10(b) are due to surfactant transport to the free space on the surface, rather than CU desorption. At concentrations greater than 5.6 mM, the dilatational modulus decreases rapidly, approaching zero, supporting the hypothesis that the CU completely desorbs from the interface at high surfactant concentrations.

The behavior of the rinsed interface at high and low concentrations of SDS agrees with prior observations of the coadsorption of SDS and HFBII.[13,16] At high surfactant concentrations, SDS dominates the air/water interface in parallel adsorption experiments with HFBII. During parallel adsorption, SDS and HFBII are both present in the bulk solution and form surfactant-hydrophobin complexes that prevent HFBII from adsorbing at the interface at sufficiently large SDS concentrations.[13] In the sequential adsorption experiments performed here, no complexes are formed in the bulk solution, since SDS and CU are never present in the reservoir at the same time. Instead, SDS displaces the pre-adsorbed CU from the interface at the highest surfactant concentrations, disrupting the rigidified protein film. This is a fundamentally different experimental observation than has

been previously reported; rather than preventing CU adsorption, here we observe that SDS successfully disrupts a fully rigidified protein film. Since SDS adsorbs reversibly, rinsing the interface with deionized water results in the desorption of SDS from the interface, indicated by the decrease in normalized surface pressure and dilatational modulus. These observations differ from the sequential adsorption experiments performed by Stanimirova *et al.*[16], where high concentrations of SDS could not fully remove HFBII from the interface. However, the authors did not allow the HFBII films to rigidify before exposing them to SDS, while our study solely considers fully rigidified CU films. As seen in Figure 6.1, the adsorption behavior of CU at short times varies significantly with the bulk solution concentration. The sequential adsorption experiments we attempted on non-rigidified films resulted in irreproducible interfacial behavior, again indicating that interfacial measurements are highly sensitive to bulk concentration, adsorption time, and surface coverage.

Additionally, the behavior of the mixed hydrophobin-surfactant interface at intermediate concentrations between 0.32 mM and 5.6 mM SDS is not predicted by co-adsorption results. The formation of an incompressible hydrophobin film does not occur with mixed surfactant-protein systems; for example, the modulus of the SDS-HFBII mixed interface measured by Stanimirova *et al.*[16] is substantially lower than the modulus of a pure HFBII layer. By using a sequential adsorption procedure and pre-forming an incompressible CU layer before exposing it to a SDS solution, we achieve co-adsorption while maintaining a large dilatational modulus. Mixed hydrophobin-surfactant interfaces with these unique mechanical properties are only

acheiveable by carefully controlling the formation method, highlighting the differences between bulk complex formation and interfacial interaction between the protein and surfactant.

6.4 SUMMARY

We have characterized the adsorption of a dilute Cerato-ulmin solution at air/water interfaces. The measured surface pressure and dilatational modulus increase with increasing CU adsorption. We use the Volmer equation of state to predict the relationship between surface pressure and dilatational modulus at low surface coverages. At high surface coverages, an incompressible protein film forms, and the dilatational modulus deviates substantially from the predicted Volmer model Gibbs modulus.

CU adsorption is irreversible, exhibiting no significant desorption upon fluid exchange with deionized water. The protein film remains rigid and incompressible after the fluid exchange. SDS coadsorbs to the pre-formed CU film. For SDS concentrations greater than 0.32 mM with surfactant present in the bulk solution, the surface pressure increases with SDS concentration while the dilatational modulus decreases, indicating that SDS is adsorbing to the interface and decreasing the rigidity of the CU film.

Exchanging the bulk solution with deionized water after exposing the CU film to SDS reveals behavior that strongly depends on surfactant concentration. At high SDS concentrations near the CMC, the surface pressure and dilatational

modulus decrease substantially upon rinsing, indicating near total desorption of CU and SDS.

At moderate concentrations, some SDS remains adsorbed on the surface with CU, creating a mixed layer that retains an extremely large dilatational modulus. This mixed layer is fundamentally different from layers formed by co-adsorption from solution, where surfactant-protein complexes adsorb together and do not form rigid, incompressible films. SDS can both disrupt and displace a pre-formed hydrophobin film, as well as contribute to a mixed adsorption layer. The potential use of hydrophobins as foam and emulsion stabilizers depends on their ability to form rigid interfacial films in mixed systems. These results highlight the importance of formation method on the interfacial mechanics that contribute to overall formulation stability.

REFERENCES

(1) Hektor, H. J.; Scholtmeijer, K. Hydrophobins: Proteins with Potential. *Curr. Opin. Biotechnol.* **2005**, *16*, 434–439.

(2) Hakanpää, J.; Paananen, A.; Askolin, S.; Nakari-Setälä, T.; Parkkinen, T.; Penttilä, M.; Linder, M. B.; Rouvinen, J. Atomic Resolution Structure of the HFBII Hydrophobin, a Self-Assembling Amphiphile. *J. Biol. Chem.* **2004**, *279*, 534–539.

(3) Wessels, J. Hydrophobins, Unique Fungal Proteins. *Mycologist* **2000**, *14*, 153–159.

(4) Linder, M. B. Hydrophobins: Proteins That Self Assemble at Interfaces. *Curr. Opin. Colloid Interface Sci.* **2009**, *14*, 356–363.

(5) Wösten, H. A. B. Hydrophobins: Multipurpose Proteins. *Annu. Rev. Microbiol.* **2001**, *55*, 625–646.

(6) Burke, J.; Cox, A.; Petkov, J.; Murray, B. S. Interfacial Rheology and Stability of Air Bubbles Stabilized by Mixtures of Hydrophobin and β-Casein. *Food Hydrocoll.* **2014**, *34*, 119–127.

(7) Basheva, E. S.; Kralchevsky, P. a.; Christov, N. C.; Danov, K. D.; Stoyanov, S. D.; Blijdenstein, T. B. J.; Kim, H. J.; Pelan, E. G.; Lips, A. Unique Properties of Bubbles and Foam Films Stabilized by HFBII Hydrophobin. *Langmuir* **2011**, *27*, 2382–2392.

(8) Cox, A. R.; Cagnol, F.; Russell, A. B.; Izzard, M. J. Surface Properties of Class II Hydrophobins from Trichoderma Reesei and Influence on Bubble Stability. *Langmuir* **2007**, *23*, 7995–8002.

(9) Szilvay, G. R.; Paananen, A.; Laurikainen, K.; Vuorimaa, E.; Lemmetyinen, H.; Peltonen, J.; Linder, M. B. Self-Assembled Hydrophobin Protein Films at the Air-Water Interface: Structural Analysis and Molecular Engineering. *Biochemistry* **2007**, *46*, 2345–2354.

(10) Kisko, K.; Szilvay, G. R.; Vuorimaa, E.; Lemmetyinen, H.; Linder, M. B.; Torkkeli, M.; Serimaa, R. Self-Assembled Films of Hydrophobin Proteins HFBI and HFBII Studied in Situ at the Air/Water Interface. *Langmuir* **2009**, *25*, 1612–1619.

(11) Wösten, H. a. B.; Scholtmeijer, K. Applications of Hydrophobins: Current State and Perspectives. *Appl. Microbiol. Biotechnol.* **2015**, *99*, 1587–1597.

(12) Green, A. J.; Littlejohn, K. A.; Hooley, P.; Cox, P. W. Formation and Stability of Food Foams and Aerated Emulsions: Hydrophobins as Novel

Functional Ingredients. *Curr. Opin. Colloid Interface Sci.* **2013**, *18*, 292–301.

(13) Zhang, X. L.; Penfold, J.; Thomas, R. K.; Tucker, I. M.; Petkov, J. T.; Bent, J.; Cox, A.; Campbell, R. A. Adsorption Behaviour of Hydrophobin and Hydrophobin / Surfactant Mixtures at the Air-Water Interface. *Langmuir* **2011**, *27*, 11316–11323.

(14) Stanimirova, R. D.; Gurkov, T. D.; Kralchevsky, P. a; Balashev, K. T.; Stoyanov, S. D.; Pelan, E. G. Surface Pressure and Elasticity of Hydrophobin HFBII Layers on the Air-Water Interface: Rheology Versus Structure Detected by AFM Imaging. *Langmuir* **2013**, *29*, 6053–6067.

(15) Alexandrov, N. A.; Marinova, K. G.; Gurkov, T. D.; Danov, K. D.; Kralchevsky, P. A.; Stoyanov, S. D.; Blijdenstein, T. B. J.; Arnaudov, L. N.; Pelan, E. G.; Lips, A. Interfacial Layers from the Protein HFBII Hydrophobin: Dynamic Surface Tension, Dilatational Elasticity and Relaxation Times. *J. Colloid Interface Sci.* **2012**, *376*, 296–306.

(16) Stanimirova, R. D.; Marinova, K. G.; Danov, K. D.; Kralchevsky, P. A.; Basheva, E. S.; Stoyanov, S. D.; Pelan, E. G. Competitive Adsorption of the Protein Hydrophobin and an Ionic Surfactant: Parallel vs Sequential Adsorption and Dilatational Rheology. *Colloids Surfaces A Physicochem. Eng. Asp.* **2014**, *457*, 307–317.

(17) Blijdenstein, T. B. J.; de Groot, P. W. N.; Stoyanov, S. . On the Link Between Foam Coarsening and Surface Rheology: Why Hydrophobins Are So Different. *Soft Matter* **2010**, *6*, 1799–1808.

(18) Aumaitre, E.; Vella, D.; Cicuta, P. On the Measurement of the Surface Pressure in Langmuir Films with Finite Shear Elasticity. *Soft Matter* **2011**, *7*, 2530–2537.

(19) Dickinson, E. Proteins at Interfaces and in Emulsions: Stability, Rheology and Interactions. *J. Chem. Soc. Faraday Trans.* **1998**, *94*, 1657–1669.

(20) Zhang, X. L.; Penfold, J.; Thomas, R. K.; Tucker, I. M.; Petkov, J. T.; Bent, J.; Cox, A.; Grillo, I. Self-Assembly of Hydrophobin and Hydrophobin/Surfactant Mixtures in Aqueous Solution. *Langmuir* **2011**, *27*, 10514–10522.

(21) Dickinson, E. Adsorbed Protein Layers at Fluid Interfaces: Interactions, Structure and Surface Rheology. *Colloids Surfaces B Biointerfaces* **1999**, *15*, 161–176.

(22) Tucker, I. M.; Petkov, J. T.; Penfold, J.; Thomas, R. K.; Cox, A. R.; Hedges, N. Adsorption of Hydrophobin–Protein Mixtures at the Air–Water Interface: The Impact of pH and Electrolyte. *Langmuir* **2015**, *31*, 10008–

10016.

(23) Kirby, S. M.; Anna, S. L.; Walker, L. M. Sequential Adsorption of an Irreversibly Adsorbed Nonionic Surfactant and an Anionic Surfactant at an Oil/Aqueous Interface. *Langmuir* **2015**, *31*, 4063–4071.

(24) Svitova, T. F.; Radke, C. J. AOT and Pluronic F68 Coadsorption at Fluid / Fluid Interfaces : A Continuous-Flow Tensiometry Study. *Ind. Eng. Chem. Res* **2005**, *44*, 1129–1138.

(25) Romoscanu, A. I.; Mezzenga, R. Cross Linking and Rheological Characterization of Adsorbed Protein Layers at the Oil-Water Interface. *Langmuir* **2005**, *21*, 9689–9697.

(26) Russo, P. S.; Blum, F. D.; Ipsen, J. D.; Abul-Hajj, Y. J.; Miller, W. G. The Surface Activity of the Phytotoxin Cerato-Ulmin. *Can. J. Bot.* **1982**, *60*, 1414–1420.

(27) Stringer, M. A.; Timberlake, W. E. Cerato-Ulmin, a Toxin Involved in Dutch Elm Disease, Is a Fungal Hydrophobin. *Plant Cell* **1993**, *5*, 145–146.

(28) Russo, P. S.; Blum, F. D.; Ipsen, J. D.; Abul-Hajj, Y. J.; Miller, W. G. The Solubility and Surface Activity of the Ceratocystis Ulmi Toxin Cerato-Ulmin. *Physiol. Plant Pathol.* **1981**, *19*, 113–126.

(29) Takai, S.; Richards, W. C. Cerato-Ulmin, a Wilting Toxin of Ceratocystic Ulmi: Isolation and Some Properties of Cerato-Ulmin from the Culture of C. Ulmi. *Phytopath* **1978**, *91*, 129–146.

(30) Stevenson, K. J.; Slater, J. A.; Takai, S. Cerato-Ulmin-A Wilting Toxin of Dutch Elm Disease Fungus. *Phytochemistry* **1979**, *18*, 235–238.

(31) Alvarez, N. J.; Walker, L. M.; Anna, S. L. A Microtensiometer to Probe the Effect of Radius of Curvature on Surfactant Transport to a Spherical Interface. *Langmuir* **2010**, *26*, 13310–13319.

(32) Alvarez, N.; Walker, L.; Anna, S. Diffusion-Limited Adsorption to a Spherical Geometry: The Impact of Curvature and Competitive Time Scales. *Phys. Rev. E* **2010**, *82*, 11604.

(33) Reichert, M. D.; Walker, L. M. Interfacial Tension Dynamics, Interfacial Mechanics, and Response to Rapid Dilution of Bulk Surfactant of a Model Oil-Water-Dispersant System. *Langmuir* **2013**, *29*, 1857–1867.

(34) Reichert, M. D.; Walker, L. M. Coalescence Behavior of Oil Droplets Coated in Irreversibly-Adsorbed Surfactant Layers. *J. Colloid Interface Sci.* **2015**, *449*, 480–487.

(35) Kotula, A. P.; Anna, S. L. Regular Perturbation Analysis of Small Amplitude Oscillatory Dilatation of an Interface in a Capillary Pressure Tensiometer. *J. Rheol. (N. Y. N. Y).* **2015**, *59*, 85–117.

(36) Lumsdon, S. O.; Green, J.; Stieglitz, B. Adsorption of Hydrophobin Proteins at Hydrophobic and Hydrophilic Interfaces. *Colloids Surfaces B Biointerfaces* **2005**, *44*, 172–178.

(37) Linder, M.; Szilvay, G. R.; Nakari-Setälä, T.; Söderlund, H.; Penttilä, M. Surface Adhesion of Fusion Proteins Containing the Hydrophobins HFBI and HFBII from Trichoderma Reesei. *Protein Sci.* **2002**, *11*, 2257–2266.

(38) Petkov, J. T.; Gurkov, T. D.; Campbell, B. E.; Borwankar, R. P. Dilatational and Shear Elasticity of Gel-like Protein Layers on Air/Water Interface. *Langmuir* **2000**, *16*, 3703–3711.

(39) Lucassen-Reynders, E. H.; Fainerman, V. B.; Miller, R. Surface Dilational Modulus or Gibbs' Elasticity of Protein Adsorption Layers. *J. Phys. Chem. B* **2004**, *108*, 9173–9176.

(40) Bos, M. A.; van Vliet, T. Interfacial Rheological Properties of Adsorbed Protein Layers and Surfactants: A Review. *Adv. Colloid Interface Sci.* **2001**, *91*, 437–471.

(41) Gurkov, T. D.; Russev, S. C.; Danov, K. D.; Ivanov, I. B.; Campbell, B. Monolayers of Globular Proteins on the Air/water Interface: Applicability of the Volmer Equation of State. *Langmuir* **2003**, *19*, 7362–7369.

(42) Krivosheeva, O.; Deìdinaiteì, A.; Linder, M. B.; Tilton, R. D.; Claesson, P. M. Kinetic and Equilibrium Aspects of Adsorption and Desorption of Class II Hydrophobins HFBI and HFBII at Silicon Oxynitride/water and Air/water Interfaces. *Langmuir* **2013**, *29*, 2683–2691.

(43) Alvarez, N. J.; Vogus, D. R.; Walker, L. M.; Anna, S. L. Using Bulk Convection in a Microtensiometer to Approach Kinetic-Limited Surfactant Dynamics at Fluid-Fluid Interfaces. *J. Colloid Interface Sci.* **2012**, *372*, 183–191.

(44) Binks, B. P. Particles as Surfactants—Similarities and Differences. *Curr. Opin. Colloid Interface Sci.* **2002**, *7*, 21–41.

(45) Perriman, A. W.; McGillivray, D. J.; White, J. W. Reactions of Isolated Mono-Molecular Protein Films. *Soft Matter* **2008**, *4*, 2192.

(46) Campbell, R. A.; Ang, J. C.; Sebastiani, F.; Tummino, A.; White, J. W. Spread Films of Human Serum Albumin at the Air-Water Interface: Optimization, Morphology, and Durability. *Langmuir* **2015**, *31*, 13535–13542.

(47) Fang, J.; Joos, P. The Dynamic Surface Tension of SDS—dodecanol Mixtures: 1. The Submicellarsystems. *Colloids and Surfaces* **1992**, *65*, 113–120.

(48) Prosser, A. J.; Franses, E. I. Adsorption and Surface Tension of Ionic Surfactants at the Air-Water Interface: Review and Evaluation of Equilibrium Models. *Colloids Surfaces A-Physicochemical Eng. Asp.* **2001**, *178*, 1–40.

(49) Reichert, M. D.; Alvarez, N. J.; Brooks, C. F.; Grillet, A. M.; Mondy, L. A.; Anna, S. L.; Walker, L. M. The Importance of Experimental Design on Measurement of Dynamic Interfacial Tension and Interfacial Rheology in Diffusion-Limited Surfactant Systems. *Colloids Surfaces A Physicochem. Eng. Asp.* **2015**, *467*, 135–142.

(50) Lucassen, J.; Van Den Tempel, M. Dynamic Measurements of Dilational Properties of a Liquid Interface. *Chem. Eng. Sci.* **1972**, *27*, 1283–1291.

(51) Linder, M.; Selber, K.; Nakari-Setälä, T.; Qiao, M.; Kula, M. R.; Penttilä, M. The Hydrophobins HFBI and HFBII from Trichoderma Reesei Showing Efficient Interactions with Nonionic Surfactants in Aqueous Two-Phase Systems. *Biomacromolecules* **2001**, *2*, 511–517.

CHAPTER 7

EFFECT OF SURFACTANT TAIL LENGTH AND IONIC STRENGTH ON THE INTERFACIAL PROPERTIES OF NANOPARTICLE-SURFACTANT COMPLEXES

7.1 INTRODUCTION

Nanoparticles are well known to stabilize foams by adsorbing at air/water interfaces. Particle adsorption lends steric stability to interfaces not provided by classical stabilizers such as surfactants, reducing the rate of bubble coalescence and coarsening.[1–3] The energy required to adsorb a particle at an air/water interface is estimated by $E = \pi R^2 \gamma (1 \pm \cos\theta)^2$, where R is the radius of the particle, γ is the air/water surface tension, and θ is the particle contact angle at the interface.[4] Values of adsorption energy for 10 nm nanoparticles can range from 10^2–10^3 kT, offsetting thermal motion and resulting in particles that adsorb irreversibly to the interface. The adsorption energy can be directly tuned by modifying the contact angle of the particle through the addition of modifiers, such as electrostatically bound surfactants or covalently-grafted thiols.[5–9]

In particular, the combination of negatively charged silica nanoparticles and cationic surfactant has been well studied for its ease of modifying contact angle by adsorbing oppositely charged surfactant on the interface.[10–15] The nanoparticles alone are hydrophilic, with an estimated contact angle of $\theta \sim$ 20-37°.[16,17] Surfactant is added to hydrophobize the nanoparticles and make them surface-active, increasing the contact angle to $\theta \sim$ 60-80° depending on surfactant coverage.[12,18] Without surfactant, the hydrophilic nanoparticles are ineffective stabilizing agents, but the surfactant-nanoparticle complexes yield extremely stable foams that persist

for months.[13] Understanding the interfacial behavior of the complexes is important for practical formulation design. However, complications arise when characterizing the adsorption of these systems at air/water interfaces. While increasing the surfactant concentration in a dispersion of nanoparticles is an effective way to increase particle hydrophobicity, it has the effect of simultaneously reducing the net charge of the particles.[5,11] At sufficient concentrations, this can lead to destabilization of the bulk suspension; as the electrostatic repulsion that keeps the particles dispersed in solution is reduced, the particles flocculate and sediment.[19] Often the foams with the greatest stability are formed at concentrations that result in bulk flocculation.

The inherently unstable nature of these systems adds difficulty to conventional interfacial characterization methods. Conflicting measurements have been reported on the effect of surfactant-nanoparticle complexes on surface tension. In some cases, the complexes reduce the surface tension below the equivalent concentration of pure surfactant;[13,14,20,21] in others, no synergistic effect is observed.[10,12,22,23] Measurements of the interfacial mechanics also vary; Yazhgur *et al*.[24] measure elasticity values that span almost an order of magnitude depending on experimental conditions. The discrepancies can potentially be attributed to bulk flocculation impacting adsorption and interfacial behavior.

In this study, we avoid bulk flocculation as much as possible. Instead of increasing the surfactant concentration to modify particle hydrophobicity, we instead alter the surfactant tail length at a constant, low concentration. By operating at a low surfactant concentration, the nanoparticles retain a negative surface charge,

preventing the rapid bulk destabilization that can cause irreproducible adsorption behavior.

The work presented here aims to characterize the dynamics of adsorption of surfactant-nanoparticle complexes using a combination of surface tension and interfacial rheology measurements. We assess adsorption reversibility and the effect of ionic strength on the interfacial properties by using a controlled bulk solution exchange procedure.

7.2 MATERIALS AND METHODS

The particles used throughout this study are dispersions of Ludox TMA SiO_2 nanoparticles (Sigma, St. Louis, MO), purchased as a 34 wt% dispersion. The surfactants tetradecyltrimethylammonium bromide (C_{14}TAB), hexadecyltrimethylammonium bromide (C_{16}TAB), and octadecyltrimethylammonium bromide (C_{18}TAB) (Sigma, St. Louis, MO) are purchased at 99% purity and are recrystallized twice in ethanol to remove impurities. Sodium chloride (VWR, Batavia, IL) is purchased at 99% purity and is baked at 400°C for 5 hours to remove hydrates and impurities. A 0.5 M NaCl stock solution is prepared with deionized water immediately after baking. Deionized water is prepared by a Barnstead Ultrapure water purification system to 18.2 MΩ·cm resistivity.

All interfacial studies presented here are conducted on 10 wt% SiO_2 dispersions with 0.1 mM C_nTAB added. Using the manufacturer reported particle radius of 11 nm and density of 2.2 g/cm^3, this corresponds to a ratio of

approximately 8 C_nTAB molecules per SiO_2 particle, which is 1-2 orders of magnitude lower than those used in previous studies.[10,12,25] The effect of increased surfactant to nanoparticle ratio on the zeta potential of the C_nTAB/SiO_2 complexes is shown in Figure 7.1(a). Bare Ludox TMA SiO_2 nanoparticles in 10 mM NaCl have a zeta potential of -25 ± 1.8 mV. No increase in zeta potential is observed for concentrations below 0.6 mM C_nTAB added to 1 wt% SiO_2 (443 C_nTAB molecules per particle). Above 0.6 mM C_nTAB, the zeta potential of the complexes increases with added surfactant; at high concentrations, the isoelectric point is passed and the net particle charge becomes positive. Images of the C_{16}TAB/SiO_2 dispersions measured in Figure 7.1(a) are shown in Figure 7.1(b). Despite no measurable increase in zeta potential with the addition of 0.3 mM C_{16}TAB, there is visible sedimentation observed in the bulk suspension. Even dispersions with only 0.1 mM C_{16}TAB added show a slight increase in turbidity, indicating the formation of aggregates that remain suspended in solution. Dispersions with higher C_{16}TAB concentrations exhibit even more sedimentation as the electrostatic stabilization between the nanoparticles is negated by cationic surfactant. Only the lowest tested concentration, 0.01 mM C_{16}TAB with 1 wt% SiO_2, does not result in visible sedimentation or flocculation. We therefore use an equivalent ratio in the interfacial studies presented here: 0.1 mM C_nTAB with 10 wt% SiO_2 in 10 mM NaCl solution. The total complex concentration is increased from 1 wt% to 10 wt% for the interfacial measurements to enhance adsorption at the air/water interface.

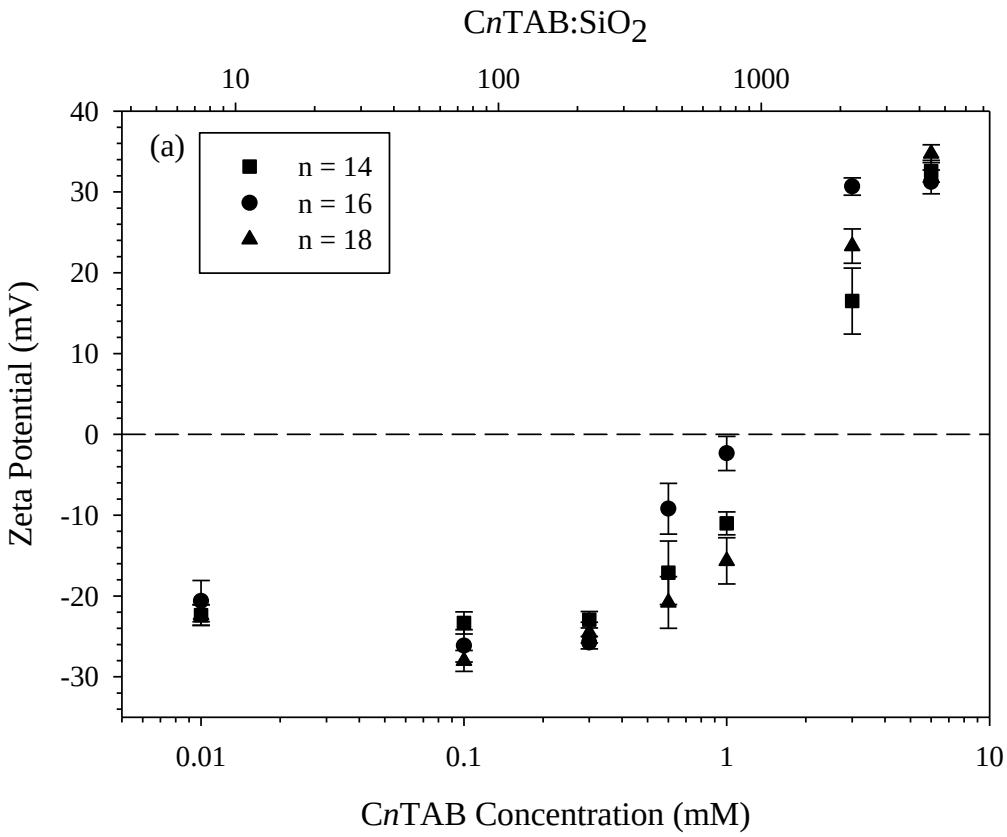

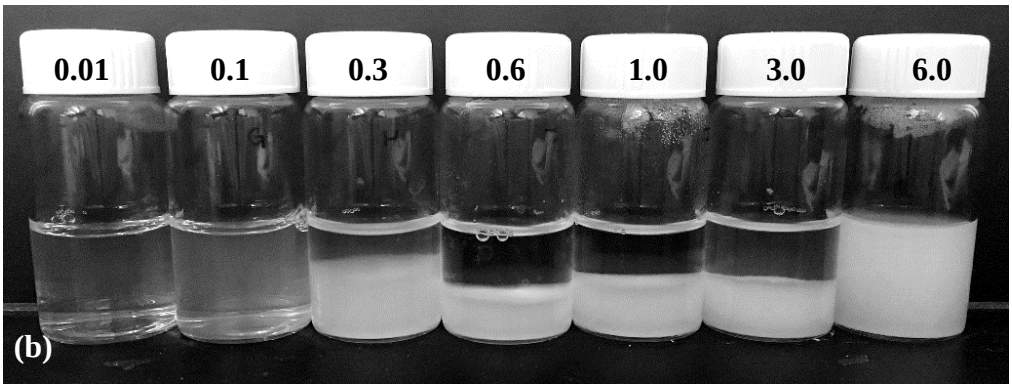

Figure 7.1: (a) Zeta potential as a function of C_nTAB concentration for 1 wt% SiO_2 nanoparticle dispersions in 10 mM NaCl solution. The equivalent surfactant to nanoparticle ratio is shown as the top axis. (b) Stability of 1 wt% C_{16}TAB/SiO_2 dispersions as a function of surfactant concentration. Each vial corresponds to one concentration in (a).

The C_nTAB/SiO_2 samples are prepared via dropwise addition of 0.2 mM C_nTAB solution into a 20 wt% SiO_2 dispersion in a method modified from Ravera *et al*.[26] The dispersion is held in a sonication bath and gently mixed during C_nTAB addition to aid in even surfactant distribution and avoid bulk aggregation. Once combined, the C_nTAB/SiO_2 dispersions are kept in the sonication bath for 30 minutes to reduce flocculation. Dispersions are aged for 24 hours before use to ensure uniform surfactant distribution, and measurements are taken within 48 hours of sample preparation. Dynamic light scattering measurements taken on the samples diluted to 1 wt% immediately prior to measuring indicate no change in average particle size over the 48 hour measurement window.

A microtensiometer is used to measure the surface tension and modulus of the air/water interfaces. The device is described in detail in Chapter 3 and elsewhere.[27–29] Briefly, it consists of a capillary filled with air, placed in a 3D printed thermoplastic cell and submerged in aqueous solution. A spherical cap bubble is formed at the capillary tip. The radius of the bubble is measured on an inverted light microscope, while the pressure jump across the curved interface is measured simultaneously by a pressure transducer in line with the capillary. The instantaneous surface tension, $\gamma(t)$, is determined using the Laplace equation for a spherical cap, $\gamma(t) = (P_1(t) - P_2)R(t)/2$, where P_1 is the pressure in the capillary, P_2 is the hydrostatic pressure of the aqueous solution at the capillary, and R is the radius of the interface. The uncertainty in the calculated surface tension is $\Delta\gamma$ = ±0.5 mN/m from the propagation of random errors in the pressure and radius measurements. Exchange of the bulk solution is achieved via two reservoir ports

connected to a peristaltic pump, as described previously.[30,31] The residence time of the reservoir is approximately 10 s.

The capillaries are purchased from World Precision Instruments, Inc. (Sarasota, FL) and are pulled to a tip radius of 35−38 μm using custom settings on a PMP-100 capillary puller (MicroData Instrument, Inc., South Plainfield, NJ). The interior of the capillaries is acid washed and coated with an arylalkoxysilane XIAMETER OFS-6124 hydrophobic coating from Dow Corning (Midland, MI) according to manufacturer instructions. The hydrophobic coating ensures that the air/water interface is pinned at the tip of the capillary for the duration of the experiment.

The interfacial mechanics are probed in two ways, through small amplitude oscillations to measure the dilatational modulus, and through large amplitude compressions to measure the Gibbs modulus. The dilatational modulus E is defined as $E = \frac{dP^S}{d\ln A}$, where P^S is the surface stress that includes the surface pressure as well as stresses that arise due to the deformation of the interface. A is the interfacial area of the spherical cap, $A = 2\pi R\left(R - \sqrt{R^2 - R_c^2}\right)$, where R_c is the radius of the capillary. The magnitude of the dilatational modulus can be calculated directly from the measured pressure and radius[32] as

$$|E^*| = \frac{b_1}{1-b_1}\left(\frac{R_{eq}}{\Delta R_1}\right)\left(\frac{P_a R_{eq}}{2}\right)\sqrt{\left(\frac{\Delta R_1}{R_{eq}}\right)^2 + 2\left(\frac{\Delta R_1}{R_{eq}}\right)\cos\phi_{R1} + 1},$$

where $b_1 = \sqrt{1-\left(\frac{R_c}{R_{eq}}\right)^2}$ and $\Delta R_1 = R_a\left(\frac{P_{eq}}{P_a}\right)$. P_{eq} is the equilibrium pressure, R_{eq} is the

equilibrium radius, P_a is the amplitude of the pressure oscillations, R_a is the amplitude of the radial oscillations, and ϕ_{R1} is the phase angle of the radial oscillations. Small amplitude oscillations are ensured by verifying that the amplitude of any higher harmonics present in the data are less than 10% of the amplitude of the primary harmonic.

The Gibbs modulus is defined as $E_G = \frac{d\gamma}{d\ln A}$, and is measured by decreasing the pressure behind the interface with a syringe pump (BS-8000, Braintree Scientific, Inc) at a constant rate of 15 Pa/s, corresponding to an average areal compression rate of 1000μm^2/min. The compression rate is five orders of magnitude slower than similar compressions performed on a Langmuir trough.[14] Before selecting the constant compression rate, control experiments were performed at rates of 5, 10, and 20 Pa/s; we observe no effect of compression rate on the results presented here.

7.3 RESULTS

7.3.1 Effect of Surfactant

The adsorption of the C_nTAB /SiO_2 complexes is initially characterized by measuring the dynamic surface tension. Figure 7.2 shows the surface tension as a function of time for three suspensions of 10 wt% SiO_2 nanoparticles in 10 mM NaCl solution with 0.1 mM C_nTAB added, where n = 14, 16, and 18. The surface tension begins at a clean air/water value of $\gamma_0 = 72.5 \pm 0.5$ mN/m, indicated by the horizontal dashed line, and decreases with time as the surfactant-nanoparticle complexes adsorb to the interface. A dispersion of 10 wt% SiO_2 nanoparticles in 10

mM NaCl does not decrease the surface tension, indicating the nanoparticles without added surfactant are not surface active. The overall change in the magnitude of surface tension increases monotonically with the tail length of the surfactant: $C_{14}TAB/SiO_2$ complexes have the smallest effect on surface tension, while $C_{18}TAB/SiO_2$ complexes have the largest effect. All dispersions are generated at a ratio of approximately 8 C_nTAB molecules per SiO_2 particle, which corresponds to just over 1% of the maximum possible adsorption of C_nTAB on SiO_2.[26] We assume total depletion of the C_nTAB to the nanoparticle surface, as verified by Ravera *et al.*[10] for $C_{16}TAB$ adsorption on similar SiO_2 nanoparticles. The decrease in surface tension seen in Figure 7.2 is therefore presumed to be a result of the combined nanoparticle-surfactant complex adsorption, not due to free surfactant adsorption from solution.

The results shown in Figure 7.2 suggest that the surface tension is dictated by the adsorbed surfactant. The average diffusion coefficient of the C_nTAB/SiO_2 complexes does not change with surfactant tail length. Measured using DLS, all three complexes exhibit an average diffusion coefficient of $(1.5 \pm 0.5) \times 10^{-11}$ m^2/s in 10 mM NaCl, equal to the measured diffusion coefficient of bare SiO_2 nanoparticles. The rate of transport to the surface should therefore be independent of surfactant tail length, and the surface tension decrease is attributed to differences in C_nTAB/SiO_2 complex behavior at the interface.

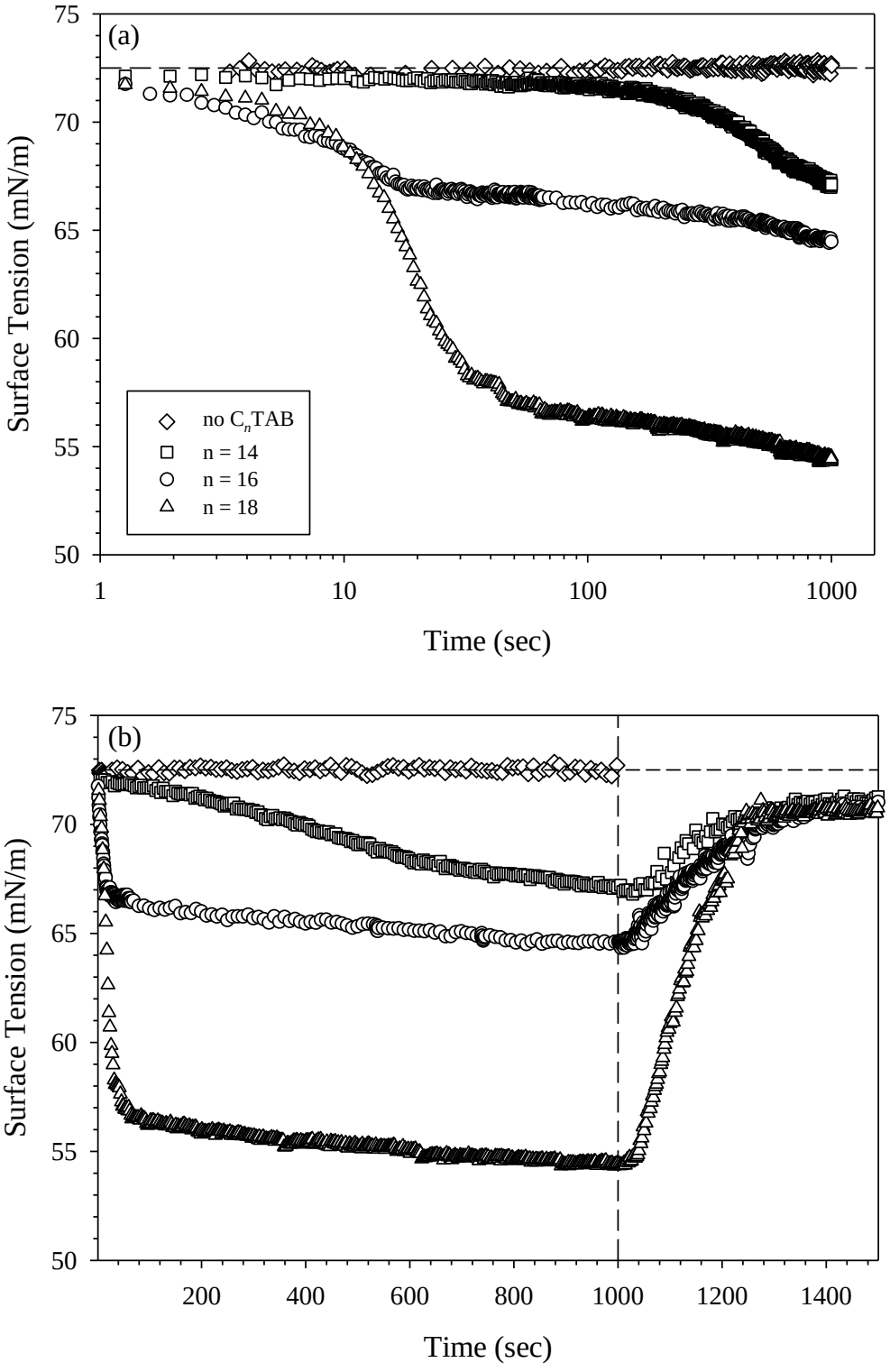

Figure 7.2: (a) Surface tension as a function of time during the adsorption of 10 wt% SiO_2 nanoparticles with and without 0.1 mM C_nTAB in 10 mM NaCl. (b) The nanoparticle dispersion in the reservoir is exchanged with deionized water at t = 1000 s.

The effect of tail length on the surface pressure of the C_nTAB/SiO_2 complexes is consistent with its effect on pure C_nTAB surfactant adsorption at air/water interfaces. The values of surface pressure $\Pi = \gamma - \gamma_0$ after 1000 seconds of adsorption for pure C_nTAB and for the C_nTAB /SiO_2 complexes are shown in Table 7.1. For all three surfactants, the value of the surface pressure due to the complexes is less than the value of the surface pressure of the pure surfactant at a concentration of 0.1 mM, indicating a weaker effect of the complexes. These results contradict those observed by Maestro *et al.*[13] on the same SiO_2 nanoparticle system, who identified an enhanced effect of the particle-surfactant complexes on the surface tension, but confirm several other studies that observed no such enhanced effect.[10–12] We do not expect an additive effect on the surface tension, as the SiO_2 nanoparticles themselves are not surface active and have no effect on the surface tension once adsorbed at the interface.

Table 7.1: Surface pressure values after a fixed time of 1000 s of adsorption (Π_{1000}) and after bulk solution exchange with deionized water (Π_∞) for C_nTAB/SiO_2 complexes and C_nTAB surfactant in 10 mM NaCl.

	Π_{1000} (mN/m)		Π_∞ (mN/m)	
	10 wt% SiO_2	without SiO_2	10 wt% SiO_2	without SiO_2
0.1 mM $C_{14}TAB$	5.5	8.1	1.3	0.3
0.1 mM $C_{16}TAB$	7.9	21.3	1.6	1.3
0.1 mM $C_{18}TAB$	18.1	40.4	1.9	2.0

The dynamics of adsorption can be further characterized using interfacial rheology measurements. Figure 7.3 shows the dilatational modulus and surface pressure as a function of time during the adsorption of 10 wt% SiO_2 with 0.1 mM $C_{16}TAB$ in 10 mM NaCl. The interface is oscillated at a frequency of 1.9 rad/s at

various time intervals to probe the dilatational modulus at different stages of adsorption.[31] Each oscillation appears as a vertical "bar" in the surface pressure data in Figure 7.3. We report the magnitude of the complex modulus extracted from this measurement, |E*|, and refer to this as the dilatational modulus here. The modulus increases slowly with time, reaching a value of 40.2 ± 1.2 mN/m after 10^4 seconds. Similar values of the dilatational modulus are observed for complexes formed with C_{14}TAB (46.4 ± 2.4 mN/m) and C_{18}TAB (39.4 ± 1.3 mN/m) after 10^4 s of adsorption. The small amplitude oscillations during adsorption do not impact the surface pressure or dilatational modulus measurements.

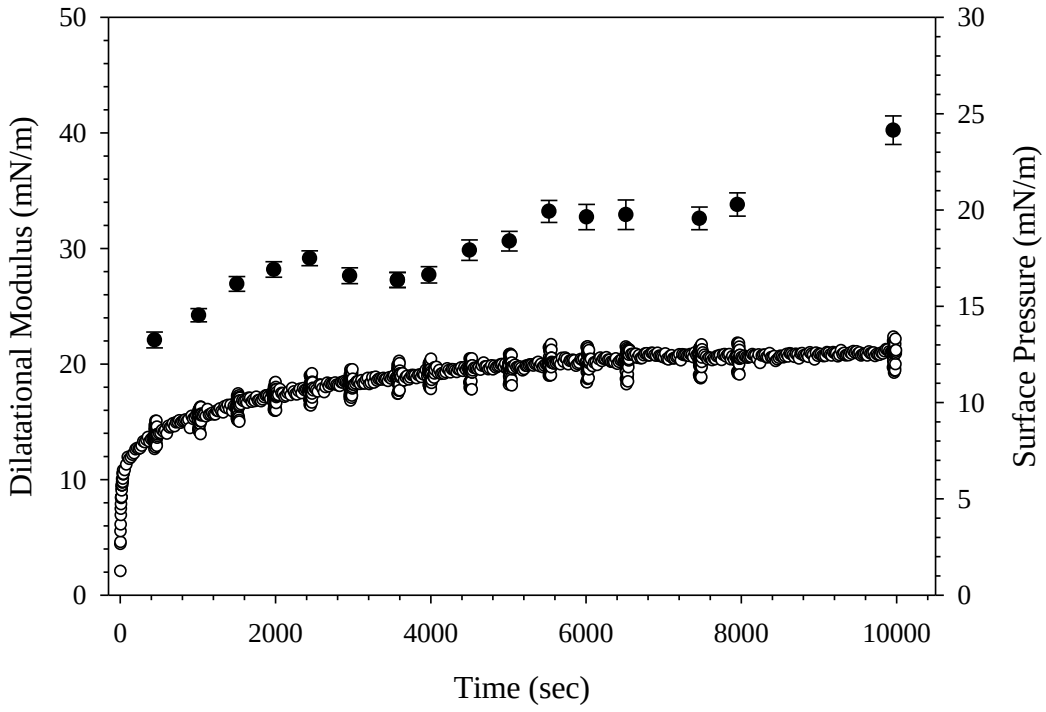

Figure 7.3: Dilatational modulus (●) and surface pressure (○) as a function of time during the adsorption of 10 wt% SiO_2 with 0.1 mM C_{16}TAB in 10 mM NaCl. Oscillations are performed at a constant frequency of 1.9 rad/s.

The values of the dilatational modulus obtained from C_nTAB/SiO_2 complex adsorption are surprisingly low for particle-covered interfaces. Previous studies have reported modulus values more than an order of magnitude larger for systems with higher concentrations of C_nTAB than considered here.[15,24,25] The adsorption of 0.1 mM C_{16}TAB in 10 mM NaCl with no particles present yields a dilatational modulus value of 33.0 ± 1.8 mN/m at an oscillation frequency of 1.9 rad/s, similar to the value obtained for the C_nTAB/SiO_2 complexes. The low modulus values again suggest that the dynamics of adsorption are dominated by the surfactant behavior and that the particles have little to no influence.

To differentiate between surfactant and nanoparticle behavior at the air/water interface, we assess adsorption irreversibly through a rinsing experiment. After allowing the complexes to adsorb for 1000 s, the bulk suspension is exchanged with deionized water, indicated in Figure 7.2(b) by the vertical dashed line. The surface tension increases with time during the rinse for each C_nTAB/SiO_2 mixture, approaching the value of a clean air/water interface (72.5 ± 0.5 mN/m). The increase in surface tension indicates desorption of species from the interface. Assuming a contact angle of 90^o and a manufacturer reported radius of 11 nm, we estimate the adsorption energy of the nanoparticles as $E \sim 1800kT$, suggesting that particle adsorption is irreversible. Therefore, the observed increase in surface tension is likely due solely to surfactant desorption, while the nanoparticles remain pinned at the interface. C_nTAB desorbs from air/water interfaces in the presence of SiO_2 as well as in pure surfactant systems. Table 7.1 shows the rinsed surface pressure values of the C_nTAB/SiO_2 complexes compared with equivalent

concentrations of C_nTAB surfactant alone after 1000 s of adsorption and 500 s of rinsing. The values of surface pressure obtained after rinsing are less than 2 mN/m, both with and without SiO_2 nanoparticles present, suggesting surfactant desorption. We note that while C_{14}TAB exhibits completely reversible adsorption, interfaces exposed to 0.1 mM C_{16}TAB and C_{18}TAB maintain a small but measurable surface pressure after rinsing. This is comparable to the rinsed surface pressure of the C_{16}TAB/SiO_2 and C_{18}TAB/SiO_2 complexes, indicating partially incomplete surfactant desorption for the longer surfactant tail lengths, both with and without nanoparticles present.

From the dynamic surface tension and dilatational modulus measurements shown in Figures 7.2 and 7.3, the C_nTAB/SiO_2 complexes appear to exhibit surfactant-like adsorption behavior, with no evidence of the expected enhanced interfacial mechanics due to the presence of adsorbed nanoparticles. However, the interfaces considered in this study have relatively short ages; similar systems with 1 wt% SiO_2 nanoparticles do not reach maximum particle coverage until surface ages of 10^4 seconds or longer.[24] We have used 10 wt% SiO_2 suspensions to increase the rate of transport to the interface and increase nanoparticle adsorption, but 1000 seconds may still be insufficient to generate fully coated interfaces that exhibit the mechanical properties expected for particle-laden interfaces.

To increase the concentration of nanoparticles adsorbed at the interface, we compress the interface by slowly decreasing the pressure behind the bubble. Assuming the particles are irreversibly adsorbed, decreasing the surface area of the interface decreases the available area per particle. We measure the surface pressure

during the compression to assess the effect of changing surface area on the interfacial mechanics. Figure 7.4(a) shows the surface pressure as a function of surface area during the compression and expansion of a $C_{16}TAB/SiO_2$ complex-coated interface before and after the bulk suspension is exchanged with deionized water. In both cases, the interface starts at a large area and low surface pressure (arrow 1). The rinsed interface has a lower initial surface pressure due to the surfactant desorption observed in Figure 7.2(b). As the interface is compressed, the surface area decreases and the surface pressure increases slightly, until a critical area is reached, below which the surface pressure increases rapidly (arrow 2). After the compression, the interface is expanded slowly to the initial area maintained during species adsorption, A_0 (arrows 3 and 4). The dramatic increase in surface pressure at the critical area of 5300 μm^2 is evidence of particle adsorption at the air/water interface. Purely surfactant-coated interfaces do not exhibit the substantial change in surface pressure over a relatively small change in area, nor do interfaces exposed to nanoparticles without added surfactant. The compression of an interface exposed to 10 wt% SiO_2 nanoparticles in 10 mM NaCl with no C_nTAB added is shown in Figure 7.4(a), where the surface pressure remains below 2 mN/m throughout the compression, suggesting negligible particle adsorption.

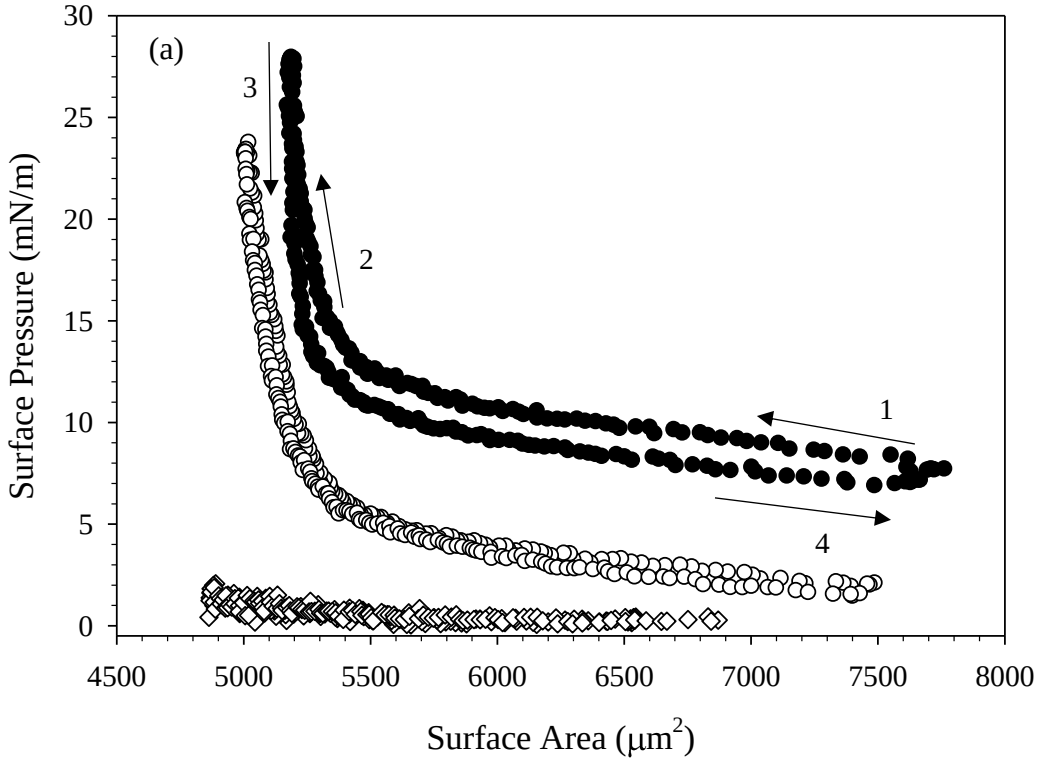
(a)
3
2
1
4
Surface Pressure (mN/m)
Surface Area (μm2)
0
5
10
15
20
25
30
4500
5000
5500
6000
6500
7000
7500
8000

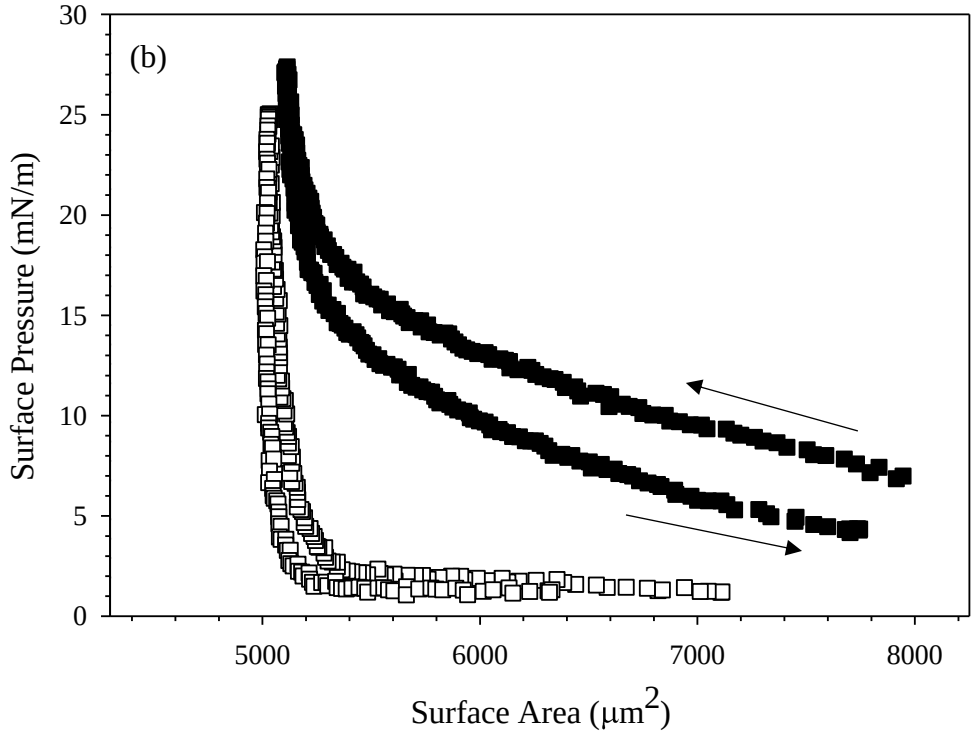
(b)
Surface Pressure (mN/m)
Surface Area (μm2)
0
5
10
15
20
25
30
5000
6000
7000
8000

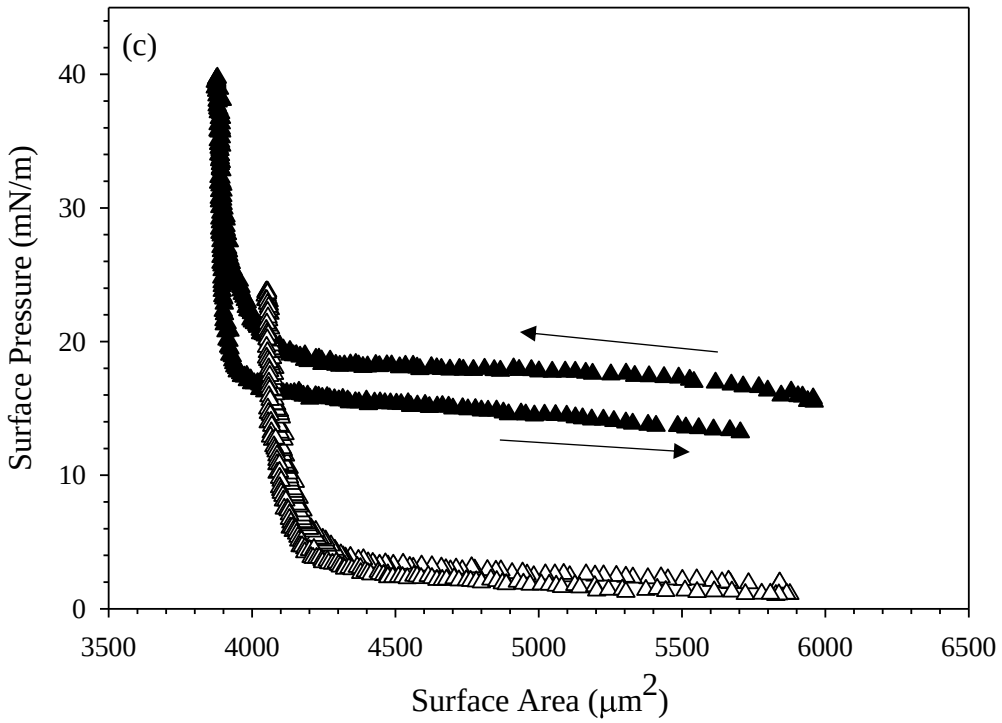

Figure 7.4: Surface pressure as a function of area during the compression and expansion of an interface coated with C_nTAB/SiO_2 complexes before (filled symbols) and after (empty symbols) the bulk suspension is exchanged with deionized water. Arrows indicate the directionality of the compression and expansion, which is consistent for all interfaces. (a) n = 16, (b) n = 14, (c) n = 18. Compression of an interface exposed to SiO_2 nanoparticles with no added surfactant shown in (a) as ◇.

The compression shown in Figure 7.4(a) is performed on an interface exposed to 10% SiO_2 with 0.1 mM C_{16}TAB in 10 mM NaCl before and after rinsing with deionized water. Similar results are obtained for complexes formed with C_{14}TAB and C_{18}TAB, as shown in Figure 7.4(b) and 7.4(c). There is a small (<5 mN/m) hysteresis observed between the compression and expansion of the interface exposed to the bulk C_nTAB/SiO_2 complexes, but no hysteresis is observed for the rinsed interfaces, indicating that complexes do not desorb due to the compression, nor do they interact strongly as a function of surface concentration. The small

hysteresis observed before rinsing is likely due to the presence of additional surfactant at the interface which desorbs upon rinsing with deionized water.

The area corresponding to the increase in surface pressure is not constant across all experiments shown in Figure 7.4 due to variations in capillary size and initial area. To quantify the effect of particle adsorption on the interfacial mechanics during the compression, the Gibbs modulus is calculated from the data in Figure 7.4 and is plotted as a function of the fractional area change, $\xi = 1 - A / A_0$, in Figure 7.5. The fractional area change is defined to normalize by the different initial areas used across experiments due to variations in capillary size. For all interfaces, the value of the Gibbs modulus is < 50 mN/m until a critical area change of about 32% is reached, above which the modulus increases much more rapidly. The modulus reaches values approaching 1000 mN/m, characteristic of particle adsorption and consistent with previous measured values reported for similar systems.[14,24]

The increase in modulus is attributed to the interparticle interactions on the surface. Once the nanoparticles reach a sufficiently high concentration, the hard sphere interactions between the particles prevent further compression. The critical area change required for the increase in Gibbs modulus is constant before and after bulk solution exchange, indicating that the nanoparticles remain irreversibly adsorbed despite rinsing. If the number of particles on the interface remains fixed, then the fractional decrease in area is equivalent to the ratio of surface concentrations, $\xi = 1 - \frac{A}{A_0} = 1 - \frac{\phi_0}{\phi}$, where ϕ is the fractional particle coverage on

the surface. $\phi = NA_P / A$, where N is the number of adsorbed nanoparticles and A_P is the cross-sectional area of a single nanoparticle.

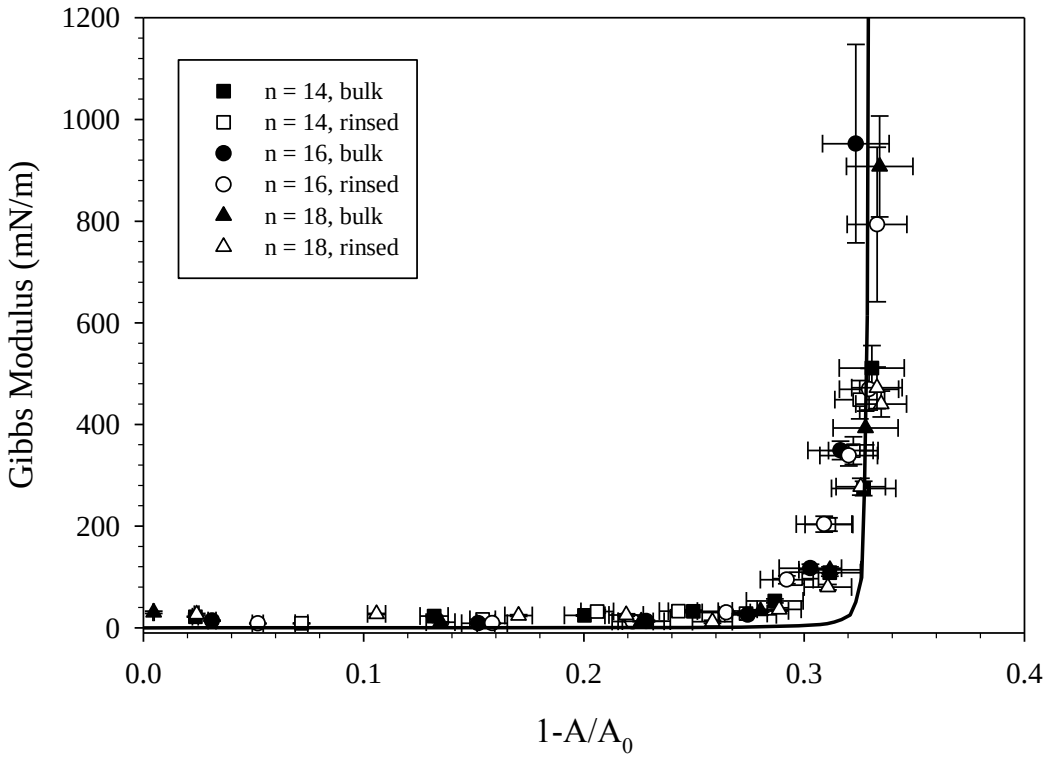

Figure 7.5: Gibbs modulus as a function of fractional area change resulting from the compression of interfaces exposed to C_nTAB/SiO_2 complexes for 1000 s. Open symbols show compressions performed with nanoparticles present in the reservoir, empty symbols show compressions performed after bulk dispersion exchange with deionized water. Solid line is a best fit to equation (7.1).

From the results shown in Figures 7.4 and 7.5, it is clear that surface tension is an insufficient measure of the complex adsorption of surfactant-nanoparticle complexes. The values of the surface pressure in Table 7.1 for the C_nTAB/SiO_2 systems span nearly 20 mN/m, yet the compressions for each surfactant system all yield an increase in Gibbs modulus at a similar fractional area change of about 32%. This result suggests that the particle coverage established at a fixed time point of

1000 seconds of adsorption is approximately constant, independent of surface tension and surfactant tail length. This result is surprising, given the substantial differences in the surface tension for the three surfactant systems. However, the systems measured here contain only a small amount of C_nTAB per SiO_2 particle. The average C_nTAB coverage is less than 8 molecules per particle, whereas previous studies have used ratios 1-2 orders of magnitude larger to achieve adsorption of the complexes.[10,12,25] At this low surfactant to nanoparticle ratio, the compression results suggest that the surfactant tail lengths do not change the effective adsorption of the nanoparticles at the air/water interface. This further supports the hypothesis that the surfactant alone is responsible for the changing surface tension, while the nanoparticles only contribute to the mechanical properties of the interface.

To interpret the response to a large amplitude compression in Figure 7.5, we choose a simple constitutive equation for the interface. The modulus as a function of particle coverage can be modeled by the Volmer equation of state, which assumes non-interacting hard spheres on an interface, as

$$E_G = -\Gamma \frac{d\Pi}{d\Gamma} = \frac{kT\phi\phi_C^2}{A_P(\phi_C - \phi)^2}, \tag{7.1}$$

where ϕ_c is the maximum particle coverage, k is the Boltzmann constant, and T is the temperature. For a particle radius of 11 nm and a contact angle of 90 degrees, A_p = 380 nm^2. This is the maximum possible cross-sectional area of a particle adsorbed at an interface, and allows for a conservative estimate of particle coverage. The Gibbs modulus predicted by the Volmer equation is shown as the solid line in Figure 7.5, using A_p = 380 nm^2 and ϕ_c = 0.86, the random close packing

limit in two dimensions. Previous studies have shown that the maximum coverage corresponds to surface buckling and a change in the slope of the surface pressure isotherm occurring at a particle coverage of about $\phi \sim 0.86$.[13] The Volmer model predicts a sharp increase in Gibbs modulus at a critical coverage due to hard-sphere interactions between the particles on the interface at ϕ_c; however, it under-predicts the measured Gibbs modulus immediately below the critical coverage value. This is attributed to the non-ideal nature of the nanoparticle system: polydispersity and long-range interactions have the potential to impact the modulus before the hard-sphere interactions become significant.

The Gibbs modulus shown in Figure 7.5 is a thermodynamic quantity, characterizing the sensitivity of the surface pressure to changes in surface concentration. The dilatational modulus can contain contributions from the Gibbs modulus, as well as other intrinsic extra stresses. A comparison of the Gibbs modulus (obtained from a large amplitude, slow compression) and the dilatational modulus (obtained from small amplitude oscillations) is shown in Figure 7.6 for the compression of an interface exposed to $C_{16}TAB/SiO_2$ complexes after bulk dispersion exchange with deionized water. At five points during the compression of the rinsed interface, the compression was paused and the pressure was oscillated at a frequency of 1.9 rad/s to measure the dilatational modulus as a function of fractional area change. The values of the Gibbs modulus and dilatational modulus as a function of fractional area change are equivalent, indicating no extra stresses are present. The measured dilatational modulus is therefore solely due to changes in the surface pressure due to changing the surface concentration.

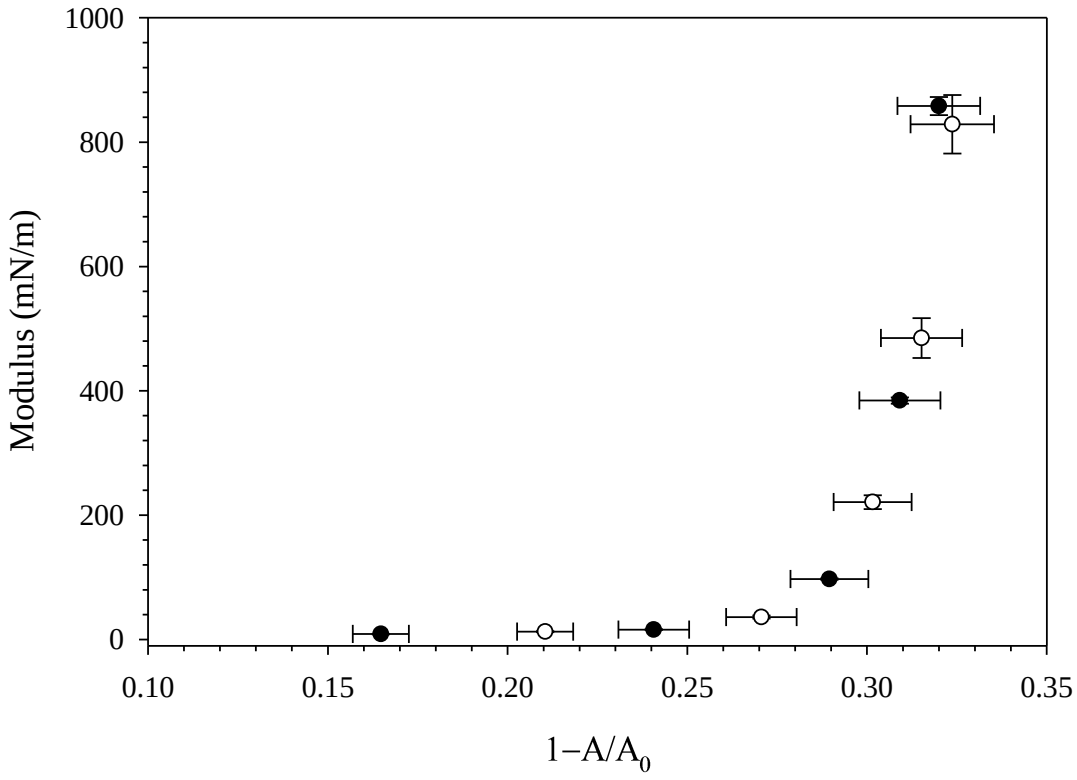

Figure 7.6: Gibbs modulus (○) and dilatational modulus (●) as a function of fractional area change during the compression of an interface coated with $C_{16}TAB/SiO_2$ complexes exposed to deionized water.

The Gibbs modulus and dilatational modulus measurements made during the compression reach values that approach 1000 mN/m as expected for particle-laden interfaces, and both measurements exhibit a critical fractional area change of 32%. The values of the dilatational modulus obtained during compression are over an order of magnitude larger than those obtained during free-adsorption of the C_nTAB/SiO_2 complexes (as seen in Figure 7.3), highlighting the effect of particle concentration on the interfacial mechanics.

7.3.2 Effect of Ionic Strength

The data presented thus far was obtained for suspensions formulated in 10 mM NaCl solution. The ionic strength was chosen to enhance C_nTAB adsorption on the SiO_2 nanoparticles, as well as to increase adsorption at the air/water interface. Figure 7.7(a) shows the surface tension as a function of time for 10 wt% SiO_2 with 0.1 mM C_{16}TAB in 1 mM NaCl and 10 mM NaCl. After 1000 s adsorption, the suspension in 10 mM NaCl reaches a lower surface tension than the suspension in 1 mM NaCl, indicating more efficient C_{16}TAB adsorption. Upon bulk suspension exchange with deionized water, both systems return to similar surface tensions near the clean air/water value. Figure 7.7(b) shows the surface pressure as a function of surface area during the compression and expansion of the rinsed interfaces from Figure 7.7(a). The surface begins at a large area and low surface pressure; upon compression, the surface area decreases and the surface pressure increases. The C_{16}TAB/SiO_2 complexes in 10 mM NaCl exhibit a sharp increase in surface pressure at a critical surface area, but the C_{16}TAB/SiO_2 complexes do not adsorb at high enough concentrations in 1 mM NaCl to significantly increase the surface pressure upon compression. Increasing the bulk suspension ionic strength to 10 mM helps to screen the electrostatic repulsion between the nanoparticles, increasing adsorption at the air/water interface.

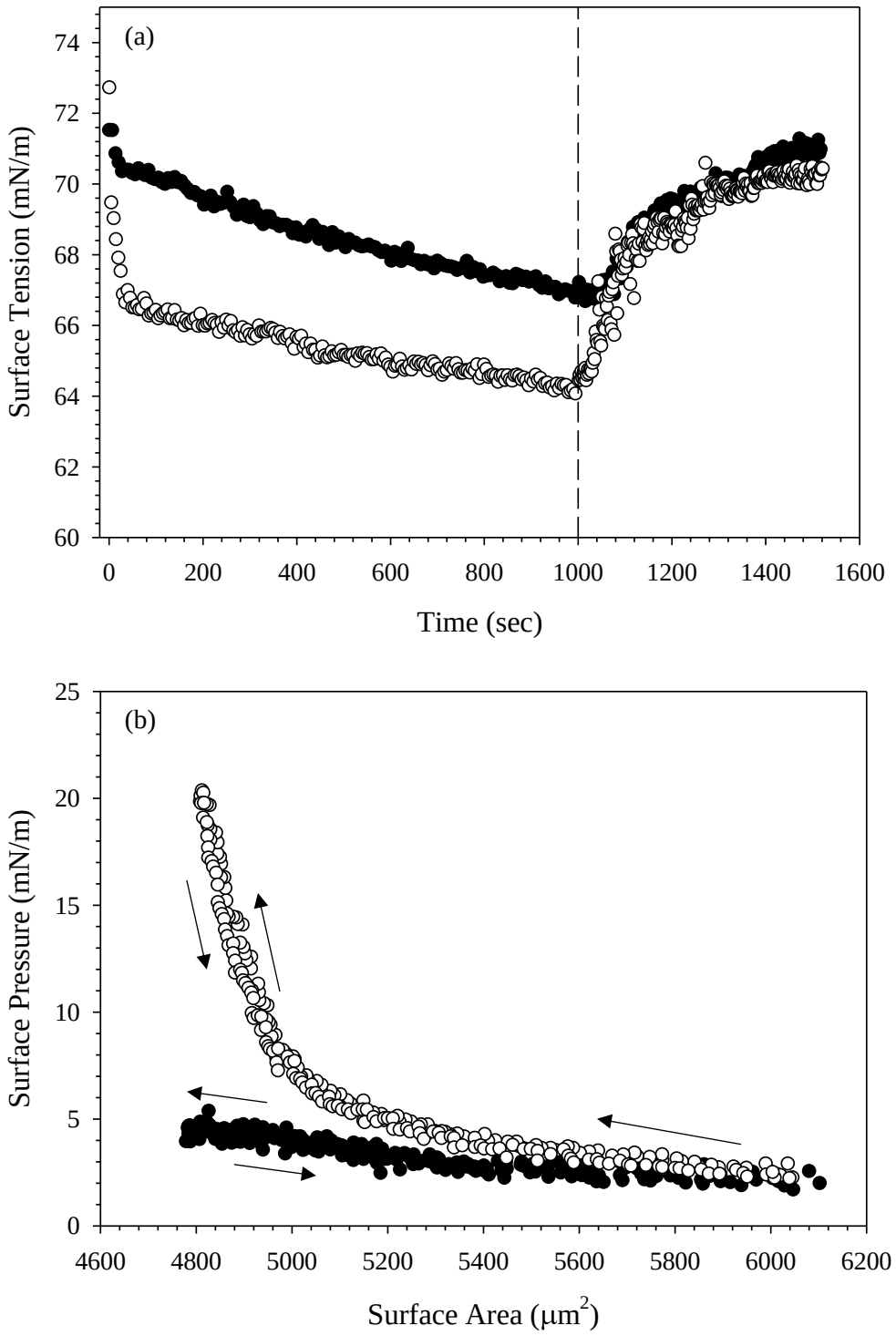

Figure 7.7: (a) Surface tension as a function of time during the adsorption of 10 wt% SiO_2 with 0.1 mM C_{16}TAB in 1mM NaCl (●) and 10 mM NaCl (○). Bulk dispersion is exchanged with deionized water at 1000s. (b): Surface pressure as a function of surface area during the compression of the interfaces from (a) after the rinse with deionized water, at t = 1500 s. Arrows indicate the directionality of the compression and expansion.

To further increase adsorption of nanoparticle complexes to the air/water interface, the ionic strength of the bulk suspension could be increased above 10 mM. However, additional increases in ionic strength lead to bulk destabilization.[19] As the electrostatic repulsion between nanoparticles is reduced with added salt, the nanoparticles flocculate and fall out of solution. To avoid destabilization while still probing the effect of ionic strength on the mechanics of particle-coated interfaces, a sequential rinsing procedure can be utilized. Used previously to characterize multi-species adsorption,[30,31] sequential exchange of the reservoir enables control over bulk conditions without inducing undesired bulk flocculation. In this case, C_{16}TAB/SiO_2 complexes formulated in 10 mM NaCl are allowed to adsorb at the air/water interface for 1000 s, then the bulk suspension is exchanged with deionized water, as seen in Figure 7.2. The air/water interface is therefore coated with irreversibly-adsorbed SiO_2 nanoparticles with no species present in the reservoir. A compression is performed to quantify nanoparticle adsorption. The deionized water in the reservoir is then replaced with 100 mM NaCl, and the compression is repeated.

Figure 7.8(a) shows the surface pressure as a function of surface area of a complex-coated interface with either deionized water in the reservoir or with 100 mM NaCl. While the interface exposed to deionized water exhibits no hysteresis between compression and expansion, when the same interface is compressed in 100 mM NaCl, a significant hysteresis is observed, and the increase in surface pressure shifts to a larger critical area. Figure 7.8(b) shows the Gibbs modulus as a function of fractional area change for the compression shown in Figure 7.8(a). The

compression of the interface when exposed to deionized water returns a critical fractional area change of about 32% as expected. Compression of the interface exposed to 100 mM NaCl exhibits a much lower critical fractional area change of only 21%. Since the compressions are performed on the same interface, the particle coverage is fixed, and the change in critical fractional area is attributed to a change in particle packing structure at the surface. To estimate the change in particle packing, we calculate the change in particle area due to the decrease in Debye length. At adsorption conditions (10 mM NaCl), κ^{-1} = 3 nm. In 100 mM NaCl, the Debye length is reduced to a value of κ^{-1} = 1 nm. The effective area per particle on the interface is reduced by 26%, from 615 nm^2 to 453 nm^2 for a particle where R = 11 nm and $\theta = 90^o$. If particles were able to form a random close packed structure in 100 mM NaCl, the predicted fractional area change needed to increase the modulus would increase to over 50% due to the smaller effective particle area on the surface. Instead of requiring a larger change in area, however, the actual critical area change in 100 mM NaCl shifts to the lower value of 21%, which suggests that the particles are not forming a random close packed structure at high ionic strength. The effective critical particle fraction fit by the Volmer model is $\phi_c \sim 0.74$ in 100 mM NaCl instead of $\phi_c = 0.86$ in deionized water, further suggesting a less closely packed layer.

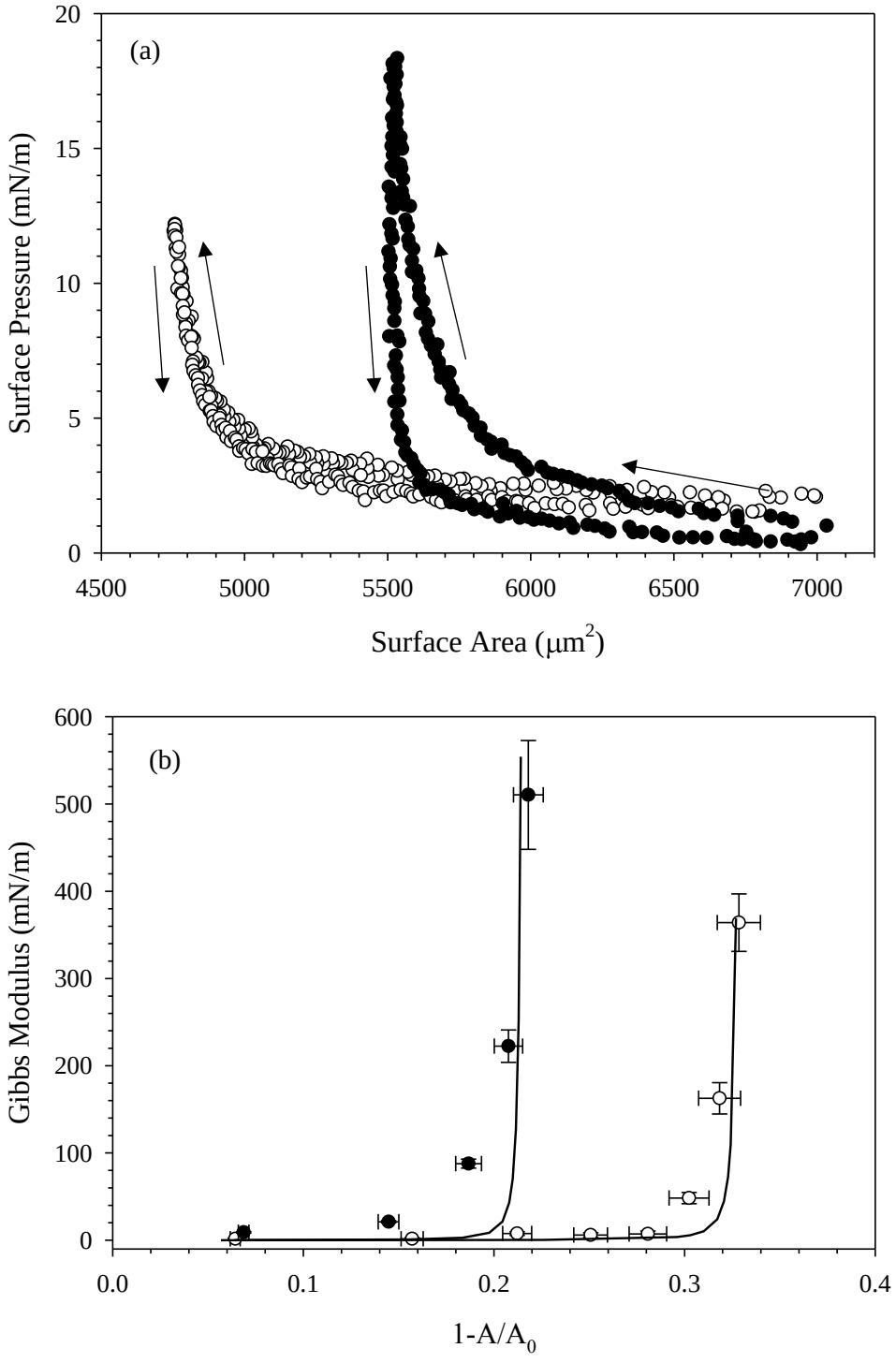

Figure 7.8: (a) Surface pressure as a function of surface area during the compression and expansion of a $C_{16}TAB/SiO_2$ coated interface after bulk exchange with deionized water (○) and subsequent exchange with 100 mM NaCl (●). Arrows indicate directionality for each compression/expansion. (b) Gibbs modulus as a function of fractional area change during the compression. Solid lines are fits to equation (7.1).

The effect of ionic strength on particle structure has been studied optically for larger particles. At low ionic strengths, charged SiO_2 particles form ordered arrays at the air/water interface; at higher ionic strengths, the particles aggregate on the interface, eventually forming percolated networks.[33,34] We hypothesize that similar behavior is occurring with the SiO_2 nanoparticles. Increasing the ionic strength screens the electrostatic repulsion between particles on the interface, inducing flocculation and the formation of a loosely packed network of aggregated particles. The formation of this network results in an increase in Gibbs modulus at lower fractional coverage than needed for non-interacting spheres, which can be compressed to a much larger particle fraction.

To identify the critical salt concentration needed for the formation of a percolated network, the experiment described in Figure 7.8 is repeated for multiple lower salt concentrations. For each concentration, an interface is exposed to 10 wt% SiO_2 nanoparticles with 0.1 mM C_{16}TAB in 10 mM NaCl solution for 1000 s before the bulk dispersion is exchanged with deionized water. The reservoir is then filled with either 1 mM, 10 mM, or 30 mM NaCl and the interface is compressed. The surface pressure as a function of surface area for each concentration is shown in Figure 7.9. The addition of 1 mM and 10 mM NaCl does not shift the critical surface area, but the addition of 30 mM NaCl changes the shape of the compression curve and exhibits slight hysteresis upon expansion. The ability of 30 mM NaCl solution to alter the critical surface area during the compression is highly sensitive to experimental conditions, including the length of time the interface is exposed to the

salt solution, suggesting the formation of the percolated network is stochastic and rate dependent.

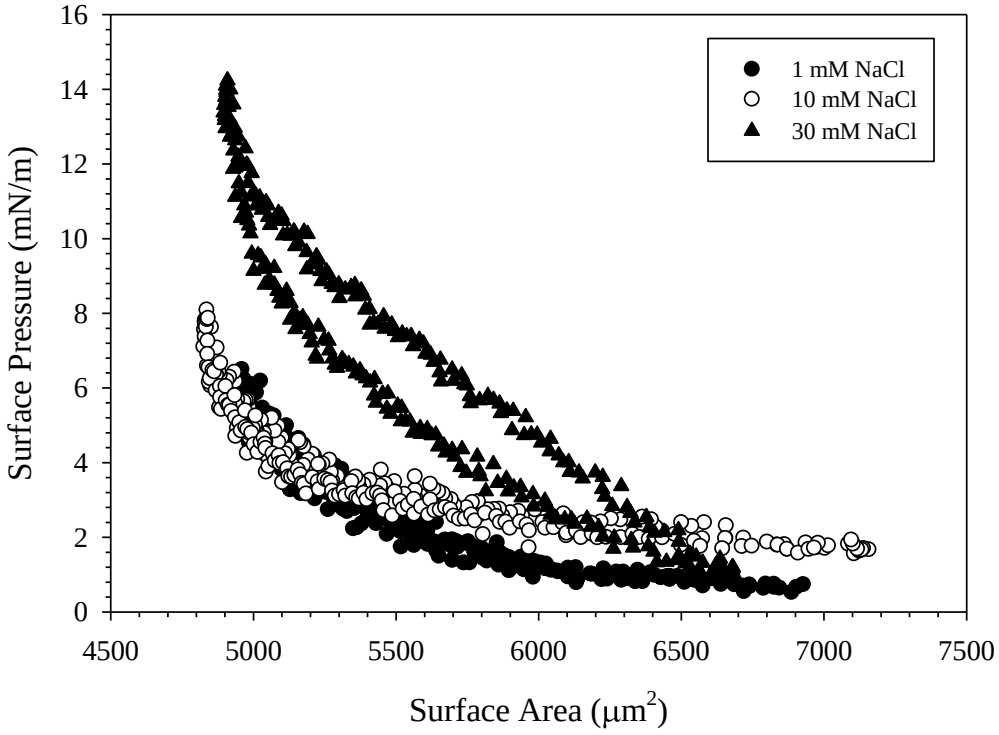

Figure 7.9: Surface pressure as a function of surface area during the compression and expansion a $C_{16}TAB/SiO_2$ coated interface after bulk exchange with deionized water and subsequent exchange with NaCl solution.

The different nature of interparticle interactions at high ionic strength is further illustrated through multiple compression cycles. Figure 7.10 shows the surface pressure as a function of surface area for multiple compression/expansion cycles of a particle-coated interface in deionized water (Figure 7.10(a)) compared to 100 mM NaCl (Figure 7.10(b)). In deionized water, each consecutive compression/expansion cycle traces the same surface pressure-surface area curve, indicating no particle desorption or change in interparticle interactions. In the presence of 100 mM NaCl, however, each subsequent compression shifts the critical area to larger areas.

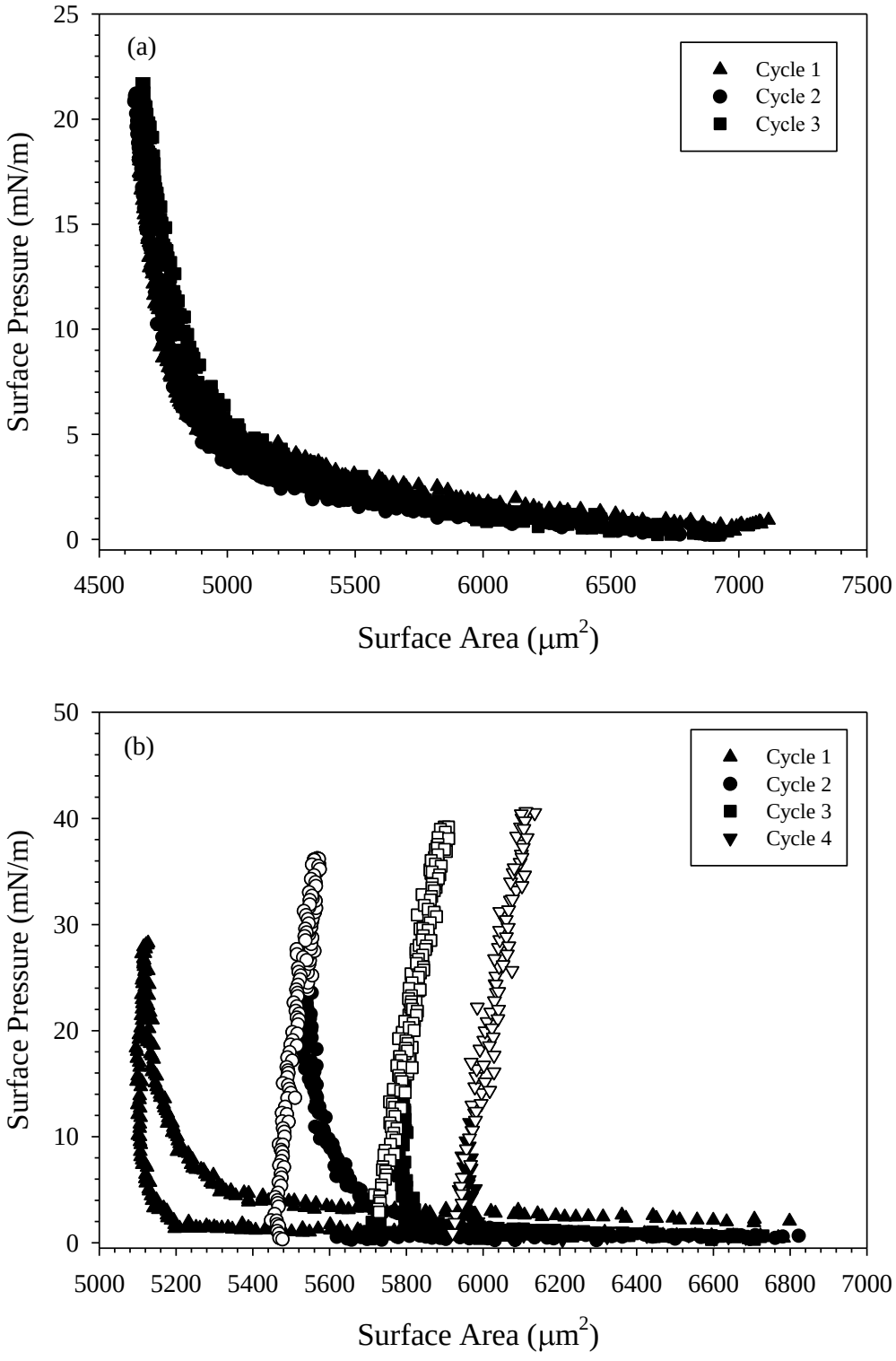

Figure 7.10: Surface pressure as a function of surface area for multiple compression-expansion cycles of a $C_{16}TAB/SiO_2$-coated interface after (a) bulk dispersion exchange with deionized water and (b) 100 mM NaCl solution. Empty symbols indicate distortion of a fully rigid interface.

Further, during the second compression in 100 mM NaCl the interface becomes fully incompressible: the surface area no longer responds to the imposed pressure decrease. Instead, attempts to further compress the interface result in a distortion of the spherical cap at the tip of the capillary, seen in Figure 7.11. This corresponds to a misfitting of the radius, which assumes a spherical cap geometry, and the surface area is overpredicted, shifting the shape of the compression curves in Figure 7.10(b). Once the interface rigidifies, the interface is no longer fluid and the Laplace equation can no longer be used to calculate a surface pressure. Data obtained after the distortion of the interface is plotted in Figure 7.10(b) as empty symbols.

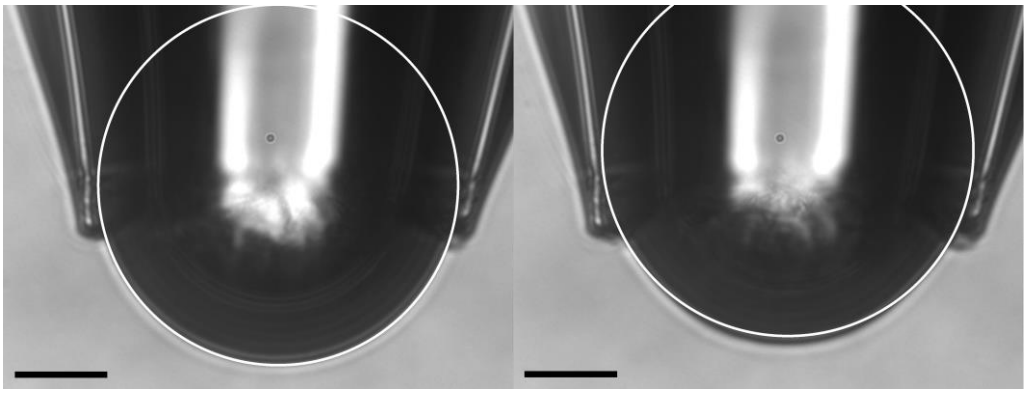

Figure 7.11: Left: Image of the expanded spherical cap before compression. Right: Image of the interface during the fourth compression in Figure 7.10(b), after rigidification. The interface no longer forms a perfect spherical cap at the tip of the capillary, seen in the deviation of the interface from the circular radial fit. Scale bars are 20 μm.

The data from Figure 7.10(b) is used to generate a plot of Gibbs modulus as a function of fractional area change for each subsequent compression in 100 mM NaCl, shown in Figure 7.12. Each compression lowers the value of the critical area change; by the fourth compression, the critical area change is only 12%,

corresponding to an effective critical particle fraction of about $\phi_c \sim 0.67$. The open symbols in Figure 7.12 indicate an estimate of the modulus after the surface has become fully incompressible.

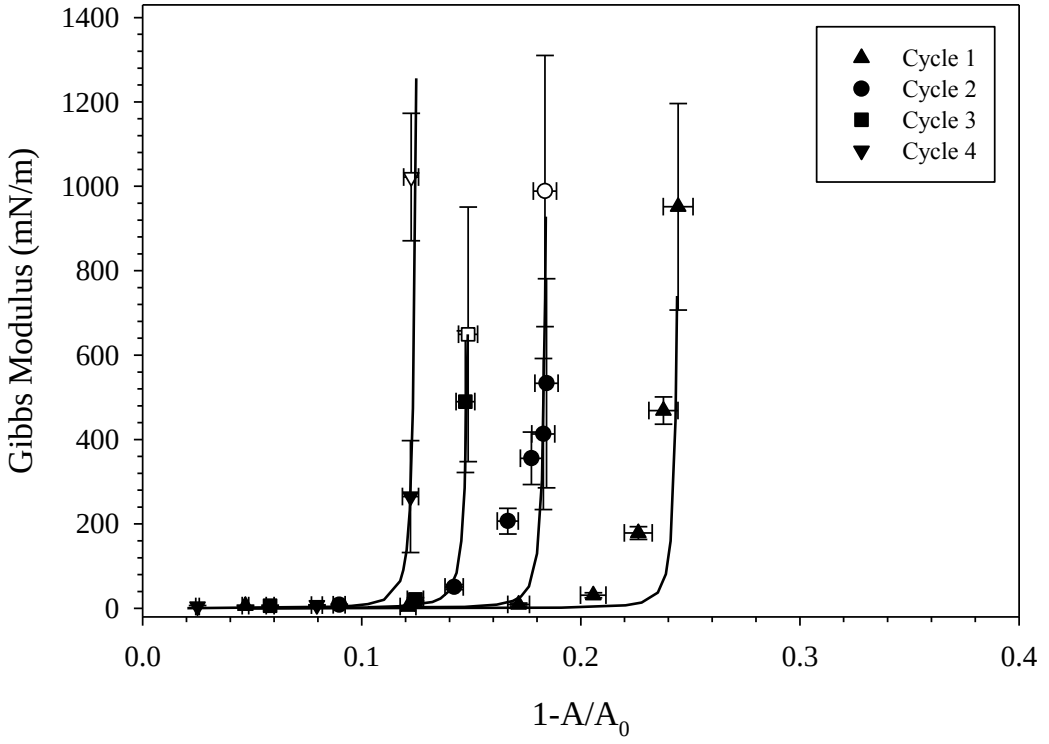

Figure 7.12: Gibbs modulus as a function of fractional area change for the four sequential compressions of a $C_{16}TAB/SiO_2$-coated interface after bulk dispersion exchange with deionized water and 100 mM NaCl shown in Figure 7.9. Solid lines are fits to equation (7.1).

As in Figure 7.8, the data in Figure 7.12 was collected on a single interface with a fixed number of adsorbed particles. Therefore, the shift in critical fractional area change is entirely due to the change in interparticle interactions in the presence of salt. We hypothesize that repeated compressions at high ionic strength induce increasing amounts of flocculation on the surface, forming larger space-filling aggregates with each compression. The flocculation events are irreversible; once

formed, the particle aggregates remain associated. Attempting to compress the interface beyond the incompressible limit results in a distortion of the surface until the surface buckles and collapses.

7.4 DISCUSSION

The results presented above were collected on interfaces aged for 1000 s in the presence of the C_nTAB/SiO_2 dispersions, resulting in a constant particle fraction on the interface for all three systems. However, the systems are not at equilibrium after only 1000 s of adsorption. The surface tension continues to decrease slowly with time beyond 10^4 s, suggesting that additional adsorption or surface reorientation may be occuring. The self-assembly of adsorbed particles on a surface can give rise to local and quasi-long range order, impacting the adsorption rate at high particle coverages;[35] rearrangement on the surface is a function of the strength of interparticle interactions.[36] Long-time adsorption kinetics measured by ellipsometry by Yazhgur *et al.*[24] indicate that steady state is not obtained for greater than 20 x 10^4 s for some C_{16}TAB/SiO_2 systems. Controlling the age of the interface prior to compression therefore offers an additional method to control surface coverage.

Figure 7.13 shows the Gibbs modulus as a function of fractional area change for the compression of six distinct interfaces, where each compression was performed at a different time during the adsorption of C_{16}TAB/SiO_2 complexes, from 250 s up to 10^4 s. The critical fractional area change decreases with interfacial age, consistent with the hypothesis that the degree of adsorption increases with

interfacial age. Compressing after only 250 s results in no measureable increase in the Gibbs modulus, while compressing after 10^4 s results in a critical fractional area change of about 28%. Assuming $\phi_c = 0.86$ at the critical area for each time point, we can estimate the particle coverage ϕ at A_0, the area maintained during the adsorption of complexes. The resulting estimated fractional particle coverage as a function of adsorption time is shown in the Figure 7.13 inset. Particle adsorption increases with adsorption time, approaching a plateau coverage value at long times.

The long-time adsorption kinetics of particles at interfaces has been modeled using random sequential adsorption theory,[37] and has recently been applied to the adsorption of asphaltenes[38] and ethyl cellulose nanoparticles[39] at fluid/fluid interfaces. Particle coverage as a function of time is modeled by

$$\phi(t) = \phi_{\max} - \frac{K}{\pi r^2 N_A C\sqrt{Dt}}, \qquad (7.2)$$

where $K = \phi_{\max}\left(\frac{\phi_{\max}}{4.64k_a}\right)^{\frac{1}{2}}$, k_a is the adsorption rate constant, C is the bulk concentration, and D is the diffusion coefficient of the C_nTAB/SiO_2 complex. The predicted particle coverage from equation (7.2) is plotted as the solid curve in the Figure 7.13 inset where K and ϕ_{max} are fitted parameters. $K = 0.021$ and $\phi_{max} = 0.625$. We note that ϕ_{max} is not equal to ϕ_c as defined earlier, but is instead the maximum particle coverage obtained from free adsorption from bulk solution. The value of ϕ_{max} is less than the value of ϕ_c due to electrostatic repulsion between the particles limiting free adsorption to the surface; the larger value of particle coverage is only obtained through compression of the interface. The value of ϕ_{max} depends

on the assumption of $\phi_c = 0.86$ and $A_p = 380$ nm^2, which are used to estimate the critical particle coverage in Figure 7.13.

The particle coverage scales with $t^{-1/2}$, consistent with long-time diffusion-limited adsorption of other particle systems.[38,39] The estimates of particle coverage in Figure 7.13 do not rely on dynamic surface tension measurements, but rather are obtained by probing the interfacial mechanics, a more reliable measure of particle adsorption behavior.

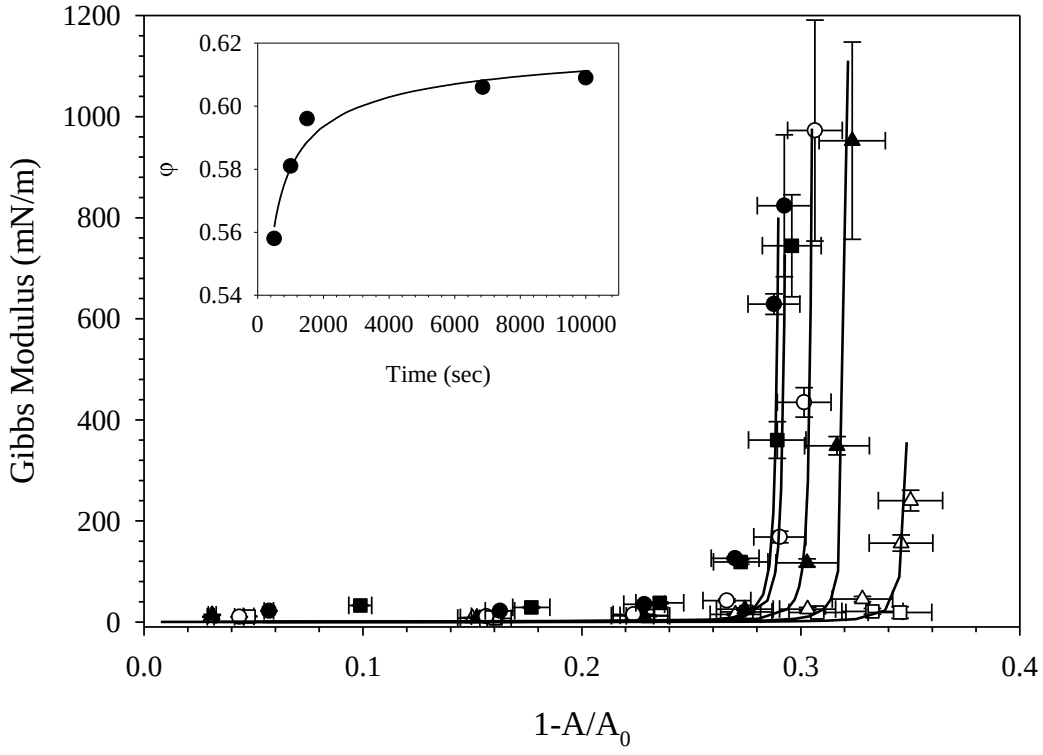

Figure 7.13: Gibbs modulus as a function of fractional area change for compressions of interfaces exposed to 10 wt% SiO_2 with 0.1 mM C_nTAB in 10 mM NaCl for 250 s (□), 500 s (△), 1000 s (▲), 1500 s (○), 7000 s (■), and 10,000 s (●). Volmer model prediction is shown as a solid line for each compression. Inset: particle fraction as a function of adsorption time as estimated from the critical strain. Long time adsorption model shown as the solid curve in inset.

7.5 SUMMARY

We have used surface tension and interfacial rheology measurements to characterize the adsorption of C_nTAB/SiO_2 complexes at air/water interfaces. The nanoparticles alone are not surface active, but the addition of 0.1 mM C_nTAB is sufficient to induce surface adsorption. The surface tension of the complexes depends on surfactant tail length, with the most hydrophobic surfactant affecting the largest reduction in surface tension. However, the particle coverage remains constant for all surfactants, independent of surface tension. We conclude that surface tension is an insufficient measure of surface coverage of the C_nTAB/SiO_2 complexes; interfacial mechanics are necessary to quantify particle adsorption. When the bulk suspension is exchanged with deionized water, the surface tension approaches the value of a clean air/water interface, indicating surfactant desorption upon rinsing. The interfacial mechanics remain unchanged before and after rinsing, confirming the irreversible adsorption of the nanoparticles.

The interfacial mechanics are determined by interparticle interactions, and can be tuned by manipulating the ionic strength of the bulk solution. A nanoparticle-coated interface exposed to deionized water can be compressed and expanded repeatedly with no hysteresis in the interfacial mechanics, with the nanoparticles acting as non-interacting hard spheres. The same interface exposed to 100 mM NaCl, however, exhibits significant hysteresis upon multiple compressions. At high ionic strength, the electrostatic repulsion between the particles is screened by counter ions, allowing the nanoparticles to flocculate on the surface and alter the interfacial mechanics. Repeated compressions of the interface

at high ionic strength ultimately result in the formation of a rigid, incompressible interface at relatively low fractional particle coverages.

This study highlights the importance of processing history on creating interfaces with desired interfacial mechanics. Surfaces with identical particle coverages exhibit substantially different mechanical properties when exposed to environments of different ionic strengths and deformation histories. These results contribute to the understanding of particle behavior at air/water interfaces for the informed formulation of particle stabilized foams.

REFERENCES

(1) Binks, B. P. Particles as Surfactants—Similarities and Differences. *Curr. Opin. Colloid Interface Sci.* **2002**, *7*, 21–41.

(2) Tambe, D. E.; Sharma, M. M. Factors Controlling the Stability of Colloid-Stabilized Emulsions. *JCIS*, 1993, *157*, 244–253.

(3) Stocco, A.; Drenckhan, W.; Rio, E.; Langevin, D.; Binks, B. P. Particle-Stabilised Foams: An Interfacial Study. *Soft Matter* **2009**, *5*, 2215–2222.

(4) Levine, S.; Bowen, B. D.; Partridge, S. J. Stabilization of Emulsions by Fine Particles I. Partitioning of Particles between Continuous Phase and Oil/water Interface. *Colloids and Surfaces* **1989**, *38*, 325–343.

(5) Binks, B. P.; Kirkland, M.; Rodrigues, J. a. Origin of Stabilisation of Aqueous Foams in Nanoparticle–surfactant Mixtures. *Soft Matter* **2008**, *4*, 2373.

(6) Garbin, V.; Jenkins, I.; Sinno, T.; Crocker, J. C.; Stebe, K. J. Interactions and Stress Relaxation in Monolayers of Soft Nanoparticles at Fluid-Fluid Interfaces. *Phys. Rev. Lett.* **2015**, *114*, 1–5.

(7) Lee, Y. L.; Du, Z. C.; Lin, W. X.; Yang, Y. M. Monolayer Behavior of Silica Particles at Air/water Interface: A Comparison between Chemical and Physical Modifications of Surface. *J. Colloid Interface Sci.* **2006**, *296*, 233–241.

(8) Pichot, R.; Spyropoulos, F.; Norton, I. T. Competitive Adsorption of Surfactants and Hydrophilic Silica Particles at the Oil-Water Interface: Interfacial Tension and Contact Angle Studies. *J. Colloid Interface Sci.* **2012**, *377*, 396–405.

(9) Arriaga, L. R.; Drenckhan, W.; Salonen, A.; Rodrigues, J. a.; Íñiguez-Palomares, R.; Rio, E.; Langevin, D. On the Long-Term Stability of Foams Stabilised by Mixtures of Nano-Particles and Oppositely Charged Short Chain Surfactants. *Soft Matter* **2012**, *8*, 11085.

(10) Ravera, F.; Santini, E.; Loglio, G.; Ferrari, M.; Liggieri, L. Effect of Nanoparticles on the Interfacial Properties of Liquid/liquid and Liquid/air Surface Layers. *J. Phys. Chem. B* **2006**, *110*, 19543–19551.

(11) Binks, B. P.; Rodrigues, J. a; Frith, W. J. Synergistic Interaction in Emulsions Stabilized by a Mixture of Silica Nanoparticles and Cationic Surfactant. *Langmuir* **2007**, *23*, 3626–3636.

(12) Maestro, A.; Guzmán, E.; Santini, E.; Ravera, F.; Liggieri, L.; Ortega, F.; Rubio, R. G. Wettability of Silica Nanoparticle-Surfactant Nanocomposite Interfacial Layers. *Soft Matter* **2012**, *8*, 837–843.

(13) Maestro, A.; Rio, E.; Drenckhan, W.; Langevin, D.; Salonen, A.; Anniina, S. Foams Stabilised by Mixtures of Nanoparticles and Oppositely Charged Surfactants: Relationship between Bubble Shrinkage and Foam Coarsening. *Soft Matter* **2014**, *10*, 6975–6983.

(14) Maestro, A.; Deshmukh, O. S.; Mugele, F.; Langevin, D. Interfacial Assembly of Surfactant-Decorated Nanoparticles: On the Rheological Description of a Colloidal 2D Glass. *Langmuir* **2015**, *31*, 6289–6297.

(15) Santini, E.; Krägel, J.; Ravera, F.; Liggieri, L.; Miller, R. Study of the Monolayer Structure and Wettability Properties of Silica Nanoparticles and CTAB Using the Langmuir Trough Technique. *Colloids Surfaces A Physicochem. Eng. Asp.* **2011**, *382*, 186–191.

(16) Safouane, M.; Langevin, D.; Binks, B. P. Effect of Particle Hydrophobicity on the Properties of Silica Particle Layers at the Air-Water Interface. *Langmuir* **2007**, *23*, 11546–11553.

(17) Hunter, T. N.; Jameson, G. J.; Wanless, E. J. Determination of Contact Angles of Nanosized Silica Particles by Multi-Angle Single-Wavelength Ellipsometry. *Aust. J. Chem.* **2007**, *60*, 651–655.

(18) Maestro, A.; Guzmán, E.; Ortega, F.; Rubio, R. G. Contact Angle of Micro- and Nanoparticles at Fluid Interfaces. *Curr. Opin. Colloid Interface Sci.* **2014**, *19*, 355–367.

(19) Metin, C. O.; Lake, L. W.; Miranda, C. R.; Nguyen, Q. P. Stability of Aqueous Silica Nanoparticle Dispersions. *J. Nanoparticle Res.* **2011**, *13*, 839–850.

(20) Lan, Q.; Yang, F.; Zhang, S.; Liu, S.; Xu, J.; Sun, D. Synergistic Effect of Silica Nanoparticle and Cetyltrimethyl Ammonium Bromide on the Stabilization of O/W Emulsions. *Colloids Surfaces A Physicochem. Eng. Asp.* **2007**, *302*, 126–135.

(21) Ma, H.; Luo, M.; Dai, L. L. Influences of Surfactant and Nanoparticle Assembly on Effective Interfacial Tensions. *Phys. Chem. Chem. Phys.* **2008**, *10*, 2207.

(22) Binks, B. P.; Rodrigues, J. A. Enhanced Stabilization of Emulsions due to Surfactant-Induced Nanoparticle Flocculation. *Langmuir* **2007**, *23*, 7436–7439.

(23) Somasundaran, P.; Snell, E. D.; Xu, Q. U. N. Adsorption Behavior of

Alkylarylethoxylated Alcohols on Silica Effect of Ethoxylation The Effect of Ethoxylation of the Nonionic Effect of Alkyl Chainlength The Adsorption Isotherms for Surfactants. **1991**, *144*.

(24) Yazhgur, P. a.; Noskov, B. a.; Liggieri, L.; Lin, S.-Y.; Loglio, G.; Miller, R.; Ravera, F. Dynamic Properties of Mixed Nanoparticle/surfactant Adsorption Layers. *Soft Matter* **2013**, *9*, 3305.

(25) Liggieri, L.; Santini, E.; Guzmán, E.; Maestro, a.; Ravera, F. Wide-Frequency Dilational Rheology Investigation of Mixed Silica nanoparticle–CTAB Interfacial Layers. *Soft Matter* **2011**, *7*, 7699.

(26) Ravera, F.; Ferrari, M.; Liggieri, L.; Loglio, G.; Santini, E.; Zanobini, A. Liquid-Liquid Interfacial Properties of Mixed Nanoparticle-Surfactant Systems. *Colloids Surfaces A Physicochem. Eng. Asp.* **2008**, *323*, 99–108.

(27) Alvarez, N. J.; Walker, L. M.; Anna, S. L. A Microtensiometer to Probe the Effect of Radius of Curvature on Surfactant Transport to a Spherical Interface. *Langmuir* **2010**, *26*, 13310–13319.

(28) Alvarez, N.; Walker, L.; Anna, S. Diffusion-Limited Adsorption to a Spherical Geometry: The Impact of Curvature and Competitive Time Scales. *Phys. Rev. E* **2010**, *82*, 11604.

(29) Reichert, M. D.; Walker, L. M. Interfacial Tension Dynamics, Interfacial Mechanics, and Response to Rapid Dilution of Bulk Surfactant of a Model Oil-Water-Dispersant System. *Langmuir* **2013**, *29*, 1857–1867.

(30) Kirby, S. M.; Anna, S. L.; Walker, L. M. Sequential Adsorption of an Irreversibly Adsorbed Nonionic Surfactant and an Anionic Surfactant at an Oil/Aqueous Interface. *Langmuir* **2015**, *31*, 4063–4071.

(31) Kirby, S. M.; Zhang, X.; Russo, P. S.; Anna, S. L.; Walker, L. M. Formation of a Rigid Hydrophobin Film and Disruption by an Anionic Surfactant at an Air/Water Interface. *Langmuir* **2016**, *32*, 5542–5551.

(32) Kotula, A. P.; Anna, S. L. Regular Perturbation Analysis of Small Amplitude Oscillatory Dilatation of an Interface in a Capillary Pressure Tensiometer. *J. Rheol. (N. Y. N. Y).* **2015**, *59*, 85–117.

(33) Aveyard, R.; Clint, J. H.; Nees, D.; Paunov, V. N. Compression and Structure of Monolayers of Charged Latex Particles at Air/water and Octane/water Interfaces. *Langmuir* **2000**, *16*, 1969–1979.

(34) Williams, D. F.; Berg, J. C. The Aggregation of Colloidal Particles at the Air-Water Interface. *J. Colloid Interface Sci.* **1992**, *152*, 218–229.

(35) Schwenke, K.; Isa, L.; Del Gado, E. Assembly of Nanoparticles at Liquid

Interfaces: Crowding and Ordering. *Langmuir* **2014**, *30*, 3069–3074.

(36) Schwenke, K.; Del Gado, E. Soft Repulsive Interactions, Particle Rearrangements and Size Selection in the Self-Assembly of Nanoparticles at Liquid Interfaces. *Faraday Discuss.* **2015**, *181*, 261.

(37) Adamczyk, Z. Kinetics of Diffusion-Controlled Adsorption of Colloid Particles and Proteins. **2000**, *489*, 477–489.

(38) Pauchard, V.; Rane, J. P.; Zarkar, S.; Couzis, A.; Banerjee, S. Long-Term Adsorption Kinetics of Asphaltenes at the Oil-Water Interface: A Random Sequential Adsorption Perspective. *Langmuir* **2014**, *30*, 8381–8390.

(39) Bizmark, N.; Ioannidis, M. A.; Henneke, D. E. Irreversible Adsorption-Driven Assembly of Nanoparticles at Fluid Interfaces Revealed by a Dynamic Surface Tension Probe. *Langmuir* **2014**, *30*, 710–717.

CHAPTER 8

CONCLUSIONS

Improved characterization of multi-component interfaces is important for practical use of mixed systems for a variety of applications. This work contributes to the understanding of several model systems by generating mixed interfaces under specific, controlled conditions. Manipulating solution properties such as concentration and ionic strength allows for the assessment of interfacial properties in conditions otherwise inaccessible due to bulk interactions or destabilization.

In Chapter 4, the adsorption of the nonionic surfactant Tween 80 and the anionic surfactant AOT are characterized at a squalane/water interface using a sequential adsorption technique. Interfaces are pre-coated with irreversibly adsorbing Tween 80 and exposed to a range of concentrations of AOT. AOT adsorbs to the pre-coated interface, and its adsorption is modeled using a Langmuir isotherm. The presence of Tween 80 on the interface inhibits AOT adsorption: the maximum AOT surface coverage is reduced by up to 50% at an interface with Tween 80 compared to a bare interface. AOT adsorption can be enhanced by increasing the ionic strength of the solution. AOT adsorbs reversibly onto the Tween 80-coated interfaces, with surface pressures returning to zero upon rinsing with deionized water. The Tween 80 remains largely irreversibly adsorbed despite exposure to high concentrations of AOT, highlighting the persistent nature of Tween adsorption at oil/water interfaces.

In Chapter 5, the dynamic and equilibrium adsorption of a rhamnolipid biosurfactant is characterized at air/water and oil/water interfaces. The adsorption

is modeled with a Langmuir isotherm. Adsorption timescales are analyzed using a scaling argument developed by Alvarez *et al.* (2010), and the adsorption is determined to be diffusion limited at both air/water and oil/water interfaces for the concentrations measured. From this, the lower bounds of the kinetic adsorption parameters are estimated.

The rhamnolipids adsorb partially irreversibly at both air/water and oil/water interfaces. Using similar techniques as Chapter 4, the sequential adsorption of rhamnolipid on oil/water interfaces pre-coated with Tween 80 is characterized. Rhamnolipid co-adsorbs to the interfaces with Tween; unlike AOT, however, the maximum surface concentration of rhamnolipids is not inhibited by the presence of Tween 80. When the mixed interfaces are rinsed, the final values of the surface pressure indicate a combination of Tween 80 and rhamnolipid persists on the interface after rinsing.

The adsorption of the globular protein Cerato-ulmin (CU) is measured at the air/water interface in Chapter 6 and at the oil/water interface in the Appendix using a combination of interfacial tension and interfacial rheology measurements. CU adsorption is irreversible, forming a rigid protein film at long exposure times with modulus values greater than 1000 mN/m. Using a combination of small-amplitude oscillations and large-amplitude compressions, we compare the dilatational modulus to the Gibbs modulus at an air/water interface, and model the modulus as a function of surface pressure using the Volmer isotherm.

Once a rigid CU film forms at the air/water interface, the sequential adsorption methodology is used to assess the effect of the addition of SDS on the

film mechanics and surface tension. SDS is able to co-adsorb to the CU film, indicated by a decrease in the surface tension and dilatational modulus as the SDS lubricates the rigid protein film. Upon rinsing with deionized water, SDS appears to desorb from the surface, and the CU film re-solidifies. This phenomenon is concentration dependent; at SDS concentrations near the CMC, the SDS fully displaces the CU from the surface.

The ability to generate a mixed CU-SDS interface that is fully incompressible is to our knowledge only achievable using the sequential adsorption methodology presented here. Parallel adsorption studied via neutron reflectometry performed by Zhang *et al.* (2011) revealed mixed adsorption at the air/water interface, but full solidification of the interface was not achieved. These results highlight the different interfacial behavior that occurs from bulk complex formation as opposed to individual species adsorption.

In Chapter 7, we characterize the adsorption of C_nTAB/SiO_2 complexes at an air/water interface. The surface tension dynamics are a function of surfactant tail length, with the most hydrophobic surfactant resulting in the largest decrease in the surface tension. The particle coverage, however, remains constant for all surfactants and is independent of the measured surface tension, indicating the particles do not contribute significantly to the measured surface tension. When the bulk suspension is exchanged with deionized water, the surface tension approaches a clean air/water surface tension value, suggesting C_nTAB desorption.

Interfacial mechanics are used to characterize nanoparticle adsorption before and after bulk solution exchange. The dilatational modulus increases slowly

with adsorption time, but does not reach the high values observed for the CU system in Chapter 6. To achieve a rigid interface, the surface concentration of the complexes is manually increased through a large-amplitude compression. The compression reveals the presence of a critical particle coverage that corresponds to a large increase in the Gibbs and dilatational modulus. The interfacial mechanics are unchanged before and after bulk solution exchange, confirming the irreversible adsorption of the nanoparticles.

The interactions of the particles on the surface can be tuned by modifying the ionic strength of the subphase. In deionized water, the particles behave as non-interacting hard spheres. Increasing the salt concentration induces particle flocculation on the surface, resulting in the formation of a more loosely packed percolated network. Repeated compressions at high ionic strengths result in additional flocculation to eventually form a rigid, incompressible surface at low fractional particle coverages.

Throughout this work, the microtensiometer platform has enabled control over bulk solution conditions for the study of various mixed systems. By taking advantage of the irreversible adsorption of certain surface-active species, we are able to use a sequential adsorption procedure that avoids bulk interaction and complex formation. The high interfacial curvature enables rapid adsorption dynamics for even dilute systems, and the small reservoir allows for rapid bulk solution exchange (and minimal sample waste). We have presented a combination of dynamic interfacial tension and interfacial mechanics measurements to fully capture the surface behavior of the complex systems.

Overall, this thesis provides novel characterizations of several model surface active systems, revealing unique interfacial properties previously unobserved without use of precise experimental control. We emphasize the roles that processing and solution conditions can have on the interfacial behavior and composition of many systems. The results presented here contribute to the overall understanding of multi-component fluid/fluid interfaces and lend insight to future improved formulation design.

APPENDIX A

CERATO-ULMIN ADSORPTION AT AN OIL/WATER INTERFACE

Characterization of the adsorption of the hydrophobin Cerato-ulmin (CU) at air/water interfaces is presented in Chapter 6, but the behavior of CU at oil/water interfaces is also of interest. The hydrophobin HFBII has been shown to stabilize oil-in-water emulsions for up to several months,[1] and low concentrations of HFBII are able to reverse the wettability of hydrophobic thin films.[2] Potential applications include use in food emulsions,[3,4] as carriers of water-insoluble drug particles,[5,6] and as oil spill dispersants.[7] Despite interest in the use of hydrophobins at oil/water interfaces, relatively few interfacial studies have been performed to quantify their adsorption behavior. Here, we use the methods described in Chapter 6 to characterize CU adsorption at a squalane/water interface.

Figure A.1 shows the surface pressure and dilatational modulus as a function of time for the adsorption of 0.002 mg/mL CU to a squalane/water interface. Data from five experiments is presented, where the interface has been oscillated at various intervals to probe the dilatational modulus during adsorption. Each oscillation corresponds to one point in Figure A.1. For all five runs, the surface pressure and dilatational modulus begin at low values and increase with time as CU adsorbs to the oil/water interface. The variability in the dynamic data across multiple runs is attributed to different effective CU bulk concentrations due to the depletion of CU to the walls and free surface of the microtensiometer reservoir.[8,9]

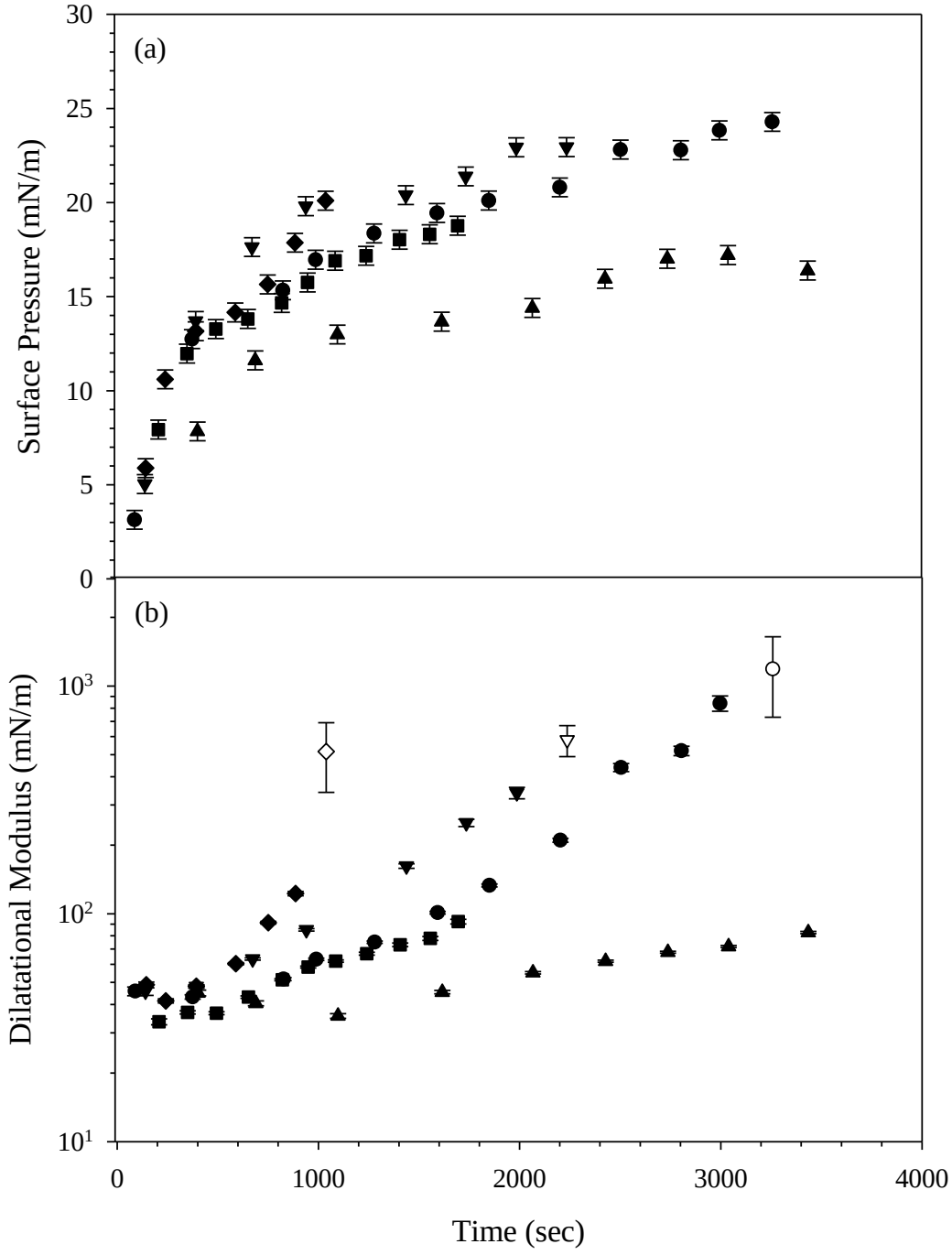

Figure A.1: (a) Surface pressure and (b) dilatational modulus as a function of time for the adsorption of 0.002 mg/mL solution of CU at a squalane/water interface. Different symbols represent five unique runs. Open symbols indicate surfaces that have a dilatational modulus too large to measure with small amplitude oscillations; the plotted values represent the minimum modulus for the surface at that time.

In three of the experiments, the modulus increases to the point where it can no longer be measured, indicating the formation of a rigid hydrophobin film at the oil/water interface. The minimum possible values of the modulus are plotted as open symbols once the interface becomes fully incompressible. The formation of a rigid protein film is also observed for the adsorption of CU at air/water interfaces in Chapter 6.

The data from Figure A.1 is used to generate a parametric plot of the dilatational modulus as a function of the surface pressure, shown in Figure A.2 as filled symbols. The variability between runs observed in Figure A.1 is reduced, and the data appear to collapse to a single curve. The dilatational modulus stays fairly constant at low surface pressures until a surface pressure of 20 mN/m is reached, at which point the dilatational modulus increases rapidly, approaching values of 1000 mN/m. The shape of the oil/water curve in Figure A.2 differs from the curve generated at an air/water interface in Chapter 6 (shown as gray symbols), suggesting a different relationship between the dilatational modulus and surface pressure. For the majority of surface pressures, the magnitude of the dilatational modulus is lower at oil/water interfaces than at air/water interfaces. Similar behavior is observed when comparing the shear modulus of HFBII adsorbed at a hexadecane/water interface versus an air/water interface,[10] and is attributed to differences in protein conformation at the oil/water interface.

The Volmer model successfully predicts the relationship between the dilatational modulus and the surface pressure at an air/water surface in Chapter 6, but does not correspond to the behavior observed at an oil/water interface. None of

the commonly used isotherm models (Langmuir, Frumkin, Volmer, or van der Waals) are able to predict the increase in dilatational modulus observed at high surface pressures at the oil/water interface. Representative curves of the Volmer and Langmuir models are shown in Figure A.2 as solid and dashed lines, respectively, to highlight the differences between the model predictions and observed behavior at the oil/water interface.

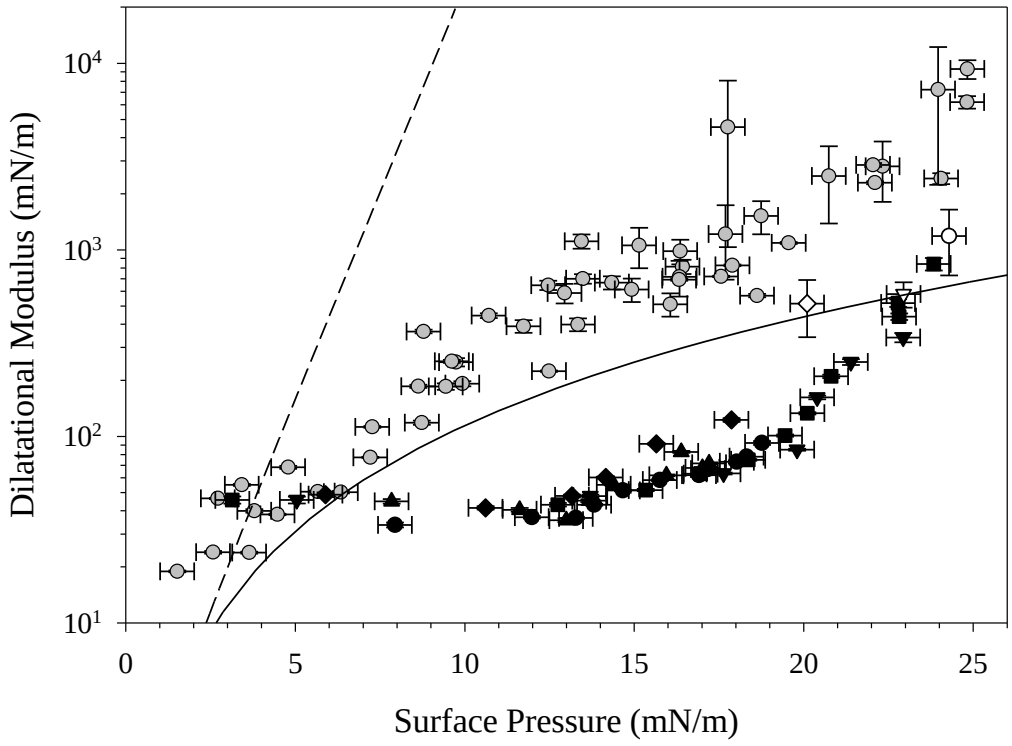

Figure A.2: Dilatational modulus as a function of surface pressure. The data from Figure A.1 is plotted parametrically as filled symbols and is shown to collapse to a single curve, independent of differences in adsorption dynamics. The gray symbols represent data at an air/water interface from Chapter 6. Open symbols represent oil/water interfaces that have a dilatational modulus too large to measure; the plotted values represent the estimated minimum modulus.

The reversibility of CU adsorption at oil/water interfaces is assessed via bulk solution exchange with deionized water. Figure A.3 shows the surface pressure and dilatational modulus of the interface before and after the CU solution in the

reservoir is replaced with deionized water. Points that coincide with the dashed one to one line exhibit no measurable change in surface tension or dilatational modulus, indicating completely irreversible adsorption. Both interfaces that have low CU surface coverage (filled symbols) and those with high CU surface coverage that have formed fully rigid films (open symbols) exhibit irreversible adsorption behavior, consistent with observations of CU at air/water interfaces.

We have shown that CU is able to adsorb at oil/water interfaces and forms irreversibly adsorbed, incompressible protein films at high surface pressures. The formation of rigid films only occurs at long adsorption times and sufficiently large values of the surface pressure; before the film rigidifies, the dilatational modulus is up to an order of magnitude lower at oil/water interfaces than at air/water interfaces. Despite this, CU adsorption at oil/water interfaces still results in modulus values that are significantly larger than those measured for other globular proteins (which are typically below 150 mN/m),[11–13] supporting continued investigation into their use as air/water and oil/water interfacial stabilizers.

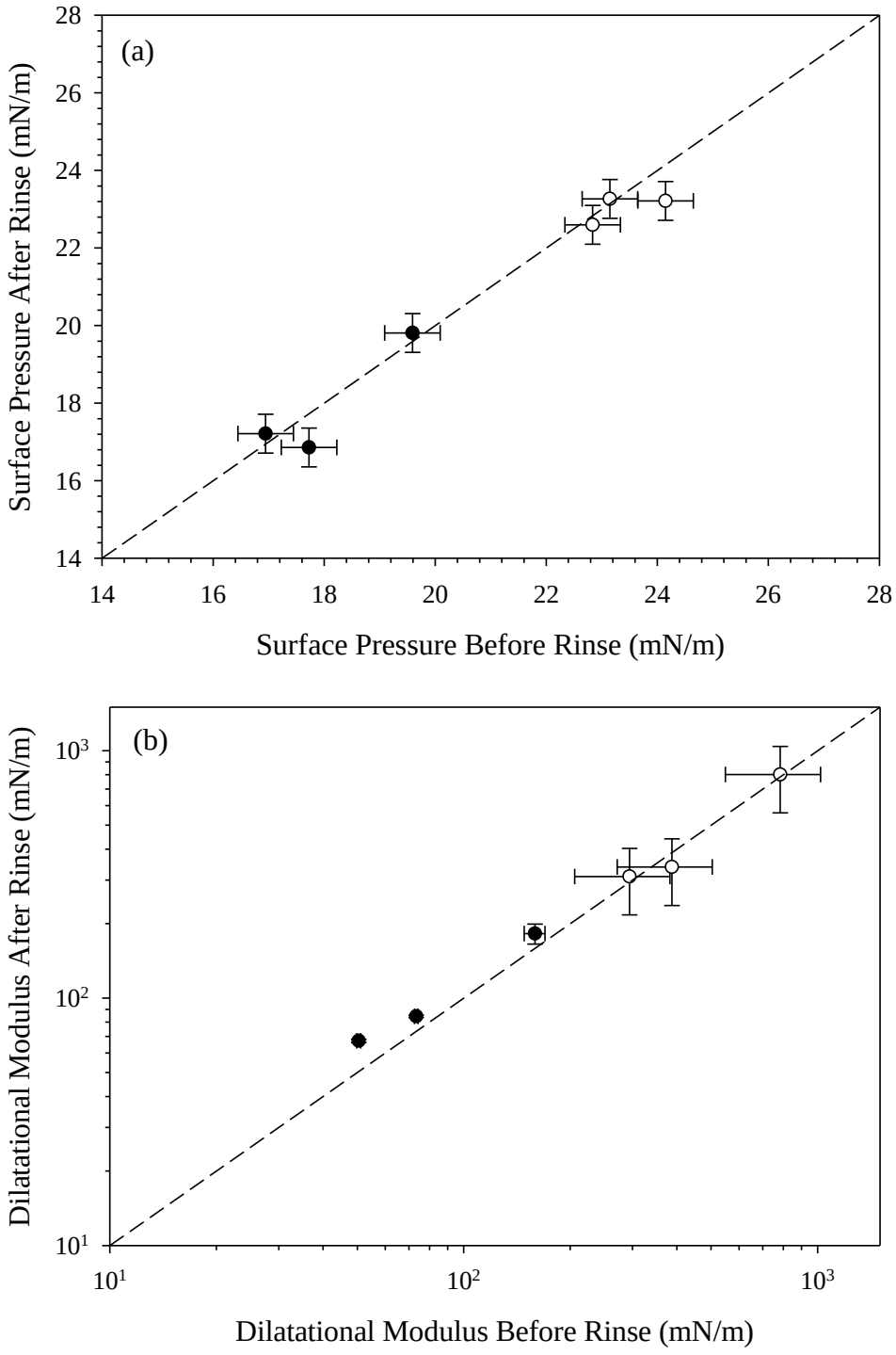

Figure A.3: (a) Surface pressure and (b) dilatational modulus before and after exchanging the CU solution with deionized water. Surfaces rinsed at low surface coverages (filled symbols) exhibit low dilatational moduli that remain constant after rinsing. Surfaces rinsed at high surface coverages (open symbols) exhibit dilatational moduli too large to measure, and the minimum possible moduli are plotted.

REFERENCES

(1) Green, A. J.; Littlejohn, K. A.; Hooley, P.; Cox, P. W. Formation and Stability of Food Foams and Aerated Emulsions: Hydrophobins as Novel Functional Ingredients. *Curr. Opin. Colloid Interface Sci.* **2013**, *18*, 292–301.

(2) Lumsdon, S. O.; Green, J.; Stieglitz, B. Adsorption of Hydrophobin Proteins at Hydrophobic and Hydrophilic Interfaces. *Colloids Surfaces B Biointerfaces* **2005**, *44*, 172–178.

(3) Wösten, H. A. B. Hydrophobins: Multipurpose Proteins. *Annu. Rev. Microbiol.* **2001**, *55*, 625–646.

(4) Linder, M. B. Hydrophobins: Proteins That Self Assemble at Interfaces. *Curr. Opin. Colloid Interface Sci.* **2009**, *14*, 356–363.

(5) Haas Jimoh Akanbi, M.; Post, E.; Meter-Arkema, A.; Rink, R.; Robillard, G. T.; Wang, X.; Wösten, H. A. B.; Scholtmeijer, K. Use of Hydrophobins in Formulation of Water Insoluble Drugs for Oral Administration. *Colloids Surfaces B Biointerfaces* **2010**, *75*, 526–531.

(6) Valo, H. K.; Laaksonen, P. H.; Peltonen, L. J.; Linder, M. B.; Hirvonen, J. T.; Laaksonen, T. J. Multifunctional Hydrophobin : Toward Functional Coatings for Drug Nanoparticles. *ACS Nano* **2010**, *4*, 1750–1758.

(7) Wösten, H. a. B.; Scholtmeijer, K. Applications of Hydrophobins: Current State and Perspectives. *Appl. Microbiol. Biotechnol.* **2015**, *99*, 1587–1597.

(8) Alvarez, N. J.; Walker, L. M.; Anna, S. L. A Criterion to Assess the Impact of Confined Volumes on Surfactant Transport to Liquid–fluid Interfaces. *Soft Matter* **2012**, *8*, 8917–8925.

(9) Kirby, S. M.; Zhang, X.; Russo, P. S.; Anna, S. L.; Walker, L. M. Formation of a Rigid Hydrophobin Film and Disruption by an Anionic Surfactant at an Air/Water Interface. *Langmuir* **2016**, *32*, 5542–5551.

(10) Radulova, G. M.; Danov, K. D.; Kralchevsky, P. a; Petkov, J. T.; Stoyanov, S. D. Shear Rheology of Hydrophobin Adsorption Layers at Oil/water Interfaces and Data Interpretation in Terms of a Viscoelastic Thixotropic Model. *Soft Matter* **2014**, *10*, 5777–5786.

(11) Petkov, J. T.; Gurkov, T. D.; Campbell, B. E.; Borwankar, R. P. Dilatational and Shear Elasticity of Gel-like Protein Layers on Air/Water Interface. *Langmuir* **2000**, *16*, 3703–3711.

(12) Lucassen-Reynders, E. H.; Fainerman, V. B.; Miller, R. Surface Dilational

Modulus or Gibbs' Elasticity of Protein Adsorption Layers. *J. Phys. Chem. B* **2004**, *108*, 9173–9176.

(13) Bos, M. A.; van Vliet, T. Interfacial Rheological Properties of Adsorbed Protein Layers and Surfactants: A Review. *Adv. Colloid Interface Sci.* **2001**, *91*, 437–471.